



NEGF Based Analytical Modeling of Advanced MOSFETs

Fabian Hosenfeld

ADVERTIMENT. L'accés als continguts d'aquesta tesi doctoral i la seva utilització ha de respectar els drets de la persona autora. Pot ser utilitzada per a consulta o estudi personal, així com en activitats o materials d'investigació i docència en els termes establerts a l'art. 32 del Text Refós de la Llei de Propietat Intel·lectual (RDL 1/1996). Per altres utilitzacions es requereix l'autorització prèvia i expressa de la persona autora. En qualsevol cas, en la utilització dels seus continguts caldrà indicar de forma clara el nom i cognoms de la persona autora i el títol de la tesi doctoral. No s'autoritza la seva reproducció o altres formes d'explotació efectuades amb finalitats de lucre ni la seva comunicació pública des d'un lloc aliè al servei TDX. Tampoc s'autoritza la presentació del seu contingut en una finestra o marc aliè a TDX (framing). Aquesta reserva de drets afecta tant als continguts de la tesi com als seus resums i índexs.

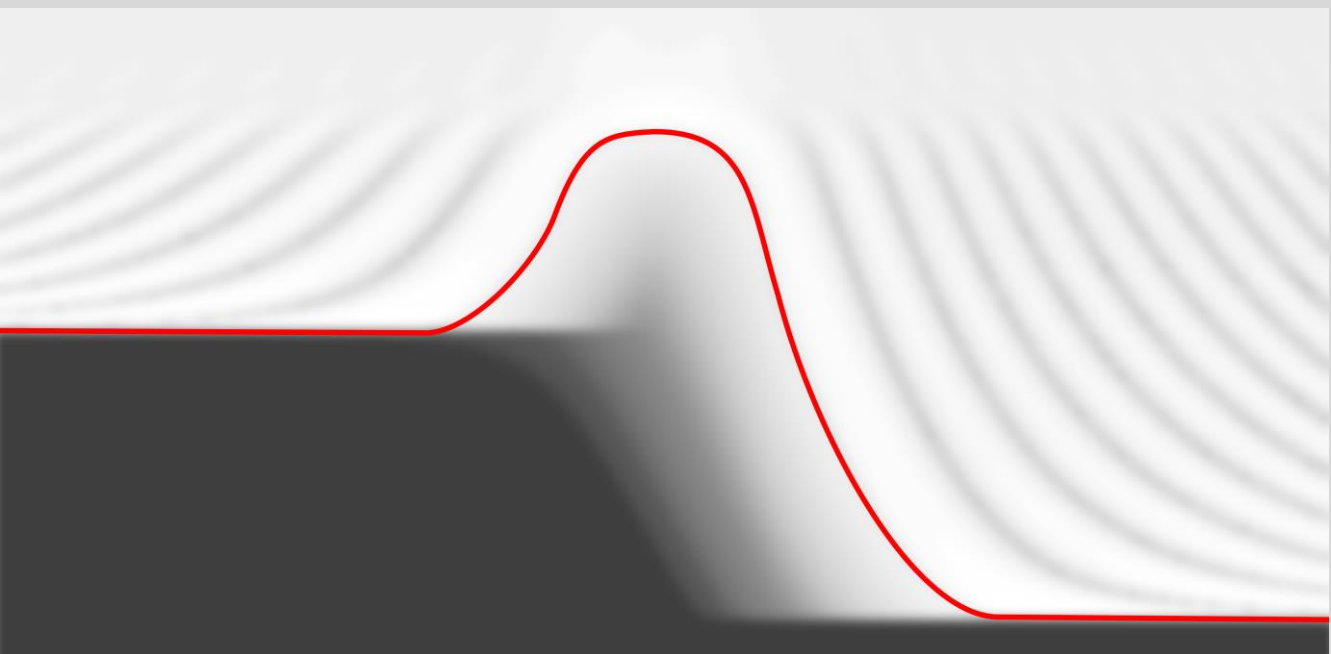
ADVERTENCIA. El acceso a los contenidos de esta tesis doctoral y su utilización debe respetar los derechos de la persona autora. Puede ser utilizada para consulta o estudio personal, así como en actividades o materiales de investigación y docencia en los términos establecidos en el art. 32 del Texto Refundido de la Ley de Propiedad Intelectual (RDL 1/1996). Para otros usos se requiere la autorización previa y expresa de la persona autora. En cualquier caso, en la utilización de sus contenidos se deberá indicar de forma clara el nombre y apellidos de la persona autora y el título de la tesis doctoral. No se autoriza su reproducción u otras formas de explotación efectuadas con fines lucrativos ni su comunicación pública desde un sitio ajeno al servicio TDR. Tampoco se autoriza la presentación de su contenido en una ventana o marco ajeno a TDR (framing). Esta reserva de derechos afecta tanto al contenido de la tesis como a sus resúmenes e índices.

WARNING. Access to the contents of this doctoral thesis and its use must respect the rights of the author. It can be used for reference or private study, as well as research and learning activities or materials in the terms established by the 32nd article of the Spanish Consolidated Copyright Act (RDL 1/1996). Express and previous authorization of the author is required for any other uses. In any case, when using its content, full name of the author and title of the thesis must be clearly indicated. Reproduction or other forms of for profit use or public communication from outside TDX service is not allowed. Presentation of its content in a window or frame external to TDX (framing) is not authorized either. These rights affect both the content of the thesis and its abstracts and indexes.



NEGF Based Analytical Modeling of Advanced MOSFETs

FABIAN HOSENFELD



DOCTORAL THESIS
2017

Fabian Hosenfeld

NEGF Based Analytical Modeling of Advanced MOSFETs

DOCTORAL THESIS

Supervised by Dr. François Lime
and Prof. Dr.-Ing. Alexander Kloes
and Prof. Benjamín Iñíguez

Department of Electronic,
Electrical and Automatic Control Engineering



UNIVERSITAT ROVIRA I VIRGILI

Tarragona
2017

Statement of Supervision



**Department of Electronic, Electric
and Automatic Engineering (DEEEA)**

Av. Paisos Catalans 26, Campus Sescelades
43007, Tarragona, Spain

Phone: +34 977 558524

Fax: +34 977 559605

I STATE that the present study, entitled: "NEGF BASED ANALYTICAL MODELING OF ADVANCED MOSFETS", presented by Fabian Hosenfeld for the award of the degree of the Doctor, has been carried out under my supervision at the DEPARTMENT of Electronic, Electrical and Automatic Control Engineering of this university, and that it fulfills all the requirements to be eligible for the European Doctorate Award.

Tarragona (Spain), August 30, 2017

Dr. François Lime, Doctoral Thesis Supervisor

Prof. Dr.-Ing. Alexander Kloes, Doctoral Thesis Supervisor

Prof. Benjamín Iñíguez, Doctoral Thesis Supervisor

Acknowledgments

The completion of my dissertation would not have been possible unless the help of many people. It is an honor for me to thank all those who have made this thesis become real. First of all, I want to thank my supervisors Dr. François Lime and Prof. Dr.-Ing. Alexander Kloes, who supported me throughout the entire thesis. Special thanks go to Prof. Dr. Benjamín Iníguez (University Rovira i Virgili, Tarragona, Spain) for the useful collaboration during the last three years. They have made available their support in a number of ways, they directing me to new topics of research and at the same time boosted me to achieve my own conceptions. We had plenty of useful conversations and they gave me advice on compact modeling and device simulations which made me smarter and helped me to complete this work.

I say thank you to my colleague Fabian Horst who helped me managing difficulties and strongly supported me on my studies as well as optimizing this work. Thanks to my former colleague Dr. Thomas Holtij for introducing me into the exciting sciences of compact modeling and working principles of transistors. Special thanks also to the members of the research group Dr. Michael Graef and Anita Farokhnejad for professional discussions over the past years.

Last but not least I wish to express my deepest thanks to my family Christel, Arnold, Daniel and my wife Julia Hosenfeld. You strongly supported me during my studies and all other chapters of my life!

... and many others...

Statement of Authorship



Research Group Nanoelectronics / Device Modeling

Wiesenstrasse 14

35390, Giessen, Germany

Phone: +49 641 309-1971

Fax: +49 641 309-2901

I STATE that this document has been composed by myself and describes my own work, unless otherwise acknowledged in the text. Parts that are direct quotes or paraphrases are identified as such. It has not been accepted in any previous application for a degree. All sources of information have been specifically acknowledged.

Giessen (Germany), November 1, 2017

A handwritten signature in black ink, appearing to read 'Fabian Hosenfeld', is written in a cursive style.

Fabian Hosenfeld, M. Sc.

List of Publications

Journals

- F. Hosenfeld, F. Horst, B. Iñíguez, F. Lime, A. Kloes, "A Quantum Wave Based Compact Modeling Approach for the Current in Ultra-Short DG MOSFETs Suitable for Rapid Multi-Scale Simulations", *Solid-State Electronics*, Vol. 137, pp 70-79, 2017
- F. Hosenfeld, F. Horst, M. Graef, A. Farokhnejad, A. Kloes, B. Iñíguez, F. Lime, "Rapid NEGF-Based Calculation of Ballistic Current in Ultra-Short DG MOSFETs for Circuit Simulation", *International Journal of Microelectronics and Computer Science*, Vol.7, No. 2, pp. 65-72, 2016

Conferences

- F. Hosenfeld, F. Horst, F. Lime, B. Iñíguez, A. Kloes, "Non-Iterative NEGF Based Model for Band-to-Band Tunneling Current in DG TFETs", MIXDES 2017, Bydgoszcz, Poland, 2017
- F. Hosenfeld, M. Graef, F. Horst, B. Iñíguez, F. Lime, A. Kloes, "Modeling Approach for Rapid NEGF-Based Simulation of Ballistic Current in Ultra-Short DG MOSFETs", MIXDES 2016, Lodz, Poland, 2016
- F. Hosenfeld, M. Graef, F. Horst, B. Iñíguez, F. Lime, A. Kloes, "Semi-Analytical Model for Leakage Current in Ultra-Short DG MOSFET Based on NEGF Formalism", MOS-AK 2016, Dresden, Germany, 2016
- F. Hosenfeld, M. Graef, F. Hain, B. Iñíguez, F. Lime, A. Kloes, "Dynamic Look-up Table for Increased Numerical Efficiency of Multi-Scale Simulation Approaches in Circuit Simulations", MOS-AK 2015, Graz, Austria, 2015

Co-Autorship

- F. Horst, A. Farokhnejad, M. Graef, F. Hosenfeld, G. V. Luong, C. Liu, Q. Zhao, F. Lime, B. Iñíguez, A. Kloes, "DC/AC Compact Modeling of TFETs for Circuit Simulation of Logic Cells Based on an Analytical Physics-Based Framework", accepted for Austrochip 2017, Linz, Austria, 2017.

-
- M. Graef, F. Hain, F. Hosenfeld, F. Horst, A. Farokhnejad, B. Iñíguez, A. Kloes, "Analytical Modeling of RDF Effects on the Threshold Voltage in Short-Channel Double-Gate MOSFETs", MIXDES 2017, Bydgoszcz, Poland, 2017
 - F. Horst, M. Graef, F. Hosenfeld, A. Farokhnejad, G. V. Luong, Q. Zhao, B. Iñíguez, A. Kloes, "Static Noise Margin Analysis of 8T TFET SRAM Cells Using a 2D Compact Model Adapted to Measurement Data of Fabricated TFET Devices", EuroSOI-ULIS 2017, Athens, Greece, 2017
 - F. Horst, M. Graef, F. Hosenfeld, A. Farokhnejad, F. Hain, G. V. Luong, Q. Zhao, B. Iñíguez, A. Kloes, "Implementation of a DC Compact Model for Double-Gate Tunnel-FET Based on 2D Calculations and Application in Circuit Simulation", ESSDERC/ESSCIRC 2016, Lausanne, Switzerland, 2016
 - M. Graef, F. Hain, F. Hosenfeld, F. Horst, A. Farokhnejad, B. Iñíguez, A. Kloes, "Comparative Numerical Analysis and Analytical RDF-Modeling of MOSFETs and DG Tunnel-FETs", MIXDES 2016, Lodz, Poland, 2016
 - M. Graef, F. Hain, F. Hosenfeld, F. Horst, A. Farokhnejad, B. Iñíguez, A. Kloes, "Numerical Analysis and Analytical Modeling of RDF in DG Tunnel-FETs", EuroSOI-ULIS 2016, Vienna, Austria, 2016
 - F. Hain, C. Lammers, F. Hosenfeld, H. Klauk, U. Zschieschang, B. Iñíguez, A. Kloes, "Charge-based Modelling of the Channel Current in Organic Field Effect Transistors Considering Injection Effects", Electrochemical Society Meeting 2015, Chicago, USA, 2015
 - F. Hain, C. Lammers, F. Horst, F. Hosenfeld, B. Iñíguez, A. Kloes, "Continuous Charge-Based Current Model for Organic TFT Derived from Gaussian DOS", ICOE 2015, Erlangen, Germany, 2015
 - M. Graef, F. Hain, F. Hosenfeld, B. Iñíguez, A. Kloes, "Advanced Analytical Modeling of Nanowire Tunnel-FETs", Nanoelectronic Days 2015, Jülich, Germany, 2015
 - M. Graef, F. Hain, F. Hosenfeld, B. Iñíguez, A. Kloes, "Analytical Approach to Consider Gaussian Junction Profiles in Compact Models of Tunnel-FETs", EuroSOI-ULIS 2015, Bologna, Italy, 2015

Contents

1	Introduction	1
1.1	History of Semiconductor Development	2
1.2	Transistor Technologies	2
1.3	Circuit Design and Device Modeling	3
1.3.1	Device Simulation	4
1.3.2	Circuit Simulation	4
1.3.3	Multi-Scale Simulation	5
1.3.4	Properties of Physics-Based Compact Models	7
1.4	Challenges and Outline of Thesis	7
2	Basics of Microphysics	11
2.1	Fundamentals of Quantum Mechanics	11
2.1.1	Wave-Particle Duality	11
2.1.2	Thermionic Emission and Absorption	12
2.1.3	Wave Characteristics of Electrons	12
2.1.4	Heisenberg Uncertainty Principle	13
2.1.5	Pauli Exclusion Principle	13
2.1.6	Rutherford-Bohr Model	13
2.1.7	Momentum and Wavenumber	13
2.1.8	Construction of Atoms	14
2.2	Semiconducting Solids	15
2.2.1	Energy Level to Band Structure	15
2.2.2	Density of States	16
2.2.3	Fermi Distribution	17
2.2.4	Carrier Densities	18
2.3	Quantum Based Charge Transport	19
2.3.1	Hamiltonian	20
2.3.2	Schrödinger Wave Equation	20
2.3.3	Potential Well	23

Contents	x
2.3.4 Transmission and Reflection	27
2.3.5 The one-Level Device	29
2.3.6 Potential Profile of the one-Level Device	33
2.3.7 Multi-Level Device	35
3 Physics and Simulation Approach of Advanced MOSFETs	37
3.1 Ultra-Scaled MOSFETs	38
3.1.1 Ballistic Charge Transport	38
3.1.2 Source-to-Drain Tunneling Current	40
3.1.3 MOSFET Multi-Scale Simulation Approach	41
3.2 Tunneling Field-Effect Transistor	42
3.2.1 Band-to-Band Tunneling Current	43
3.2.2 TFET Multi-Scale Simulation Approach	45
4 Mathematical and Physical Derivation	47
4.1 Potential Theory	47
4.1.1 Poisson's and Laplace's Equation	47
4.1.2 Complex Potential Theory	49
4.1.3 Conformal Mapping Technique	50
4.1.4 Potential Solution	52
4.2 Non-Equilibrium Green's Function	53
4.2.1 Finite Difference Approximation	53
4.2.2 Effective Mass Hamiltonian	56
4.2.3 Infinite Wall Boundary Conditions	57
4.2.4 Open Boundary Conditions	57
4.2.5 Dispersion Relation	60
4.2.6 Retarded Green's Function	62
4.2.7 Electron Density	62
4.2.8 Numerical Treatment of Scattering	65
5 Potential Model	67
5.1 Modeling Preliminaries	68
5.1.1 Model Simplifications	68
5.1.2 Conformal Mapping of the Device Structure	70
5.1.3 Inversion Charges	71
5.1.4 Quantum Confinement	73
5.2 Closed-Form Solution of the 2D Potential	74
5.2.1 Effective Built-in Potentials	74
5.2.2 Integration Limits	75
5.2.3 Boundary Conditions and Potential Solution Within the Channel	75

5.3	Gate Influence on the Source and Drain Regions	78
5.4	Band Structure	79
5.5	Potential Adaption for DG TFET	80
5.6	MOSFET Potential Model Verification	82
5.7	TFET Potential Model Verification	87
6	MOSFET Current Model	89
6.1	Slicing of the Conduction Band	89
6.2	Current Calculation by NEGF	90
6.2.1	Hamiltonian Matrix	90
6.2.2	Self-Energy Functions	91
6.2.3	Broadening Functions	92
6.2.4	Spectral Function	92
6.2.5	Fermi Function	94
6.2.6	Density Matrix	94
6.2.7	Current Operator	96
6.2.8	Energy Dependent Integration	96
6.3	Approximations for Increased Numerical Efficiency	97
6.3.1	Energy Dependent Approximation	97
6.3.2	Geometry Dependent Approximation	98
6.4	Analytical Treatment of Electron Backscattering	99
6.5	MOSFET Model Verification	101
6.5.1	Ballistic transport	101
6.5.2	Non-Ballistic transport	105
6.6	Investigations of Short-Channel Effects	107
6.6.1	Source-to-Drain Tunneling	107
6.6.2	Quantum Reflections	108
6.6.3	Leakage Current	109
6.6.4	Subthreshold Slope	110
7	TFET Current Model	111
7.1	Transition Between Electrostatics and NEGF	111
7.2	Current Calculation	113
7.3	TFET Model Verification	114
8	Conclusion	117
	References	121

List of Symbols

Symbol	Description	Unit
ρ	Density matrix	[-]
ε	Energy level	[eV]
ε_{in}	Dielectric permittivity of insulator	[F/cm]
ε_{si}	Dielectric permittivity of silicon	[F/cm]
ε_0	Permittivity of vacuum	[F/cm]
Φ_{sp}	Surface potential	[V]
$\gamma, \mathbf{\Gamma}$	Broadening	[-]
φ	Potential	[V]
ϕ	Potential solution for the boundary condition	[V]
ψ	Wavefunction	[-]
$\Delta\Phi_{bi,s/d}$	Built-in potential (source or drain)	[V]
$\Delta\Phi_{bi,eff,s/d}$	Effective built-in potential (source or drain)	[V]
χ	Electron affinity	[eV]
λ	Screening length	[m]
$\Sigma(\mathbf{E})$	Self-energy	[eV]
\hbar	Reduced Planck's constant	[eVs]
a	Grid size	[m]
$\mathbf{A}(\mathbf{E})$	Spectral function	[1/eV]
c	Speed of light	[m/s]
C_{in}	Insulator capacitance per unit area	[F/cm ²]
$d_{s/d}$	Bending distance (source or drain)	[m]
$\mathbf{D}(\mathbf{E})$	Density of states (DOS)	[1/eV]
D_{in}	Dielectric displacement density	[C/cm ²]
E	Energy	[eV]
k	Wavenumber	[1/m]
E_c	Conduction band energy	[eV]
E_F	Fermi energy	[eV]
E_g	Band-gap	[eV]

E_v	Valence band energy	[eV]
E_{vac}	Vacuum energy level	[eV]
F_1	Fermi function of the left contact	[-]
F_2	Fermi function of the right contact	[-]
$\mathbf{G}(\mathbf{E})$	Green's function (retarded)	[1/eV]
h	Planck's constant	[eVs]
H	Hamiltonian operator	[eV]
\mathbf{H}_L	Hamiltonian matrix (longitudinal)	[eV]
I	Current	[A]
J	Current density	[A/(eV m ²)]
k_B	Boltzmann constant	[eV/K]
m_0	Free electron mass	[kg]
$n(x)$	Electron density per unit area	[1/m ²]
$n(E)$	Electron density per unit energy	[1/eV]
N	Number of electrons	[-]
N_A	Acceptor doping concentration	[1/cm ³]
N_D	Donor doping concentration	[1/cm ³]
p	Momentum	[kg · m/s]
q	Magnitude of electronic charge	[C]
$Q'_{i,s}$	Inversion charge density per unit area	[As/cm ²]
t_{ch}	Channel thickness	[nm]
t_{dev}	Device thickness	[nm]
t_{in}	Insulator thickness	[nm]
T	Absolute temperature	[K]
\bar{u}	Integration limits	[m]
U	Potential	[eV]
v_t	Thermal velocity	[m/s]
V_{in}	Voltage drop across the insulator	[V]
V_{fb}	Flat-band voltage	[V]
w	Complex variable for w-plane	[-]

Acronyms

Symbol	Description
B2B	Band-to-band
BTE	Boltzmann Transport Equation
BVP	Boundary value problems
CMOS	Complementary metal-oxide-semiconductor
D	Drain
DG	Double-gate
DIBL	Drain-induced barrier lowering
EDA	Electronic design automation
FEM	Finite element method
FET	Field-effect transistor
GAA	Gate-all-around
HDL	Hardware description language
IC	Integrated circuit
IVP	Initial value problem
ITRS	International technology roadmap for semiconductors
LDOS	Local density of states
MOSFET	Metal-oxide-semiconductor field-effect transistor
NEGF	Non-equilibrium Green's function
PDE	Partial differential equation
QE	Quantization effect
RF	Radio frequency
RDF	Random dopant fluctuation
S	Source
SCE	Short-channel effect
SD	Source-to-drain
SOI	Silicon on insulator
TAT	Trap-assisted tunneling
TCAD	Technology computer aided design

TFET	Tunneling field-effect transistor
WKB	Wentzel-Kramers-Brillouin

CHAPTER 1

Introduction

New innovations in computer technologies have changed life over the past 40 years. Nowadays, it is common to use laptops, smartphones and micro-controllers many times a day. The entry of smart devices into daily life is contributed by a formidable progress in computer chip technology. Researchers all over the world improve the performance of these integrated circuits (IC) which are made out of billions of transistors. Due to the high performance, good scalability and low power-consumption, the metal-oxide-semiconductor field-effect (MOSFET) has become the most common used device. A reduction of its geometry, especially of its channel length from μm to the sub 20 nm region has led to better characteristics but also to unintended parasitic effects. To continue this shrinking process down to even smaller transistors, new and even more complex device geometries are necessary. In order to prevent future product failures, it is necessary to check these new devices beforehand. During the development process the products are simulated countless times. First, the focus is on the simulation of single transistors and then on circuits. These two types of simulations differ fundamentally. The simulators for single transistors make use of the finite element method (FEM) and consider technology parameters and physical effects to predict an accurate behavior. Nowadays, the geometries are so small, that even quantum effects influence the device behavior. Based on these studies, compact models can be realized which are much faster than FEM simulations and are therefore indispensable when simulating circuits. In the next step, the interaction of many transistors is simulated in circuit simulators like SPICE (Simulation Program with Integrated Circuit Emphasis) [1] to estimate the circuit behavior. Bridging the gap between compact transistor models and numerical quantum based device simulations is named in this context as multi-scale simulation, which is the major challenge of this thesis. Therefore, the analytical model fits for the next level of transistors and on the other hand is still fast enough to enable circuit simulations.

The following sections deal with the history of semiconductors and the proceeding development. In a further step, the differences between device modeling and circuit design are clarified. In the end of this introduction chapter the thesis' goals and outline are presented to the reader.

1.1 History of Semiconductor Development

Over the past 150 years our life has been electrified by several inventions. One of those was made in 1926 by Julius Edgar Lilienfeld when he presented his patent "Method and apparatus for controlling electric currents" [2], where he described a three terminal device, whereby two contacts were connected with a compound of copper and sulfur. The third contact establishes a potential between the others and influences the current. Today his innovation is well known as the field-effect transistor. In the same year, Erwin Schrödinger opened the door to quantum mechanics by formulating the well known Schrödinger equation [3]. He gave an expression to calculate the eigenvalues for a hydrogen atom by applying the time-independent wave equation. In 1933 he was honored for his work with the Nobel Prize. The discovery of the p-n junction by Russel Ohls in 1940 [4] led eight years later to the conception of the bipolar transistor by William Shockley [5, 6] who received the Nobel Prize in Physics in 1956. The first n-p-n structures with a thin layer were built in 1950 by the Bell Labs [7]. Jack Killby of Texas Instruments showed the first integrated Circuit (IC) in 1958 [8] and received the Nobel Prize in Physics for his invention in December 2000. In 1959, the Bell Labs engineers M. Atalla and D. Kahang presented the electric field controlled semiconductor device, which was the first insulated-gate field-effect transistor (FET) [9] that later became the most common device in integrated circuits. The combination of nMOS and pMOS transistors in electrical circuits was done by C. T. Sah and Frank Wanlass, who were with the Fairchild R&D laboratory in 1963 [10, 11]. This complementary MOS (CMOS) technology achieved a decrease of standby power and is still used today. Gordon Moore gave a statement in 1965, that due to the continuous decreasing gate length dimension, the number of components per chip will increase exponentially. In particular he said that the number of components would double every 12 month [12], about 10 year later he improved his statement to a double of the components every 2 years [13]. Nowadays, this prediction is still valid and well known as Moore's law. Ted Hoff and Staley Mazor developed Intels's 4004 in 1971, which was one of the first commercial available microprocessors. This microprocessor was build in a 16-pin package and included 2300 transistors [14].

All these achievements made by an uncountable number of scientists have led to the current MOSFET technologies and challenges introduced in the following section.

1.2 Transistor Technologies

The objectives to achieve better performance of computer technologies have been unchanged for many years. One challenge is to increase the number of devices on a single chip and hence the transistor density. Another focus is to increase the clock frequency of microprocessors [15]. Furthermore, it is necessary to reduce the power consumption of each transistor, otherwise self-heating problems may cause operational failures. A discrepancy can be seen in the transistors switching speed and its leakage current. The transistors can be adapted to achieve a very high

switching speed to the cost of a higher leakage power which is preferred in server computing. Lower leakage power is needed in mobile always-on circuits and are hence designed with a lower switching speed. In general, both properties can be improved by reducing the transistors channel length [16]. In 2016 Intel started the 6th generation Core processor "Skylake". It is manufactured using an 14 nm tri-gate CMOS technology. Compared to previous generations, the performance and its active power is improved [17].

In fact, transistors being developed with a short channel length do not have just advantages, consequently they suffer from undesired parasitic effects. These effects are called short-channel effects (SCEs) and occur due to the reduced gate influence onto the channel region of the MOSFET when shrinking down the device [18]. An important SCE is the threshold voltage roll-off caused by the charge sharing effect. This effect leads to a geometry dependent threshold voltage. Drain-induced barrier lowering (DIBL) is a reduction of the energy barrier within the channel due to the influence of the drain region. In other words, the threshold voltage becomes drain voltage dependent [19]. These effects lead to a higher off-state leakage current and a higher static power consumption.

Due to further miniaturization, several effects related to the atomic structure such as random dopands [20] and edge roughness [21] influence the device behavior. Additionally, quantum mechanical effects have an impact on device performance. In ultra-thin silicon layers, a quantization of the sub band energy occurs which also affects the threshold voltage [22]. An other quantum mechanical effect can be seen at channel length below 10 nm. For this channel length source-to-drain (SD) tunneling starts to decrease the device's on/off ratio [23][24].

Over the last few years, tunneling field-effect transistors (TFETs) have become increasingly important because they are viewed as a possible successor to the standard MOSFET. The device combines two advantages, the CMOS compatibility and due to the carrier transport caused by the band-to-band (b2b) tunneling effect, a subthreshold slope of less than 60 mV/dec at a temperature of 300 K can be achieved. The device is therefore a steep slope device and consequently suitable for low power applications [25].

1.3 Circuit Design and Device Modeling

Developing new integrated circuits with billions of transistors inside is a great challenge. The total process includes the design of individual devices, the virtual composition of many devices with its validation, the manufacturing and cost analysis. In a hard competition to provide an attractive price and the newest chip generation, it is necessary to reduce the time and costs of the development process. Today, lots of electronic design automation (EDA) tools for high-level digital design are used to model and simulate discrete devices. These devices are simulated countless times to consider the functionality in different operating conditions. The chip designer investigates the chip behavior for different ambient temperatures, changes in the power supply and the impact of radio frequencies (RF). Another important part of the chip simulation is addressed to the existence of statistical variations in device parameters like doping, thickness

and line-edge roughness. Every built transistor in a chip is unique and minimally differs from its expected behavior. The combination of many individual working transistors can lead to a failure of the total circuit [26]. For these reasons compact models are developed which are then used in circuit simulators to estimate the behavior of the circuitry under test. These compact models are derived from numerical device simulations by simplifying the physical equations. Furthermore, the numerical simulations give the compact modeling designers an insight into the physical behavior of the semiconducting devices. This connection strongly couples both different types of simulations.

1.3.1 Device Simulation

The manufacturing costs of a single nano-scale transistor is enormous and sometimes especially for future devices at this point in time impossible. To estimate the behavior of those novel devices, researchers are forced to simulate these devices using Technology Computer Aided Design (TCAD) device simulators like TCAD Sentaurus [26], Minimos-NT [27] or ATLAS [28][29]. These discrete device simulators allow the 2D or 3D virtual creation of semiconductor devices out of individual parameters. Device designers are able to predict the impact of different materials, doping, geometries and much more in this way. Additionally, TCAD tools enable a look inside the device, for example to investigate the electric field in its cross-section, which can not be measured. Therefore, TCAD simulations are necessary to gain the understanding of transistors and are consequently unalienable for developing compact models. The simulator divides the transistor model into many small pieces (mesh) and solves the physical equations for each mesh point. Since partial differential equations have to be solved, the received results have to be adjusted after each iteration until the simulation converges. This iterative process by using a mesh is well known as FEM simulations. Depending on the settings, accuracy and the total number of mesh points, the simulation of one device lasts from a few minutes to some days. Consequently, these numerical methods are good for accurate simulations of single devices but much too complex and time-consuming for circuit simulation.

1.3.2 Circuit Simulation

Circuit simulations do not aim on the simulation of a single transistor. The target of circuit simulations is on the combination of many devices to achieve a requested functionality. Some of the most important circuit simulators are SPICE [1] and ELDO [30]. Computer aided design of electrical circuits is based on accurate compact models of electrical devices. These models represent the device characteristics and behavior through a set of physics-based equations and model parameters. In contrast to device models, compact models have less degrees of freedom. They are less accurate and only valid for specific device parameter variations. The equations which describe the device behavior are analytically solved and work completely without iterative solutions. Following this, compact models are much faster than TCAD simulations. The speed of compact models depend on the complexity of the device describing equations. In general,

the compact models can be split into the following categories [18, 31, 32]:

- **Physics-based models** strongly refer to physical parameters and equations to describe the transistor's behavior. These models are good for describing scaled devices and fit for many parameter variations. Often, they are introduced for the description of long-channel devices. In other cases, they are used for the calculation of individual characteristics like subthreshold slope and threshold voltage.
- **Numerical-fit models** are based on mathematical expressions and work without physical relations. The device describing behavior is made through many fitting parameters which are adopted from numerical TCAD simulations. On the one hand, this approach is very fast and is not technology dependent, but on the other hand results outside the data range are not validated. Consequently, the model needs to be adapted for each parameter change.
- **Empirical-based models** are a composition of both, the numerical-fit models and physics-based ones. These models use many physical equations and add some numerical fitting parameters to reduce complexity. This method leads to less physical dependency but also to faster models.

No matter which kind of compact model is used, all models should be balanced between the following requirements [18, 33]:

- A high accuracy should be given over all operation regions to reproduce a good electrical device behavior.
- Simplicity to be fast.
- Especially for analog applications, the derivative of the current should be continuous, otherwise convergence problems will abort the circuit simulation.
- The model should be scalable for state-of-the-art design devices.

1.3.3 Multi-Scale Simulation

Multi-scale describes the interaction between variables in one scale on variables in another scale. In this context, it bridges the gap between compact models, its fast and efficient calculation of the device terminal voltages and numerical device models which consider quantum effects of nano-scaled devices. The device current of ultra-short MOSFETs consists of two parts, the thermionic emission current and the unwanted SD tunneling current [23]. The thermionic emission current is well known and can be described by classical physics. The SD tunneling current can be described by quantum mechanics and influences the device behavior of MOSFETs with ultra-short channel length. The proportion of SD tunneling current to the device current increases with decreasing channel lengths as soon as the channel length falls below 10 nm.

Overcoming this geometry milestone of 10 nm always results in a significant increase of the device's OFF-current, hence reducing the on/off ratio and a degradation of the subthreshold slope. Consequently, SD tunneling current physically limits the scaling of the channel length [23] [34] [35]. Modeling this and other quantum mechanical effects becomes more and more important and are some of the requirements of future simulations [36].

The non-equilibrium Green's function (NEGF) formalism, introduced by Martin, Schwinger, Kadanoff, Baym and Keldysh in the 1960's, is a general method for considering coherent and incoherent quantum transport [37]. The formalism provides a sound conceptual basis to establish atomic-level quantum mechanical simulations because it can handle great number of transport problems. During the last years the formalism has been applied to simulate resonant tunneling diodes (RTD), MOSFETs, carbon nanotubes as well as graphene based devices. Due to the atomistic consideration of charge transport, the NEGF formalism has become one of the most promising current calculation methods for numerical simulations of nano-scaled MOSFETs [38] [39] [40] [41] [29] [24]. Based on the NEGF formalism, the thermionic emission and SD tunneling current are inherently considered [23] [34] [35] [42]. In order to transfer these mathematics from numerical device simulations to numerically efficient compact transistor models for circuit simulation, the advantages of numerical models have to be merged with the advantages of compact models.

Physics-based compact models for DG MOSFETs as shown in Fig. 1.1(a) are commonly based on classical transport equations such as Boltzmann Transport Equation (BTE). These transport equations are only able to calculate the thermionic emission current, whereas the SD tunneling current is neglected. The NEGF is the matrix form counterpart of the Schrödinger equation. Numerical device simulations couple the NEGF with a Poisson solver to achieve a self-consistent solution. The iterative procedure (see Fig. 1.1(b)) increases the simulation time. By considering scattering effects, another iterative coupling for matching each scattering event with the density matrix as for instance the Büttiker probe model dramatically increases the simulation time.

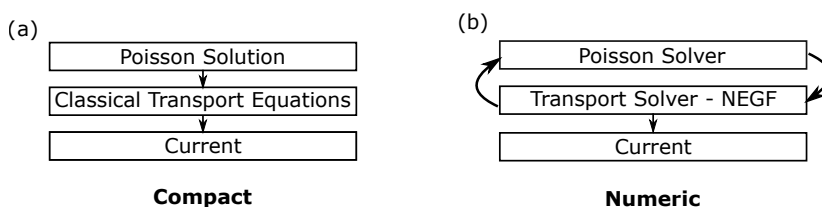


Figure 1.1: Flowchart of (a) compact models using analytical solved equations. (b) Common numerical NEGF simulations which iterate between transport and Poisson solver.

1.3.4 Properties of Physics-Based Compact Models

The different demands on the physical compact models like accuracy, speed or parameter variability for analog, digital and mixed signal simulations result into an abundance of different models. Compact models for describing MOSFETs can be separated into the following categories [43].

- **Threshold voltage based models** are one of the first compact models implemented in circuit simulators. These models simply calculate the surface potential in dependency on the input voltage. The surface potential is separated in two regions. In strong inversion $V_g \geq V_T$, the surface potential is assumed to be constant, however in weak inversion $V_g \leq V_T$ the surface potential is assumed to be linear. Applying a smoothing function, both separate parts were connected [43]. The disadvantage of this regional approach is the inaccuracy in the moderate inversion region [44]. This method is realized in BSIM1-4 [45], Berkley MOSFET model family 1-3 and MOS Model 9 [46].
- **Surface potential models** are based on the calculation of the surface potential at both ends of the channel for the applied biases. The resulting current and its derivatives are calculated for the existing charges, which depend on the surface potential of the channel. Most of these models use the substrate/bulk as the reference terminal to achieve a symmetric device operation. An accurate description of the device current and its derivatives without discontinuity are the advantages of these models [43]. Commonly used models which are based on this method are: MOS Model 11 [47], HiSIM [48] and PSP [49].
- **Charge based models** are based on the simplified but accurate modeling of the inversion charges within the channel. The relation between the charges and the channel potential is given by the current-voltage relationship. The device current expression is given in terms of inversion charge densities. In most models, the physical symmetry is achieved using the bulk as reference. The analytical linearization of the inversion charges leads to the small signal parameters [43]. This method is implemented in BSIM5 [50], EKV [51] and ACM [52].

1.4 Challenges and Outline of Thesis

This dissertation introduces a novel method for the current calculation in analytical models of field-effect transistors. From the modeling point of view there are certain objectives to fulfill in order to develop a multi-scale model. The approach should be implemented in an analytical, physics-based model for nano-scaled DG MOSFETs. The aim is to simplify the mathematics of the current calculation which is commonly used in numerical device simulations to a straightforward manner. The main scientific objectives are:

- A 1D NEGF formalism should be implemented into an analytical DG MOSFET model. Therefore, the NEGF based transport solver needs to be decoupled from the Poisson solver and the NEGF transport equation must be transferred into a closed-form.
- The closed-form potential solution, developed and published in previous work [53] should be adapted and extended to consider ultra-short channel lengths and channel thicknesses, which also includes the consideration of quantization effects [54].
- The computational efficiency of the developed model needs to be increased, in order to enable circuit simulations.
- The developed quantum based transport equation should be adapted to a TFET model to show the general validity of the formalism.
- To ensure sufficient accuracy, both developed models are to be verified with TCAD simulation data.

To fulfill the recent goals of the ITRS [15] requirements for future CMOS technology, the target of the MOSFET lays on ultra-short devices with a minimum channel length of 6 nm and thicknesses down to 2 nm. For these geometries, quantization effects (QEs) play a notable role. Because SD tunneling dramatically worsens the subthreshold slope and consequently the *on/off* ratio in ultra-short MOSFETs, these effects are addressed and discussed. The developed model consists of three main parts, the Poisson solution, the NEGF based transport equation and the efficient calculation of the device current. All these parts are discussed in the following chapters.

The physical preliminaries beginning with atom physics up to semiconducting solids are introduced in chapter 2. Additionally, Schrödinger's wave equation is derived and finally the charge transport of extremely scaled devices is explained in detail. At the end of the chapter, a semiclassical transistor model based on only one-level is given.

In chapter 3 the reader is introduced to the general operational principle of the MOSFET and of the TFET. Based on this, the modeling approach is derived in order to incorporate quantum based charge transport within an analytical model.

In chapter 4 the necessary mathematical basics for the potential model are shown. Therefore, the complex potential theory and the conformal mapping is introduced. Within the second part of the chapter, the NEGF formalism is derived. The formalism applies the Schrödinger equation in connection with appropriate boundary conditions. Also, the finite difference approximation is derived, which is one opportunity to solve computationally a partial differential equation.

In chapter 5 the potential model is introduced. It consists of a 2D analytical closed-form Poisson solution within the channel area, based on the conformal mapping technique by applying the Schwarz-Christoffel transformation [55]. First, the focus is on the subthreshold region of the device, hence mobile charges may be neglected in the solution of Poisson's equation. In order to extend the model by the on-state operations of the device, a closed-form model for

the calculation of the inversion charges is implemented. The potential solution leads to the electrostatics of the whole device, including the source and drain region. Using the potential solution, the band structure can be calculated for different geometry and material variations.

In chapter 6 the MOSFET current model is shown. In a first step the transition from the potential model to the NEGF based current calculation is detailed. The Green's function leads to the electron density and hence to the current for each energy. In the end, the device current can be calculated in a numerically efficient way by applying analytical functions. Finally, a performance comparison between various device geometries is shown and the impact of short-channel effects are highlighted.

The implementation of the NEGF formalism into an analytical TFET model is given in chapter 7. The energy bands are reshaped from a two-band structure into a one-band structure, which maps the b2b tunneling into a kind of SD tunneling. At the end of the chapter, the received results of the TFET model are compared with numerical TCAD data.

Finally, the overall conclusion is reflected in chapter 8 and an outlook on the future research prospects is presented.

CHAPTER 2

Basics of Microphysics

In order to explain the behavior of a transistor in the nano-scale, it is essential to understand the properties of semiconductors. Quantum mechanics describes the interaction of single atoms and the charge transport of mesoscopic devices. The following sections show some of the most important physical effects. Starting with the consideration of single electrons and atoms shown in Sec. 2.1, the scale becomes bigger up to semiconductors (see Sec. 2.2) and transistors (see Sec. 2.3).

2.1 Fundamentals of Quantum Mechanics

Quantum mechanics are necessary to understand the electrical behavior of solids. In the following, some of the major quantum effects are summarized from [56] [57]:

2.1.1 Wave-Particle Duality

The detection of interferences of light by many physical experiments have shown that light can be described by waves. On the other hand, it can be shown by the photo electric effect that light is also described by particle properties which are named as Photons. The photo electric effect causes the release of electrons in a solid due to illumination. More light causes no higher energy but more electrons, which can not be described by wave properties. Einstein explained this behavior with light particles and showed the relationship of energy E and the frequency of the light ν . The frequency can also be expressed by dividing the wavelength λ with the speed of light $c = 2.998 \cdot 10^8 \text{ m/s}$ [56]:

$$E = h\nu = h\frac{c}{\lambda} = 2\pi\hbar\frac{c}{\lambda}, \quad (2.1)$$

with $h = 6.626 \cdot 10^{-34} \text{ Js}$ is the Planck constant and $\hbar = h/(2\pi)$ is the reduced Planck constant. In semiconducting physics, it is common to describe the energy in the unit electron volt $1 \text{ eV} = 1.602 \cdot 10^{-19} \text{ J}$. By doing this, the Planck constant is also given by $h = 4.136 \cdot 10^{-15} \text{ eVs}$

and can be used to calculate the energy of a photon in dependency on its wavelength:

$$E = \frac{hc}{\lambda} = \frac{1240 \text{ eVnm}}{\lambda}. \quad (2.2)$$

Since photons are particles and can also have a velocity, they inevitably have a momentum. The momentum directly leads to the wave number k which is commonly used to characterize plane waves, having a wavelength λ . The relationship between the wavelength and the momentum is described by the Planck constant:

$$p = \hbar \frac{2\pi}{\lambda}, \quad k = \frac{2\pi}{\lambda}. \quad (2.3)$$

Substituting Eq. (2.3) in Eq. (2.1), the relation between energy and momentum is defined by:

$$E = cp. \quad (2.4)$$

2.1.2 Thermionic Emission and Absorption

The interaction of electrons with photons can cause an energy exchange. The absorption of a photon by an electron raises its energy. The opposite is given when an electron loses some energy by sending out a photon named as emission. Figure 2.1 shows the absorption and emission of photons by an electron, causing a change of the electrons energy. The absorption of a photon increases the energy of the electron by $\Delta E = h\nu$, whereas the emission of a photon lowers the electron's energy [56].

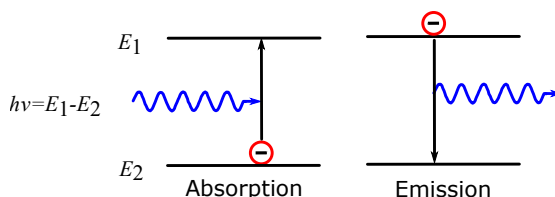


Figure 2.1: Absorption and emission of photons by an electron [56].

2.1.3 Wave Characteristics of Electrons

According to light, electrons are also liable to the wave-particle duality. The same can be applied for the relationship between its momentum and wavelength named in this context as the de Broglie wavelength. The wave characteristics can only be seen in mesoscopic physics due to a smaller mass and and also low momentum [56]:

$$\lambda = \frac{h}{p} = \frac{2\pi\hbar}{p}. \quad (2.5)$$

2.1.4 Heisenberg Uncertainty Principle

The uncertainty principle of Heisenberg implies that it is not possible to determine the location and the momentum of a microscopic particle at the same time. The location Δx and the momentum Δp is uncertain. This effect does not play part in traditional devices but in ultra-short channel devices. Falling below a channel length of 10 nm the momentum of the electrons can not exactly be estimated [56]:

$$\Delta x \Delta p = \hbar. \quad (2.6)$$

2.1.5 Pauli Exclusion Principle

The Pauli exclusion principle regulates the occupation of states by electrons. According to the principle, every quantum mechanical state can only be occupied by 2 electrons. Considering the up- and down-spin of electrons, every quantum mechanical state can be occupied by one electron [56].

2.1.6 Rutherford-Bohr Model

Any existing substances are made of atoms. Atoms consists of negative charged electrons in the atomic shell and a positive charged atomic nucleus made out of neutrons and protons. The electrons circulate around the atomic nucleus with a distance r and a momentum $p = mv$. The acting Coulomb force relates to the mass of a free electron m_0 and the permittivity of vacuum ϵ_0 [56]:

$$\frac{p^2}{m_0 r} = \frac{e^2}{4\pi\epsilon_0 r^2}. \quad (2.7)$$

The resulting energy is the sum of the potential energy and the kinetic energy:

$$E = E_{pot} + E_{kin} = \frac{e^2}{4\pi\epsilon_0 r} + \frac{p^2}{2m_0}. \quad (2.8)$$

Inserting the momentum from Eq. (2.7) in Eq. (2.8) leads to the total energy E as a function of r :

$$E = -\frac{e^2}{8\pi\epsilon_0 r}. \quad (2.9)$$

Experimental results show that only discrete orbital radii exist, because only those circles are stable which form coherent waves. Therefore, the wavelength is restricted to be a discrete multiple of the circle length. Electrons moving on the same radius do not lose energy, whereas electrons which change their radius, lose or gain energy by emission or absorption of photons.

2.1.7 Momentum and Wavenumber

Assuming a free electron located in the vacuum and is therefore not bound to an atom having a mass of m_0 and a velocity v , the corresponding energy of the electron is given according to

the squared momentum:

$$p = m_0 v, \quad (2.10)$$

$$E = \frac{m_0}{2} v^2 = \frac{p^2}{2m_0}. \quad (2.11)$$

The momentum of the electron can be split into a component for each direction in space $p^2 = p_x^2 + p_y^2 + p_z^2$. For simplicity, Fig. 2.2 shows the corresponding energy in dependency of only two momentum vectors. Due to the wave-particle duality, it is also possible to express

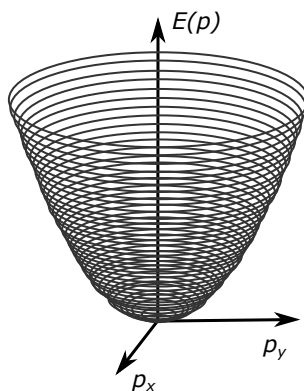


Figure 2.2: Dependency of the energy on the momentum shown for two dimensions [56].

the momentum by its wave number $p = \hbar k$ with $|k| = \frac{2\pi}{\lambda}$. The corresponding energy can also be expressed by the wave number k :

$$E = \frac{\hbar^2 k^2}{2m_0}. \quad (2.12)$$

2.1.8 Construction of Atoms

The periodic system of elements shows the elements in a structured way and starts with the atom with the least number of electrons. The electrons keep the total energy as low as possible and start to occupy the lowest shells at first. According to the Pauli principle, each quantum mechanical state can keep two electrons.

The s-shell is equal to one state and can be occupied by two electrons. The p-shell contains three states, each in a different direction in space and can be occupied by $2 \cdot 3 = 6$ electrons [56].

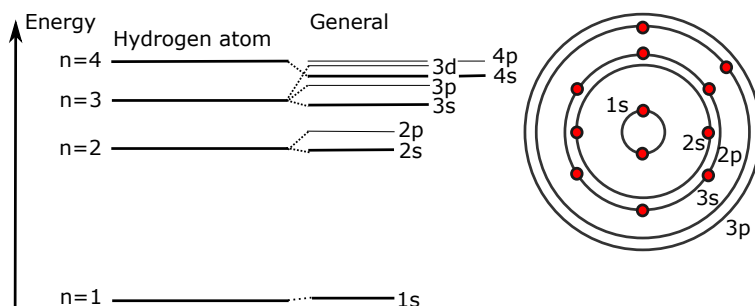


Figure 2.3: Schematic illustration of an atom and its surrounding electrons located on their shells [56].

2.2 Semiconducting Solids

Till now the focus was on single electrons and single atoms. In this section the scale is becoming bigger and focuses first on the combination of a few atoms (see Sec. 2.2.1) up to semiconducting solids which are composed of many atoms. The states of a solid are represented by a density of states (see Sec. 2.2.2). The occupation probability of these states is given by the Fermi function (see Sec. 2.2.3). The density of states together with the Fermi function leads to the carrier density within a semiconductor (see Sec. 2.2.4).

2.2.1 Energy Level to Band Structure

The connection of many atoms leads from discrete energy levels to energy bands. Fig. 2.4 shows the reduction of the distance between isolated atoms. The energy levels having higher energies penetrate into the energy levels of their neighboring atoms.

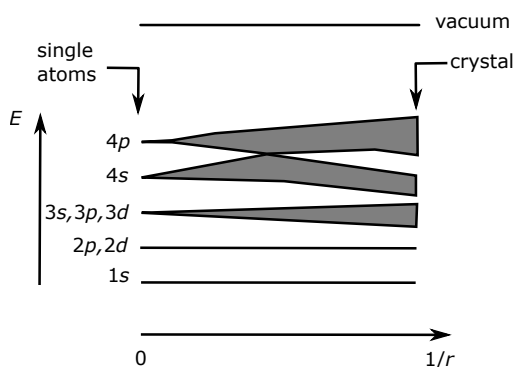


Figure 2.4: Distance reduction of separated atoms causes a broadening of the shells [56].

Fig. 2.5 shows 5 atomic nuclei together with their states. The states having less energy are

isolated whereas states having higher energies penetrate into each other. Therefore, the former discrete and isolated energy levels broaden to continuous energy bands. Equally to isolated

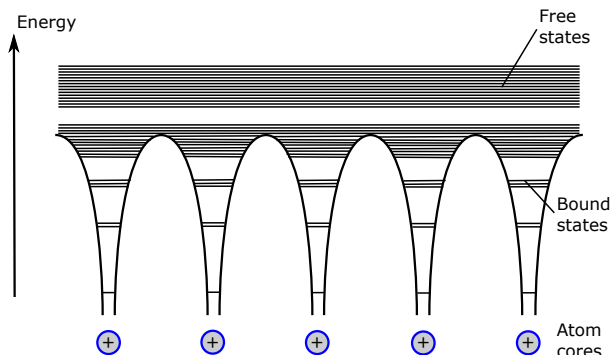


Figure 2.5: Schematic broadening of the energy level of an isolated atom to energy bands of a crystal [56].

atoms, the possibility that a state is occupied by an electron rises by lowering the energy and vice versa. The electrons in the lower energy bands are bound to the atoms, hence these energy bands are named valence bands. Because almost all states of the valence bands are occupied by electrons, electrons are not able to move through the solid. By adding energy to an electron, located at a lower energy band, it can occupy a free state of an energy band with a higher energy. The electron is not bound to the atom any more and is able to move freely inside the crystal. Electrons in those energy bands contribute to a conducting solid, hence these energy bands are named conduction bands [56].

2.2.2 Density of States

Aiming for the calculation of the number of electrons per energy, it is necessary to calculate the density of states per energy in a previous step. The density of states just tells how many states at a specific energy are available. According to the Pauli principle, there can only be two electrons within one state. The states within a crystal are separated by the wavevector k which is related to the momentum $p = \hbar k$ of the electron as shown in section 2.1.7. Each of the three different wavevectors can contribute to the same energy, because the total kinetic energy depends on the squared addition of them [56]:

$$E = \frac{\hbar^2 k^2}{2m_c} = \frac{\hbar^2 (k_x^2 + k_y^2 + k_z^2)}{2m_c}, \quad (2.13)$$

with m_c is the effective mass of the conduction band. Therefore, it is necessary to count the states which contribute to one specific energy. Fig. 2.6 shows the k -space for a plane area defined by k_x and k_y . The black dots represent the possible k -states. Assuming that $g(k)$ symbolizes the density of the states within an area, then the annulus having a thickness of dk

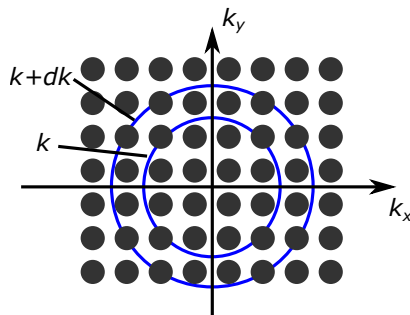


Figure 2.6: States within the k -space [56].

and an area of $2\pi k dk$ contains $g(k)2\pi k dk$ of k -states. According to the 2D example in 3D-space the geometry is a sphere and the k -states inside are calculated by $g(k)4\pi k^2 dk$. Transferring these results from the k -space to the energy space, the number of states per energy width are calculated by [56]:

$$g_c(E) dE = g(k)4\pi k^2 dk, \quad g_c(k) = \frac{2}{(2\pi)^3}. \quad (2.14)$$

Eq. (2.13) can be solved for k :

$$k = \sqrt{\frac{2m_c E}{\hbar^2}}. \quad (2.15)$$

Performing a derivation of Eq. (2.13) shows the $dE - dk$ -relationship:

$$dE = \frac{\hbar^2}{2m_c} 2k dk. \quad (2.16)$$

Substituting Eq. (2.15) and Eq. (2.16) in Eq. (2.13), the density of states per energy is calculated by:

$$g_c(E)dE = v_e \frac{2}{(2\pi)^3} 2\pi \left(\frac{2m_c}{\hbar^2}\right)^{\frac{3}{2}} \sqrt{E} dE, \quad (2.17)$$

with v_e being the number of conduction band minima.

2.2.3 Fermi Distribution

In a further step, it is necessary to determine whether a state is occupied or not. The probability that a state is occupied by an electron is described by the Fermi function and depends on the energy difference between the Fermi level E_F and the energy E of the state. The Fermi function calculates the occupation probability as follows [56]:

$$F(E) = \frac{1}{1 + e^{\frac{(E-E_F)}{k_B T}}} \quad (2.18)$$

If the energy of a state E equals the Fermi energy E_F the probability that the state is occupied is 50%. The probability at other energy states differs from 0 to 1 in general within an energy range of $k_B T$, where k_B indicates the Boltzmann-constant and T the temperature of the solid. In undoped semiconductors at room temperature, the Fermi energy has an intrinsic state E_{Fi} and is located between the valence and conduction band. Hence, the occupation probability of energy states by electrons is small for the conduction band and high for the valence band. Doping of the semiconductor with acceptors or donors causes a shift of the Fermi energy. This shift influences the occupation probability of the conduction and valence band. A higher probability within the conduction band leads to more free electrons and vice versa.

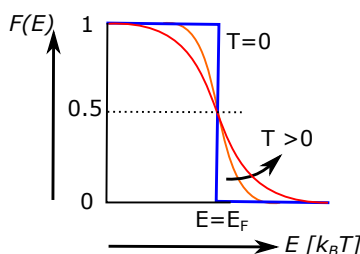


Figure 2.7: Fermi function with its sharp transition from 1 to 0 at a temperature $T = 0$ K. For higher temperatures the transition becomes smoother [56].

2.2.4 Carrier Densities

The electron density per energy is calculated by the multiplication of the density of states $g_c(E)$ and the probability of occupation $F(E)$ for all energies (see Fig. 2.8) [56]: The density of states is proportional to a square root function, whereas the Fermi function $F(E)$ is an exponential function. The resulting curve depicts the number of electrons. At small energies, the number of electrons is small, due to a small number of states at low energies. With increasing number of states, the number of electrons also increases. At higher energies, the decreasing probability of the Fermi function causes a decreasing electron density. The conductivity of a material depends on the total number of free electrons in the conduction band and the holes in the valence band. The total number of electrons is calculated by an integration over all energies:

$$n = \int_0^{\infty} g_c(E) F(E) dE. \quad (2.19)$$

Due to the complexity of both functions, an integration can not be done easily. Using some mathematical expressions, the resulting behavior can be approximated by the Fermi integral of the order $1/2$:

$$\mathcal{F}_{\frac{1}{2}}(\eta_c) = \frac{2}{\sqrt{\pi}} \int_0^{\infty} \eta^{\frac{1}{2}} \frac{1}{1 + e^{\eta - \eta_c}} d\eta, \quad (2.20)$$

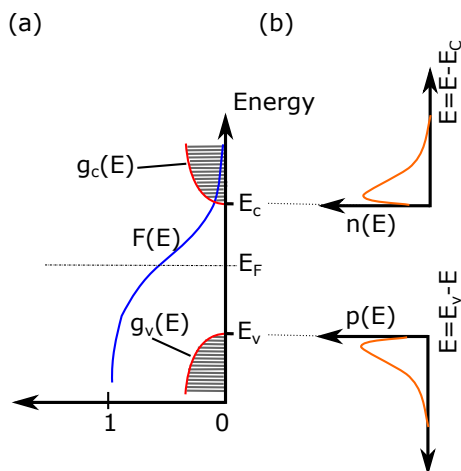


Figure 2.8: (a) Interaction of the Fermi function and the given energy states in a semiconductor. (b) Resulting electron and hole density per energy within the semiconductor [56].

$$\eta_c = \frac{E_F - E_c}{k_B T}, \quad \eta = \frac{E}{k_B T}. \quad (2.21)$$

By introducing the effective density of states of the conduction band N_c and the effective density of states of the valence band N_v :

$$N_c = 2v_e \left(\frac{m_c k_B T}{2\pi\hbar^2} \right)^{\frac{3}{2}}, \quad N_v = 2 \left(\frac{m_h k_B T}{2\pi\hbar^2} \right)^{\frac{3}{2}}, \quad (2.22)$$

the Fermi integral together with the effective density of states lead to a simplified equation of the total number of electrons:

$$n = N_c \mathcal{F}_{\frac{1}{2}}(\eta_c). \quad (2.23)$$

2.3 Quantum Based Charge Transport

This section is heading towards the particle transport within a simple device. Therefore, the quantum mechanics describing Hamiltonian operator (see Sec. 2.3.1) needed for the calculation of the Schrödinger wave equation (see Sec. 2.3.2) is introduced at first. In a further step, the infinite boundary conditions of a potential well (see Sec. 2.3.3) are turned into more realistic ones which allows the electrons to penetrate into the forbidden area. The movement of electrons through a barrier is introduced in Sec. 2.3.4, which serves as a fundamental description of the SD tunneling. A first device containing one single energy level is depicted in Sec. 2.3.5. The energy of its single energy level can be varied by the contacting voltages (see Sec. 2.3.6). Finally, the single energy level is replaced by many independent energy levels (see Sec. 2.3.7).

2.3.1 Hamiltonian

The Hamiltonian function \mathcal{H} is well known for describing a classical mechanic system by its kinetic energy proportional to its momentum p and potential energy $U(r)$ [57]:

$$\mathcal{H} = \frac{p^2}{2m} + U(r). \quad (2.24)$$

When defining a quantum mechanical system, the Hamiltonian operator has to be used, whereby a quantum mechanical system is defined to a size, which is comparable to the de Broglie wavelength of the particle. Therefore, the Hamiltonian function \mathcal{H} is turned into the Hamiltonian operator $\hat{\mathcal{H}}$ by replacing the momentum p with the momentum operator $\hat{p} = i\hbar \partial/\partial r$ [57]:

$$\hat{\mathcal{H}} = -\frac{\hbar^2 \nabla^2}{2m} + U(r). \quad (2.25)$$

The kinetic energy of a particle in space is given by the first part of Eq. (2.25), whereby the Laplace operator is written as:

$$\nabla^2 = \frac{\partial^2}{\partial x^2} + \frac{\partial^2}{\partial y^2} + \frac{\partial^2}{\partial z^2}. \quad (2.26)$$

2.3.2 Schrödinger Wave Equation

The Schrödinger wave equation, named after the Austrian scientist Erwin Schrödinger, describes the basics and physical concepts of electron movement in quantum mechanical systems by introducing wavefunctions. More precisely, the quantum mechanics $\hat{\mathcal{H}}$ are matched up with the wavefunction of the particle. The Schrödinger equation can be separated into two parts, the time-dependent and the time-independent one. Whereby the time-dependend Schrödinger equation is written as [57]:

$$i\hbar \frac{\partial \psi}{\partial t} - \hat{\mathcal{H}}\psi = 0. \quad (2.27)$$

Most problems in quantum mechanics are attributed to solve the Schrödinger wave equation of Eq. (2.27). It should be kept in mind that when considering a time-independent system $t \rightarrow \infty$ the uncertainty principle $\Delta E \cdot \Delta t \geq h$ is still valid and causes an inaccuracy of the measurement. For describing time-independent systems $U(r)$, which means that the device describing potential does not vary with time, the system's wavefunction can be separated into time and space coordinates:

$$\psi(r,t) = e^{-iEt/\hbar} \psi(r). \quad (2.28)$$

The time-independent part of the complex wavefunction is defined by $\psi(r)$ and depends only on the space coordinates. The time-independent complex function is also named as the stationary wavefunction. Inserting Eq. (2.28) into Eq. (2.27) results in the time-independent Schrödinger

equation:

$$\left(-\frac{\hbar^2 \nabla^2}{2m} + U(r)\right) \psi(r) = E\psi(r), \quad (2.29)$$

whereby E is the particle's total energy. In order to calculate the allowed energies, it is necessary to make a step back to the particles in free space $U(r) = 0$, which are described by plane waves $\psi(r,t) = Ae^{i(kr - \Omega t)}$, with Ω is the angular frequency and A is the amplitude. Inserting the description of plane waves into the Schrödinger equation (see Eq. (2.27)) leads to the dependency between the electron wave vector and its energy:

$$E = \hbar\Omega = \frac{\hbar^2}{2m} (k_x^2 + k_y^2 + k_z^2) = \frac{p^2}{m}, \quad (2.30)$$

and equals the classical momentum p and energy E relationship. The time-independent Schrödinger equation (see Eq. (2.29)) is attributed to an eigenvalue equation with E as the eigenvalue and $\psi(r)$ is the associated eigenfunction. The eigenvalues depend on the shape of the potential function $U(r)$ and also on the boundary conditions. In a further step, the three-dimensional time-independent Schrödinger equation is reduced to the one-dimensional case. Therefore, the system is confined by the one-dimensional potential energy $U(r) = U(x)$ (see Fig. 2.9).

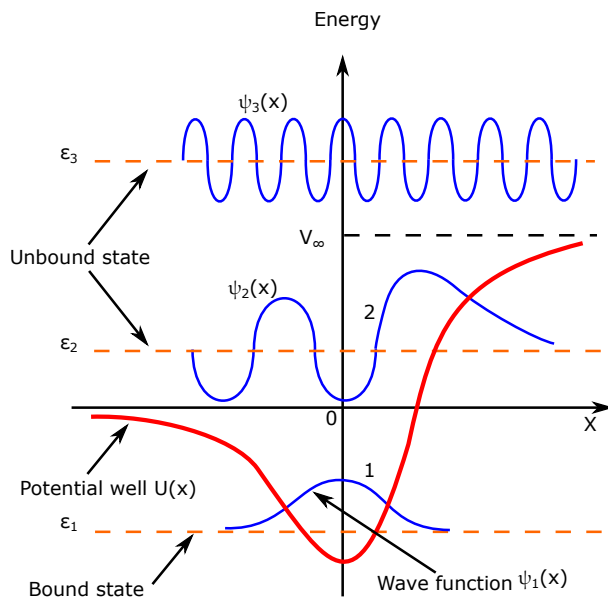


Figure 2.9: One-dimensional arbitrary formed potential well $U(x)$ and three different solution types of the Schrödinger equation $\psi_1(x)$, $\psi_2(x)$, $\psi_3(x)$ for different energies ε_1 , ε_2 , ε_3 [57].

In this case, x is the one-dimensional spatial coordinate and E is the energy. The potential well tends to 0 for $x \rightarrow -\infty$, has a negative minimum at $x = 0$ and tends to a certain value at

$x \rightarrow \infty$. The resulting solution strongly depends on the applied boundary condition. One of the possible solutions is given for a negative energy $E = \varepsilon_1 < 0$ labeled as curve 1 in Fig 2.9. The wavefunction decays in those regions, where the energy E is smaller than the confining potential barrier $U(x)$, which is named as the classically forbidden region. This decreasing wavefunction ψ within the forbidden region is shown for curve 1 for $x \rightarrow \infty$, $x \rightarrow -\infty$ and for curve 2 at positions for $x \rightarrow \infty$. Another possible solution of the wavefunction is shown by curve 2 at energy ε_2 . This wavefunction is confined only at the right hand side by the potential $U(x)$ and free on the other side. The next solution is to be found for particles which are free to move in both directions, as shown for curve 3 at energy ε_3 . The solution can be a superposition of waves propagating from the left side to the right side and vice versa.

As mentioned before, the Schrödinger equation is related to a linear equation. Its solution function ψ and consequently any multiples of the function ψ are solutions of the equation. To avoid this property, a look into the theory of probability is necessary. If a particle is located within a finite volume, the probability of finding this particle inside this volume must be equal to 1. This normalization condition results in the constant multiplication factor of the desired wavefunction within a finite sized system [57]:

$$\int |\psi(x,t)|^2 dx = 1. \quad (2.31)$$

Introducing scattering events complicates this assumption, because electrons in motion coming from the left side can be backscattered by the local potential as shown in Fig. 2.9 for the energies ε_2 , ε_3 . The general form of the wavefunction is described by [57]:

$$\psi(x,t) = Ae^{ikx}e^{-iEt/\hbar}, \quad (2.32)$$

with A is the amplitude and k is the wavenumber. Due to the linearity of the Schrödinger equation, the amount of scattered waves is proportional to the amplitude A . This initial condition deals with the state of a wave before and after the scattering event. In quantum mechanics and also in classical physics it is necessary to calculate the density of particle flow which means to calculate the number of particles crossing a unit area within a finite area and time. When considering waves, the particle flow is to be found by the derivation of the wavefunction [57]:

$$i_p = -\frac{i\hbar}{2m} (\psi^* \nabla \psi - \psi \nabla \psi^*), \quad (2.33)$$

with ψ^* is the complex conjugate of the wavefunction. In general, the Schrödinger equation defines the behavior of the wavefunction within a quantum mechanical system of particles. By combining the general solution with the initial or/and boundary conditions, the specific solution of the system is obtained. From the specific solution, the macroscopic parameters and the device operation can be derived. A further significance can be seen by the calculation of the average coordinates of a particle. The square of the wavefunction tells the probability of finding the particle at this position. If x being the position, the probability of finding the

particle at this position x' is obtained by [57]:

$$x' = \int \psi^* x \psi dx = \int x |\psi|^2 dx. \quad (2.34)$$

2.3.3 Potential Well

A straightforward theoretical experiment to show the behavior of waves is the one-dimensional quantum well. Today's devices are still three-dimensional and consequently the Schrödinger equation based on the three-dimensional coordinate vector r needs to be solved. But some physical effects can also be treated in a one or two-dimensional system. If the confining potential just depends on one coordinate, the wave vector $k_{||} = k_y + k_z$ can be reduced and the accompanied wavefunction is given with [57]:

$$\psi(t, r) = e^{i(k_y y + k_z z - \Omega t)} \psi(x). \quad (2.35)$$

Consequently, the wavefunction's amplitude depends on the x -coordinate and propagates in the y, z -plane. The one-dimensional Schrödinger equation is obtained by substituting Eq. (2.35) into Eq. (2.27):

$$\left(\frac{\hbar^2}{2m} \frac{d^2}{dx^2} + U(x) - \varepsilon \right) \psi(x) = 0, \quad (2.36)$$

with

$$\varepsilon = E - \frac{\hbar^2 k_{||}^2}{2m} \quad (2.37)$$

and E is the total energy, $(\hbar^2 k_{||}^2)/2m$ the kinetic energy in free y, z -direction and ε is the kinetic energy confined by the potential $U(x)$. In a further step, a particle is placed in this one-

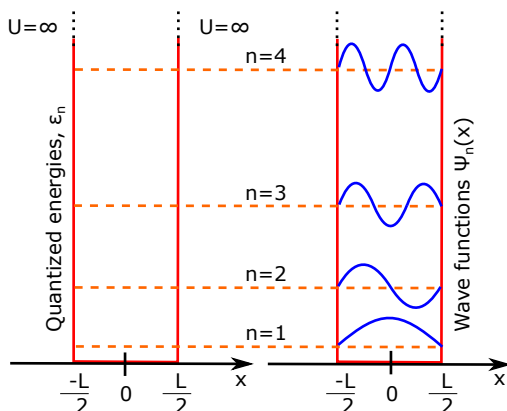


Figure 2.10: One-dimensional quantum well with applied infinite boundary conditions. Solving the Schrödinger equations leads to the wavefunctions and the quantized eigenenergies $\varepsilon_n = n^2 \varepsilon_1$ where $\varepsilon_1 = \hbar^2 \pi^2 / (2mL^2)$ [57].

dimensional system and confined by infinite potential walls on both sides at position $x = \pm L/2$ which can not be penetrated. Within the potential well the potential equals zero $U(x) = 0$ and in all other regions the potential is assumed to be infinite $U(x) = \infty$:

$$U(x) = \begin{cases} 0 & \text{for } |x| < \frac{L}{2}, \\ +\infty & \text{for } |x| > \frac{L}{2}. \end{cases} \quad (2.38)$$

The wavefunction within the well is described by the one-dimensional time-independent Schrödinger equation (see Eq. (2.36)), whereby the general solution of a plane wave is described by:

$$\psi(x) = Ae^{iKx} + Be^{-iKx}, \quad (2.39)$$

with:

$$K = \sqrt{\frac{2m\varepsilon}{\hbar^2}}. \quad (2.40)$$

Since the confining potential can not be penetrated, the boundary condition and hence the probability of finding the particle outside the well is zero:

$$\psi\left(-\frac{L}{2}\right) = \psi\left(+\frac{L}{2}\right) = 0. \quad (2.41)$$

The boundary conditions for describing a particle within a quantum well are to be found by applying the general solution of a plane wavefunction:

$$Ae^{-iK\frac{L}{2}} + Be^{+iK\frac{L}{2}} = 0 \quad \text{for } z = -\frac{L}{2}, \quad (2.42)$$

$$Ae^{+iK\frac{L}{2}} + Be^{-iK\frac{L}{2}} = 0 \quad \text{for } z = +\frac{L}{2}. \quad (2.43)$$

If the determinate of the algebraic system of equations equals zero, a nontrivial solution exists:

$$\begin{vmatrix} e^{-iK\frac{L}{2}} & e^{+iK\frac{L}{2}} \\ e^{+iK\frac{L}{2}} & e^{-iK\frac{L}{2}} \end{vmatrix} = 0, \quad (2.44)$$

which is given when:

$$\sin(KL) = 0 \quad \text{or} \quad KL = \pi n. \quad (2.45)$$

Consequently, the eigenvalues are calculated by:

$$K_n = \frac{\pi}{L}n, \quad n = \pm 1, \pm 2, \pm 3, \dots \quad (2.46)$$

Connecting Eq. (2.40) together with Eq. (2.46) leads to the possible eigenenergies of the particle:

$$\varepsilon_n = \frac{\hbar^2 k_n^2}{2m} = \frac{\hbar^2 \pi^2}{2mL^2} n^2. \quad (2.47)$$

The possible wavefunctions according to the eigenenergies are obtained by substituting Eq. (2.46) into Eq. (2.43). For odd integers, the result is given by symmetric wavefunctions:

$$\psi_n(x) = \sqrt{\frac{2}{L}} \cos\left(\frac{\pi n x}{L}\right), \quad n = \pm 1, \pm 3, \pm 5, \dots \quad (2.48)$$

and for even integers the solution is given by anti-symmetric wavefunctions:

$$\psi_n(x) = \sqrt{\frac{2}{L}} \sin\left(\frac{\pi n x}{L}\right), \quad n = \pm 2, \pm 4, \pm 6, \dots \quad (2.49)$$

Fulfilling the requirement of the total probability to find a particle equals one, results in the prefactor of both wavefunctions $\sqrt{2/L}$:

$$\int_{-\infty}^{\infty} |\psi_n(z)|^2 dz = 1. \quad (2.50)$$

Table 2.1 summarizes the lowest four possible energies and the associated wavefunctions. Since the energies calculated by Eq. (2.47) only depend on the square of the quantum number n , it is possible to consider just the positive ones.

Quantum Number	Eigenenergy	Wavefunction
n=1	$\varepsilon_1 = \frac{\hbar^2 \pi^2}{2mL^2}$	$\psi_1 = \sqrt{\frac{2}{L}} \cos\left(\frac{\pi z}{L}\right)$
n=2	$\varepsilon_2 = 4 \cdot \varepsilon_1$	$\psi_2 = \sqrt{\frac{2}{L}} \sin\left(\frac{2\pi z}{L}\right)$
n=3	$\varepsilon_3 = 9 \cdot \varepsilon_1$	$\psi_3 = \sqrt{\frac{2}{L}} \cos\left(\frac{3\pi z}{L}\right)$
n=4	$\varepsilon_4 = 16 \cdot \varepsilon_1$	$\psi_4 = \sqrt{\frac{2}{L}} \sin\left(\frac{4\pi z}{L}\right)$

Table 2.1: Summary of the four lowest available eigenenergies within a quantum well applying infinite barriers.

The introduced example of a quantum well with infinite boundary conditions results in the following three statements [57]:

- **Quantization of energy levels**

The confinement within a quantum well causes discrete energy levels. The distance between the allowed energy levels increases with the eigenenergy.

- **Non-zero ground state energy**

The energy of the lowest energy level has to be greater than zero, because particles located at the lowest energy levels can not have zero energy.

- **Standing waves**

Only standing waves with discrete number of half waves exist between the impenetrable walls.

The potential well with infinite potential barriers is an illustration of an idealized environment. The theory can also be adapted to more realistic cases. A first step is made by reducing the infinite boundary conditions to finite potential barriers as shown in Fig. 2.11. Another case is

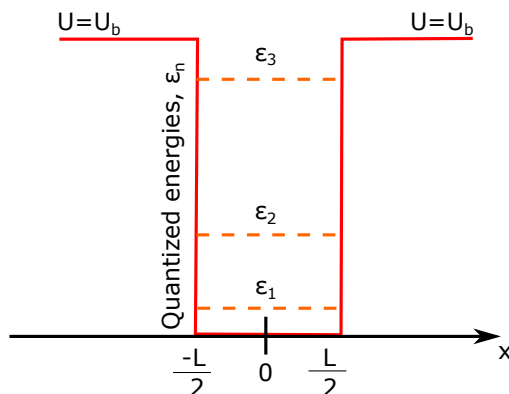


Figure 2.11: One-dimensional quantum well with applied finite potential walls. Solving the Schrödinger equations leads to the quantized eigenenergies ε_n [57].

given by changing the rectangular barrier into quadratic increasing potential walls (see Fig. 2.12). The length L of the potential well now depends on the energy. Since the potential wall is finite the wavefunction penetrates into the forbidden area.

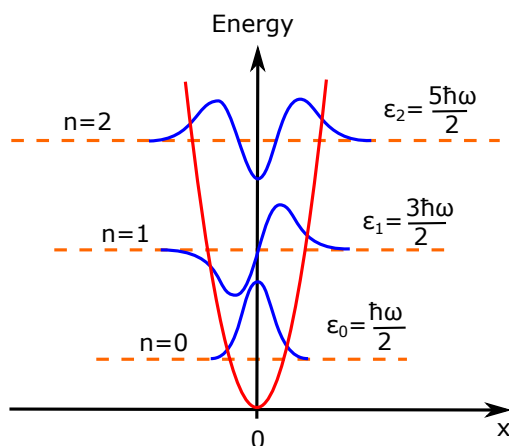


Figure 2.12: One-dimensional quantum well with parabolic potential walls. Shown are the resulting eigenenergies and eigenfunctions [57].

2.3.4 Transmission and Reflection

The opposite of a potential well is given for a rectangular potential barrier within a continuous energy spectra (see Fig. 2.13). In this case, the particles are free to move on both sides of the barrier, whereas inside the barrier the particles are not free to move. For this example, the boundary conditions are given by:

$$U(x) = \begin{cases} U_b, & \text{for } |x| \leq \frac{L}{2}, \\ 0, & \text{for } |x| > \frac{L}{2}, \end{cases} \quad (2.51)$$

where L is the barrier width and U_b is the barrier height. According to the wave theory, incoming waves from the left side can be reflected by the potential barrier or can transmit through the barrier into the right side of the barrier. In order to estimate the number of particles reflected and transmitted by the barrier, the numbers are counted in ratios of the reflected i_r and transmitted i_t particles of the total incoming flux i_i :

$$R(\varepsilon) = \frac{i_r}{i_i}, \quad (2.52)$$

$$T(\varepsilon) = \frac{i_t}{i_i}. \quad (2.53)$$

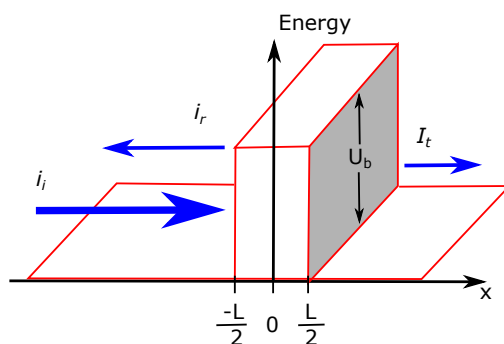


Figure 2.13: Potential barrier within a continuous energy spectra [57].

The entire flux is calculated by Eq. (2.33), which requires the calculation of eigenfunctions ψ . The energy intervals are separated into two parts. One interval describes energies lower than the energy barrier $0 < \varepsilon < U_b$. In classical physics the waves of these energies are totally reflected $R = 1$ and the transmission is zero $T = 0$. The other energy interval includes all energies higher than the barrier $\varepsilon > U_b$. These waves are free to move and easily overcome the barrier, thus $R = 0$, $T = 1$.

Quantum mechanical effects have to be taken into account for small dimensions and therefore the Schrödinger equation (see Eq. (2.36)) is solved. The wave mechanics are obtained by

applying the potential description of Eq. (2.51), which leads to the following three cases:

$$\psi(x) = \begin{cases} e^{ikx} + re^{-ikx}, & x < -\frac{L}{2}, \\ ae^{-\kappa x} + be^{\kappa x}, & \text{for } -\frac{L}{2} \leq x \leq \frac{L}{2}, \\ te^{ikx}, & \frac{L}{2} < x. \end{cases} \quad (2.54)$$

There are two waves on the left side of the barrier, the incident wave described by e^{ikx} and the reflected wave, re^{-ikx} . The transmitted wave $\psi = te^{ikx}$ only exists on the right side of the barrier. The exponential factor of the waves is obtained by:

$$k = \frac{\sqrt{2m_0\varepsilon}}{\hbar}, \quad \kappa = \frac{\sqrt{2m_0(U_b - \varepsilon)}}{\hbar}. \quad (2.55)$$

Waves with eigenenergies lower than the barrier energy $\varepsilon < U_b$ are described by a real value κ whereas the other eigenenergies $\varepsilon > U_b$ are described by an imaginary value κ . The wave defining parameters x , a , b , t depend on the eigenenergy ε and need to be calculated by solving the boundary value problem. Therefore, the waves and their derivatives have to match the boundary conditions at the barrier $x = \pm L/2$. By introducing the relationship of reflecting and transmitting waves $R + T = 1$ and solving Eq. (2.54), the transmission coefficient for both types of energy intervals is as following [57]:

$$T = \frac{1}{1 + \left(\frac{k^2 + \kappa^2}{2k\kappa}\right)^2 \sinh^2(2\kappa L)}, \quad \varepsilon < U_b, \quad (2.56)$$

$$T = \frac{1}{1 + \left(\frac{k^2 - K^2}{2kK}\right)^2 \sin^2(2KL)}, \quad \varepsilon > U_b, \quad (2.57)$$

with $K^2 = -\kappa^2$. Investigating the energy below the barrier energy and applying classical physics where $\hbar \rightarrow 0$, leads to $\kappa \rightarrow \infty$, $\sinh(2\kappa L) \rightarrow \infty$ and finally to the result that no particles are able to transmit through the barrier $T \rightarrow 0$. But this simplification is only valid for wide and high barriers ($U_b, L \rightarrow \infty$). Since \hbar is obviously not 0 but a finite value, a finite tunneling probability is always guaranteed.

The other case is given by considering energies above the barrier, where classic physics assume an ideal transmission $T = 1$. This is only valid for the case of $\sin(2KL) = 0$ which is given for $2KL = \pi n$ ($n \in \mathbb{N}$). For the other cases, the transmission is smaller than one $T < 1$. This means that there is a particle reflection even for energies larger than the energy barrier [57]. Fig. 2.14 shows the transmission coefficient for two barrier widths. The transmission is almost zero for energies far below the barrier height. The transmission increases sharper for the device with a bigger barrier width $L = 2$ nm than for the small barrier width $L = 1$ nm due to less barrier tunneling. For energies greater than the energy barrier $\varepsilon > U_b$, the transmission is almost 1. The overbarrier reflection of particles is a quantum mechanical effect and results in an oscillating transmission at energies slightly above the energy barrier [57].

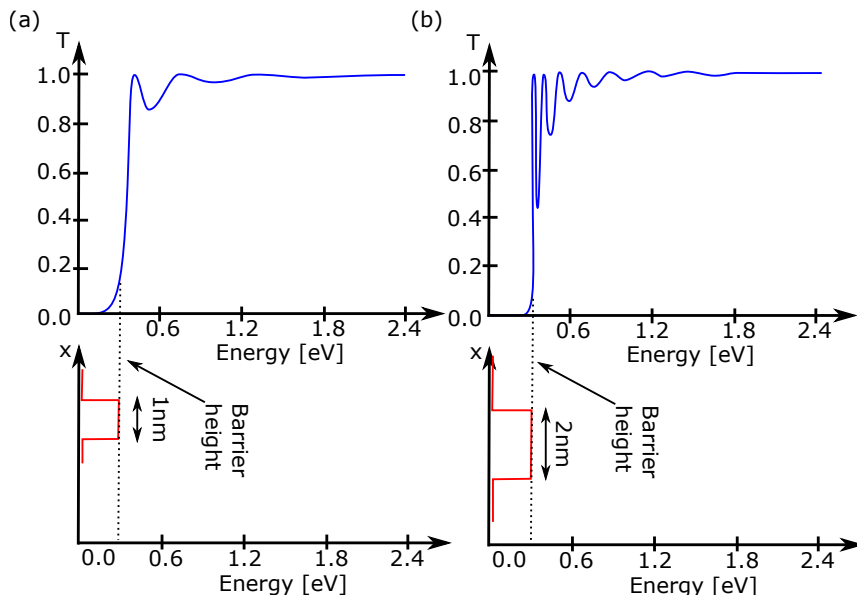


Figure 2.14: Transmission coefficient of a particle for different energies. Figure (a) considers a barrier width of $L = 1$ nm, and (b) a barrier width of $L = 2$ nm [57].

2.3.5 The one-Level Device

In the following, a device which consists of a source, drain and channel region is assumed. The source and drain region are filled with a continuous density of states, whereas the channel is described by only one level ε . Adding a bias qV_{ds} to the contacts lowers the energy levels in the drain region and the Fermi level of each contact is separated by [58]:

$$E_{F1} - E_{F2} = qV_{ds}, \quad (2.58)$$

and both Fermi functions are given by:

$$F_1(\varepsilon) = \frac{1}{1 + e^{\frac{\varepsilon - E_{F1}}{k_b T}}}, \quad (2.59)$$

$$F_2(\varepsilon) = \frac{1}{1 + e^{\frac{\varepsilon - E_{F2}}{k_b T}}}. \quad (2.60)$$

This non-equilibrium forces the Fermi function of each contact to bring the device into equilibrium with itself. The source contact E_{F1} tries to fill the device with electrons in order to achieve equilibrium with the device. On the other side, the drain Fermi function E_{F2} tries also to achieve equilibrium conditions and consequently pulls electrons out of the device. In this non-equilibrium case, the device is held in the middle of both Fermi functions, where one side

pumps electrons into it and the other side pulls electrons out of it. The number of electrons N

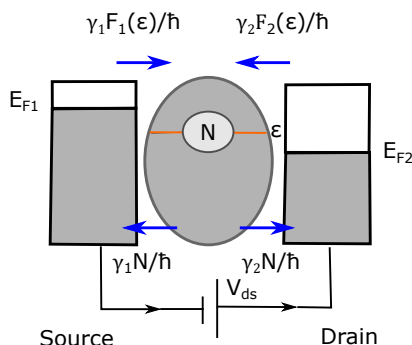


Figure 2.15: Sketch of a one-level device showing the flux of electrons into and out of the device [58].

is described by the average of the source and drain Fermi function. The pushing of electrons of the source Fermi function leads to a resulting current I_1 which depends on the electrons located inside the channel:

$$I_1 = (-q) \frac{\gamma_1}{\hbar} (F_1 - N), \quad (2.61)$$

with q is the electron charge. The current I_2 on the drain side is obtained equally by the drain Fermi function, which pulls electrons out of the device:

$$I_2 = (-q) \frac{\gamma_2}{\hbar} (F_2 - N). \quad (2.62)$$

An electron located at the level ϵ escapes into the source contact by the escape rate γ_1/\hbar and into the drain contact by γ_2/\hbar . For a steady state condition, the absolute value of the current entering the device has to be as big as the current leaving the device $I_1 + I_2 = 0$. By applying this condition to both currents of Eq. (2.61) and Eq. (2.62), the number of electrons is defined by:

$$N = \frac{\gamma_1 F_1 + \gamma_2 F_2}{\gamma_1 + \gamma_2}. \quad (2.63)$$

The total steady state current is hence given by substituting Eq. (2.63) into Eq.(2.61).

$$I = I_1 = -I_2 = \frac{q}{\hbar} \frac{\gamma_1 \gamma_2}{\gamma_1 + \gamma_2} [F_1(\epsilon) - F_2(\epsilon)]. \quad (2.64)$$

From this simple equation, the following facts can be derived [58]:

- If both Fermi functions are equal, there will be no current $F_1(\epsilon) = F_2(\epsilon) \rightarrow I = 0$.
- If the energy level ϵ is located way above both Fermi levels, both Fermi functions will be 0 and no current can flow $\epsilon \gg E_{F1}$ and $\epsilon \gg E_{F2} \rightarrow I = 0$.
- If the energy level ϵ is located way below both Fermi levels, both Fermi functions will be

1 and no current can flow $\varepsilon \ll E_{F1}$ and $\varepsilon \ll E_{F2} \rightarrow I = 0$.

- An energy level ε located within a few $k_B T$ between E_{F1} and E_{F2} will lead to current $\mu_1 > \varepsilon > \mu_2 \rightarrow I \neq 0$.

Since one contact tries to fill up the number of electrons from N to F_1 and the other tries to lower the number of electrons from N to F_2 , it is regardless whether the states are filled or empty under equilibrium condition. Either the states are initially filled, drain contact will try to empty them and source contact subsequently refills them. The other case covers states that are initially empty, source contact will try to fill them and drain contact subsequently empty them. Both cases result in a current [58].

In a further step it is necessary to include the level broadening. Broadening describes the process of coupling the device to the contacts. The density of states of the source, channel and drain region is shown in Fig. 2.16. Depicted is a continuous density of states for the isolated source and drain region, whereas the isolated channel is described by only one sharp energy level ε [58]. The coupling of the channel to the source and drain region results in an exchange

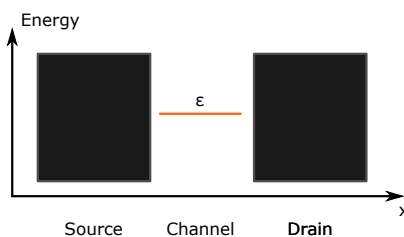


Figure 2.16: Each of the device parts source, channel and drain is isolated and has its own density of states [58].

of the energy levels. Some of the channel's states spread into the source and drain region, whereas some states of the source and drain spread into the channel region. This effect causes a broadening of the channel energy level because the level loses states at its fix energy, whereas it gains states over a range of energy. Fig. 2.17 shows the transition of the isolated channel to the coupled channel with its broadened states [58]. The former sharp energy level is the

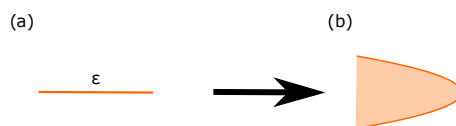


Figure 2.17: (a) Illustration of a sharp energy level ε which is broadened to a continuous density of states (b) [58].

limiting case for $\gamma \rightarrow 0$, which gets broadened from a delta function to a Lorentzian function. Its center energy equals the energy of the former delta function ε . The overall exchanges of states show that the channel gains as much states as it loses by the coupling to the contacts

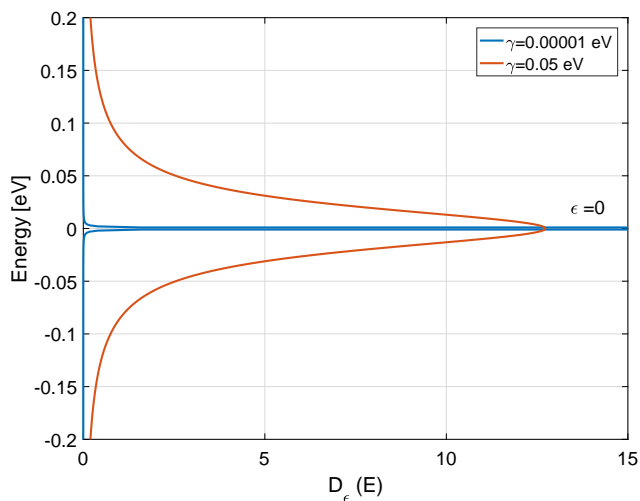


Figure 2.18: Computation of the energy level almost without broadening by $\gamma = 0.00001$ eV and by including the broadening $\gamma = 0.05$ eV.

and therefore, the number of states remains constant and is only spread over a bigger range of energy. The density of states of the broadened energy levels is defined by (see Fig. 2.18) [58]:

$$D_\varepsilon(E) = \frac{\gamma/2\pi}{(E - \varepsilon)^2 + (\gamma/2)^2}. \quad (2.65)$$

A stronger coupling of the channel to the contacts results in a stronger broadening of the energy level and the total broadening is obtained by $\gamma = \gamma_1 + \gamma_2$ introduced in Eq. (2.61). This correlation is defined by a full quantum mechanical treatment but can also be seen as a consequence of the uncertainty principle introduced in section (2.1.4).

By applying a small voltage to both contacts, both Fermi levels are separated by qV_{ds} . Due to the connection of the channel to the source and drain region, some states spread out of the range between E_{F1} and E_{F2} (see Fig. 2.19). This implies that states out of the range between both Fermi levels can contribute to a conducting solid. By including the level broadening of Eq. (2.64), the current becomes energy dependent. To receive the total current an integration over energy is mandatory:

$$I = \frac{q}{\hbar} \int_{-\infty}^{+\infty} D_\varepsilon(E) \frac{\gamma_1 \gamma_2}{\gamma_1 + \gamma_2} [F_1(E) - F_2(E)] dE. \quad (2.66)$$

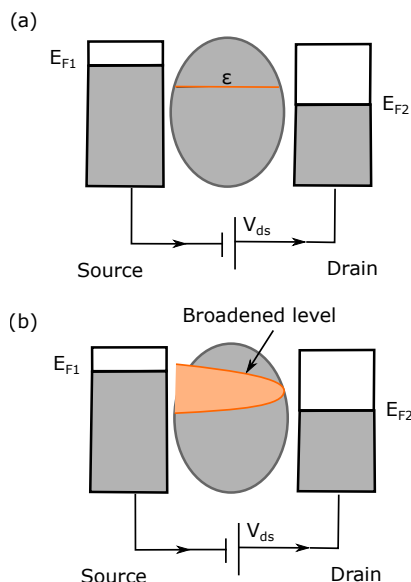


Figure 2.19: a) Isolated channel energy level. b) Broadening of the channel energy level due to the connection with the source and drain region leading to states out of the range between E_{F1} and E_{F2} [58].

2.3.6 Potential Profile of the one-Level Device

One of the main challenges is to compute the potential inside the device. This section explains the iterative method in order to point out the present problem, even though iterations are not allowed in a well developed compact model. The former assumptions are made for a single and constant energy level without the consideration of a potential profile from source to drain. The potential within the channel is shaped by the applied contact voltages (source, drain, gate) and consequently moves the energy level in the channel up and down. Depending on the applied gate bias, the energy level ϵ can be shifted up and down to different energies. For the case of a positive gate voltage ($V_{gs} > 0$), the energy level is located between both Fermi levels and contributes to a conducting solid (see Fig. 2.20(a)). For a negative gate voltage ($V_{gs} < 0$) the energy level has a higher energy than both Fermi levels and does not contribute to a conducting solid [58]. Assuming an insulating channel, Laplace's equation can be applied, leading to the electrostatic potential $U = q \cdot V$ [58]:

$$\nabla \cdot (\epsilon_r \nabla V) = 0. \quad (2.67)$$

In this introductory example, the potential inside the channel is assumed to be a single point. By introducing the contact voltages, $V_s = 0$ is the source contact, V_d is the drain contact and V_g is the gate contact, the channel potential can be calculated according to the devices

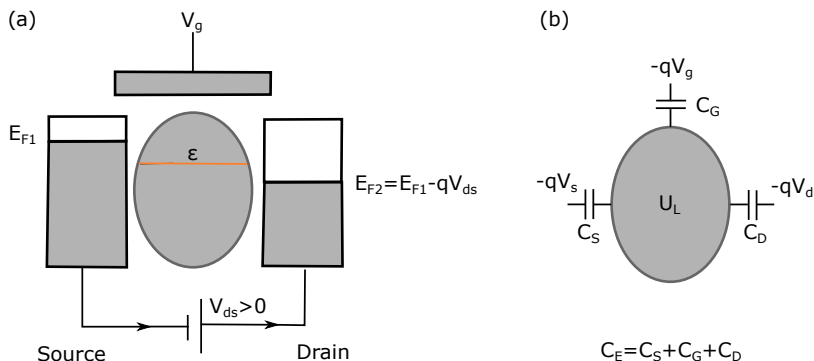


Figure 2.20: (a) Transistor model containing one energy level. (b) Capacitance for the transistor which affect the Laplace potential inside the channel [58].

capacitances as shown in Fig. 2.20(b). Multiplying the electron charge $-q$ with the electrostatic potential, results in the potential energy for the Laplace case U_L [58]:

$$U_L = \frac{C_G}{C_E}(-qV_G) + \frac{C_D}{C_E}(-qV_D), \quad (2.68)$$

with C_G , C_D , C_S are the capacitances of each contact and C_E is the total device capacitance $C_E = C_G + C_D + C_S$. For the case of electron density variation $\Delta\rho$ around the energies of both Fermi levels inside the channel, Poisson's equation needs to be solved [58]:

$$\nabla \cdot (\epsilon_r \nabla V) = -\frac{\Delta\rho}{\epsilon_0}. \quad (2.69)$$

The change of electrons ΔN is calculated by sharing the potential on each capacitor:

$$-q\Delta N = C_S V + C_G(V - V_G) + C_D(V - V_D). \quad (2.70)$$

The total potential energy is given by the summation of both potentials, namely the Laplace potential and the potential forced by the change of electrons ΔN :

$$U = U_L + \frac{q^2}{C_E} \Delta N. \quad (2.71)$$

The potential within the device shifts the density of states in dependency on the energy and consequently needs to be included in the calculation for the number of electrons N [58]:

$$N = \int_{-\infty}^{+\infty} D_\epsilon(E - U) \frac{\gamma_1 F_1(E) + \gamma_2 F_2(E)}{\gamma_1 + \gamma_2} dE \quad (2.72)$$

and also included in the expression for the current:

$$I = \frac{q}{\hbar} \int_{-\infty}^{+\infty} D_{\varepsilon}(E - U) \frac{\gamma_1 \gamma_2}{\gamma_1 + \gamma_2} [F_1(E) - F_2(E)] dE. \quad (2.73)$$

Since the solution for N , shown in Eq. (2.72), is a function of U and the calculation of U , shown in Eq. (2.71), is a function of N , a time-consuming iterative solution is required (see Fig. 2.21). Whereby the potential is successively approximate to a self-consistent value.

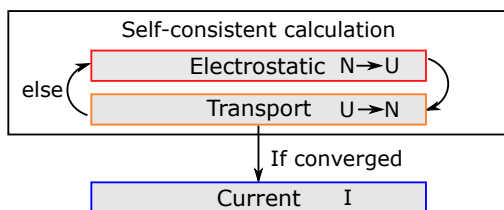


Figure 2.21: Electron concentration N and the potential U is computed by an iterative process. If a self-consistent solution is achieved the current is calculated [37].

2.3.7 Multi-Level Device

The one-level device of the previous section showed the fundamental strategy when considering a nano-scaled transistor. The potential and the single energy level was assumed to be constant along the length of the device. In a further step the rather cavalier assumption is made. It assumes many parallel energy levels, located at different energies, which all conduct independently. The so called multi-level devices as shown in Fig. 2.22, is more related to a real device [58]. Heading to a more realistic device, it is not sufficient to only incorporate more energy

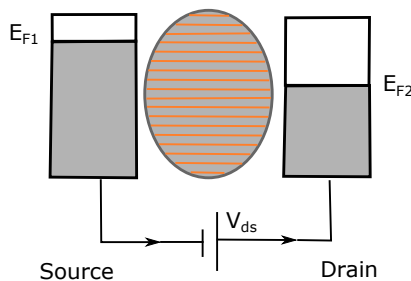


Figure 2.22: Channel of the multi-level device is composed of many independent and parallel energy levels [58].

dependent levels. A further important part is to consider the potential, which depends on the position from source to drain, shaped by the applied biases. A good way to give mathematical

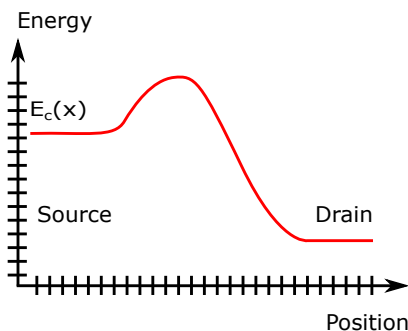


Figure 2.23: The 1D device is partitioned into a position and energy depended grid.

expressions is to represent all former introduced quantities by matrices [58]. The calculation of a device partitioned in n positions is performed by using $n \cdot n$ sized matrices. The new notations are needed to describe the matrices shown in Table 2.2. The density of states of the single level device $D_\varepsilon(E)$ is exchanged with the total density of state $D(E)$. As shown for the one-level device, the level broadening of the multi-level device is coupled to the in- and out-scattering functions. For the multi-level device both functions are summarized in the Σ -matrices.

One-Level Device	NEGF formalism	NEGF Titling
ε	\mathbf{H}	Hamiltonian matrix
γ_i	$\mathbf{\Gamma}_i(\mathbf{E})$	Broadening matrix
$2\pi D(E)$	$\mathbf{A}(\mathbf{E})$	Spectral function
$2\pi n(E)$	$\mathbf{G}^n(\mathbf{E})$	Correlation function
U	\mathbf{U}	Potential matrix
N	ρ	Density matrix

Table 2.2: Notation transition from the one-level device to multi-level description. For the one-level device each symbol describes a number, whereas the multi-level is described by matrices.

The replacement of the symbols by matrices leads to the NEGF formalism introduced in Sec. 4.2, which are related to those of the one-level device [58]. As shown in Fig. 2.23 an accurate potential profile from source to drain is mandatory to calculate the resulting current. The iterative formalism presented in Fig. 2.21 is not suitable for compact models and therefore, the potential shape needs to be solved in a closed-form (see Sec. 5). This closed-form potential solution is based on the mathematical preliminaries introduced in a prior step (see Sec. 4.1).

CHAPTER 3

Physics and Simulation Approach of Advanced MOSFETs

The ongoing geometry scaling allows higher transistor densities within microchips. Further scaling of short-channel devices leads to less electrostatic control within the channel and comes consequently hand in hand with SCEs [18]. Single-gate transistors as shown in Fig. 3.1 have been used for designing microchips since the invention of the MOSFET. One opportunity to overcome these drawbacks of downscaling is to increase the number of gates. The single-gate transistor has therefore been developed towards a multiple-gate transistor. Multiple-gate transistors increase the influence on the channel's electrostatics and consequently achieve a reduction of SCEs [59]. The future is seen in the surrounding gate devices or also known as gate-all-around (GAA) devices, because they gain the best electrostatic control. However, from a technological point of view, they are complicated to manufacture. Today's state-of-the-art design is the FinFET, which is physically based on a DG structure with a top gate [60]. A further reduction of the channel length below 10 nm leads to the ultra-scaled devices. For these devices the electrical behavior is affected by quantum effects. A further emerging device is the TFET. In this case, the tunneling current describes the main charge transport and not a parasitic effect. This work focuses on the DG transistor structure which is applied for the ultra-short MOSFET shown in Sec. 3.1 as well as for the TFET introduced in Sec. 3.2.

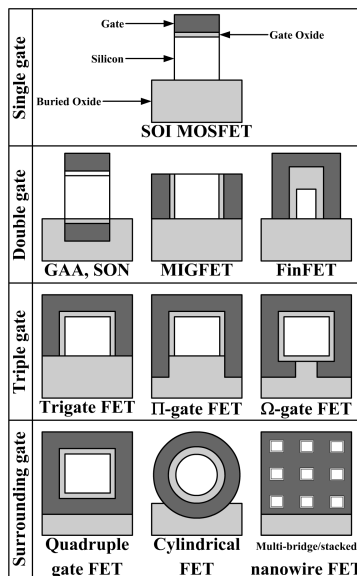


Figure 3.1: Several possible device and gate structures [59] [61].

3.1 Ultra-Scaled MOSFETs

The main focus of this study is on the DG MOSFET having the geometry shown in Fig. 3.2. The channel length l_{ch} of the DG MOSFET is assumed to be in a range of 6 nm to 30 nm. Since the concept of ballistic charge transport can be used for ultra-short devices, this concept is introduced in Sec. 3.1.1. The previously mentioned quantum based SD tunneling is a major quantum effect which influences ultra-short channel devices and is therefore introduced in Sec. 3.1.2. The approach to develop a analytical model based on quantum mechanical charge transport is explained in Sec. 3.1.3.

3.1.1 Ballistic Charge Transport

Applying an electric field to a semiconductor, electrons are accelerated and move through the device. On their way from source to drain, they get scattered leading to a change of the electrons momentum (see Fig. 3.3(a)). With shrinking the device length to a few nanometers, the mean free path becomes comparable to the dimension, consequently more and more electrons are able to pass the device without scattering (see Fig. 3.3(b)) [19]. Since ultra-short MOSFETs are in the center of interests, the concept of a ballistic charge transport is applied in the following. A semiclassical view on the charge transport across the MOSFET device is shown in Fig. 3.4. The figure introduces the ballistic case for Boltzmann transport equation for a typical MOSFET with a highly doped source and drain region. Both Fermi levels are separated by the applied

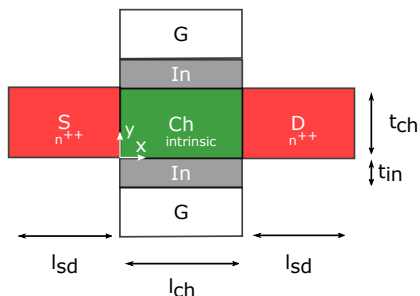


Figure 3.2: Cross-section of the considered ultra-short DG MOSFET. Shown are both gates G , the insulator In , the intrinsic channel Ch , the constant doping profiles of the source S and drain region D . The length of the source and drain region is described by l_{sd} , the channel length is named l_{ch} and the channel thickness is given by t_{ch} .

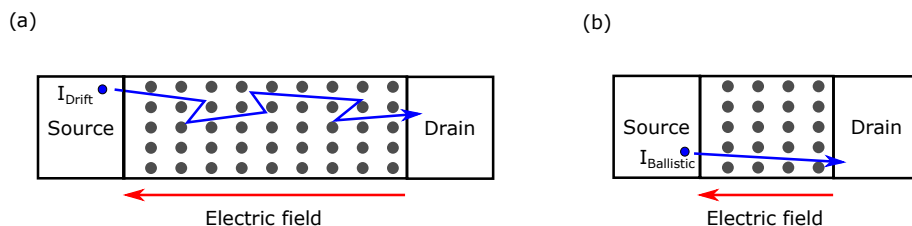


Figure 3.3: Illustration of charge transport, (a) for considering scattering, (b) for the ballistic case.

drain bias $q \cdot V_{ds}$. The barrier located within the channel modulates the electron flow. Increasing the barrier by applying a negative gate voltage $V_{gs} < 0$ reduces the current flow, leading to the off-state. The leakage current is formed by the electrons which still gain enough energy and overcome the barrier. Lowering the barrier by applying a positive gate voltage $V_{gs} > 0$ increases the current flow and the transistor is turned on. When considering the semiclassical case, the density of states inside the device is given for each position above the bottom of the conduction band. Assuming a basic band structure the $E - k$ relation is described by a parabolic one. In this semiclassical case the density of states is assumed, whereas in Sec. 4.2 the density of states is calculated by quantum mechanics. The density of states is filled up by the Fermi function of both contacts. Due to the ballistic transport and the fact that electrons in a semiclassical treatment are not able to tunnel through the barrier, the occupation of states can be described in a certain way. The positive k -states having an energy higher than the barrier $E > E_{barrier}$ are filled by the source Fermi function E_{F1} . The negative k -states are filled by the drain Fermi function E_{F2} , additionally some part gets reflected by the barrier and fills the positive k -states having an energy lower than the barrier $E < E_{barrier}$ [62].

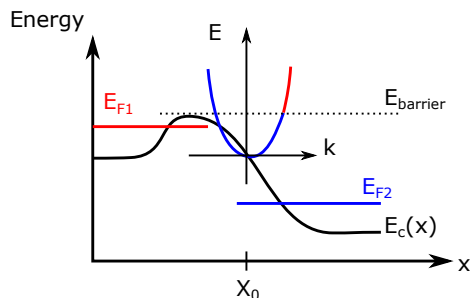


Figure 3.4: Semiclassical view of the transistor. A parabolic $E - k$ relation is assumed across the entire device [63].

3.1.2 Source-to-Drain Tunneling Current

In semiclassical physics the leakage current of MOSFETs is given by the electrons overcoming the barrier in the off-state. By shortening the channel length, the length of the barrier gets also reduced. For a barrier length coming into the nanometer range, a quantum mechanical effect occurs. The barrier tunneling, introduced in Sec. 2.3.4, allows electrons to tunnel from the source side, through the barrier, into the drain side of the device and is therefore named as SD tunneling current (see Fig. 3.5). The basic concept of the MOSFET is to control the

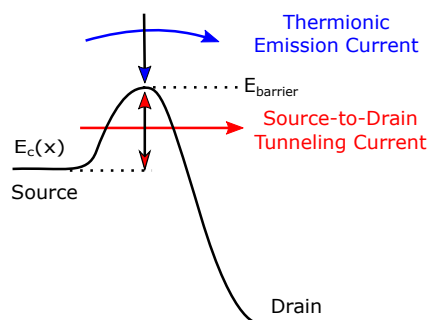


Figure 3.5: Thermionic emission current and SD tunneling current of a short-channel transistor [34].

device current by modulating the barrier height. The resulting device current is consequently linked to the applied gate voltage. This concept leads to a steepest subthreshold slope of 60 mV/dec, which means that the current increases by the factor of 10 due to an increase of the gate voltage by 60 mV. The SD tunneling current causes a higher leakage current I_{off} (see Fig. 3.6) and therefore lowers the subthreshold slope [64]. Hence, the SD tunneling effect may lead to the ultimate scaling of MOSFETs [23]. Some researchers capture this effect by using

the density gradient formalism by calibrating their results using the NEGF formalism [35]. In order to incorporate this tunneling in a physically fundamental way, a transistor model based on quantum mechanics is derived.

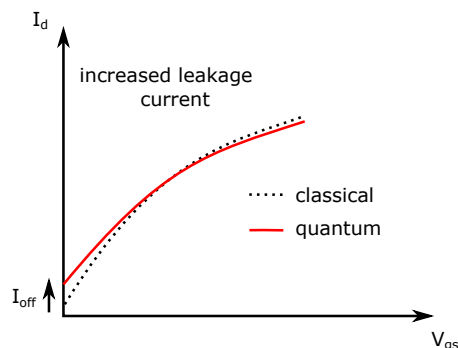


Figure 3.6: The leakage current for ultra-short MOSFETs increases when considering quantum based charge transport in contrast to classical charge transport [62].

3.1.3 MOSFET Multi-Scale Simulation Approach

The quantum based transistor model is derived by combining the advantages of the compact models with those of quantum based numerical simulators. Hence, it is possible to calculate thermionic emission current as well as quantum mechanical SD tunneling current of ultra-short DG MOSFETs.

Physics-based compact models make use of the Poisson solution in order to predict an accurate potential shape of the device without iterations. Applying this potential and a classical transport equation for example the Boltzmann transport equation, the current can be calculated without iterations (see Fig. 3.7(a)). The advantage of the NEGF based transport solver, applied for numerical simulations, is the ability to calculate the SD tunneling of ultra-short transistors (see Fig. 3.7(b)). The drawback of this simulation is the iterative solution. In a first step, the Poisson solver guesses a shape for the potential. The transport solver calculates the electron density inside the device based on the potential guess. This is followed by the Poisson solver to calculate the potential based on the electron density. The calculated potential is compared with the guessed potential, leading to an improved potential guess. The process is repeated until the calculated potential and the potential guess converges.

The goal is to combine the advantages of compact models and quantum based simulations (see Fig. 3.7(c)). The NEGF based analytical MOSFET model skips the time consuming iterative coupling due to a precise closed-form potential solution followed by the NEGF based transport solver. As a result of neglecting the iterations and turning the formalism into a straightforward calculations, the algorithm gets much faster and is also suitable for an analytical transistor model.

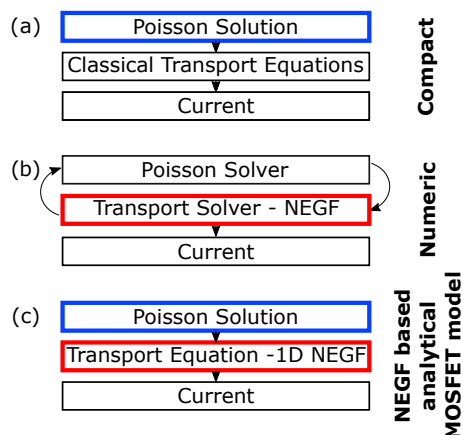


Figure 3.7: Flowchart of (a) compact models using analytical solved equations. (b) Common numerical NEGF models which iterate between transport and Poisson solver. (c) NEGF based analytical MOSFET model combines standard compact models and numeric device simulations.

3.2 Tunneling Field-Effect Transistor

In contrast to the MOSFET, the TFET is not based on the charge transport above a barrier, more precisely it is based on the charge transport through a barrier. Due to the carrier transport caused by the b2b tunneling effect, a subthreshold slope steeper than 60 mV/dec at a temperature of $T = 300$ K can be achieved [25]. Whereas the subthreshold slope of standard MOSFETs, based on thermionic emission current, is always limited to 60 mV/dec. Due to

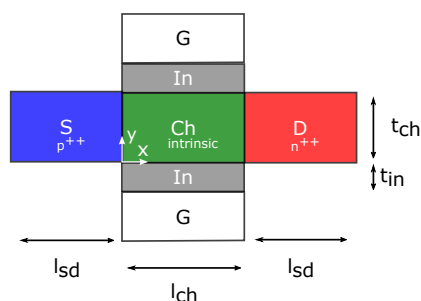


Figure 3.8: Geometry of an n-type DG TFET, showing the doping profiles, source and drain length l_{sd} , channel length l_{ch} , channel thickness t_{ch} and the insulator thickness t_{in} .

the steeper subthreshold slope of the TFET, the supply voltage of integrated circuits can be reduced without increasing the leakage current (see Fig. 3.9). Reducing the supply voltage and additionally lowering the leakage current I_{off} decreases consequently the total power

consumption, which plays an important role for mobile always-on devices [65]. The fabrication of TFETs is more difficult due to the need of steep doping gradients at the channel junctions. Furthermore, there is a general presence of defects at the junctions which causes trap-assisted tunneling (TAT) current [66]. TAT increases the leakage current in the off-state of the device and hence causes a degradation of the subthreshold slope. Nevertheless, the focus in this context is on the on-state and not on the TAT tunneling current.

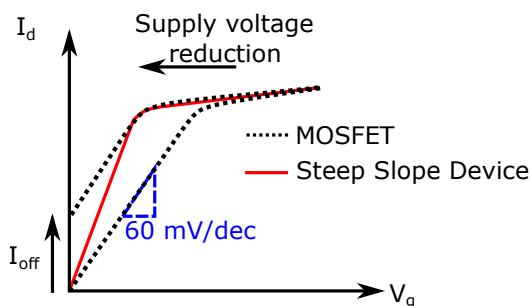


Figure 3.9: Steep slope devices allow a supply voltage reduction without increasing the leakage current I_{off} .

3.2.1 Band-to-Band Tunneling Current

The TFET consists of two opposite doped source and drain regions. For the n-type TFET the source region is heavily p-doped and the drain region is n-doped, whereby the channel stays intrinsic. For a p-type device the doping of the source and drain region is done vice versa. A schematic band structure is shown in Fig. 3.10. The gate electrode shifts the conduction band and the valence band within the channel region up and down. The off-state in Fig. 3.10(a) shows a long distance between both bands l_{tun} and therefore almost no carriers can tunnel from the valence band in the source region through the forbidden zone into the conduction band within the channel region. As described in [66], TAT can occur at the junctions and increases the leakage current but is not considered in the modeling approach. Increasing the applied gate voltage V_{gs} , both bands within the channel region are lowered (see Fig. 3.10(b)). The distance between the valence band within the source region and the conduction band is shrunk to a few nanometers and consequently electron based b2b tunneling current can occur. A further decrease of the gate voltage leads to the ambipolar-state (see Fig. 3.10(c)). In this case holes can tunnel from the drain region into the channel. Since the b2b tunneling current occurs at the channel junctions, the potential at these positions needs to be modeled accurately.

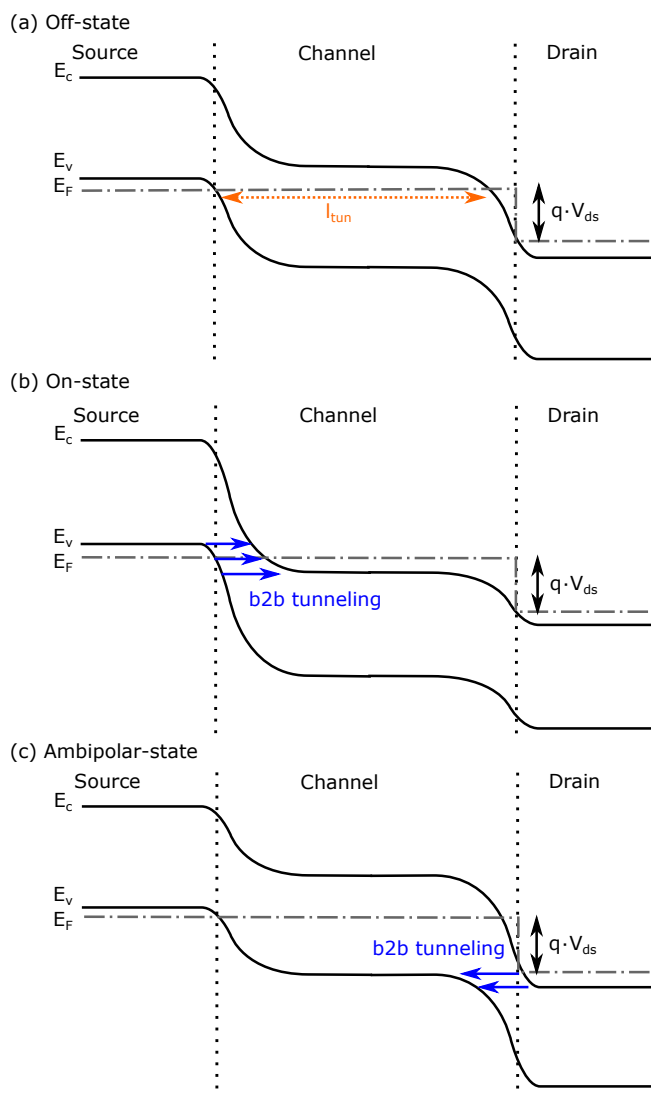


Figure 3.10: Schematic band structure of the DG TFET showing (a) the off-state, (b) the on-state and (c) the ambipolar-state.

Figure 3.11 shows the current transfer characteristic of the TFET for the three mentioned operation regimes. Since the on-state current is formed by the b2b tunneling current from the source region into the channel region, the device on-state current is less affected by the applied drain bias V_{ds} . The ambipolar current occurs at the drain side of the device and is consequently more affected by the drain bias V_{ds} in the transfer characteristic.

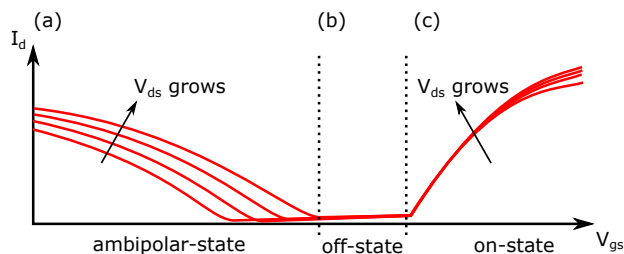


Figure 3.11: Current transfer characteristic of the TFET device showing (a) the ambipolar-state, (b) the off-state and (c) the on-state.

3.2.2 TFET Multi-Scale Simulation Approach

Common compact models for TFETs are based on the combination of Poisson solution in order to calculate the potential inside the device and a transport equation to predict the b2b tunneling (see Fig. 3.12(a)). The b2b tunneling current is commonly calculated by the Wentzel-Kramers-Brillouin (WKB) approximation [67] and Kane's equation [68]. The WKB applies small triangular profiles to approximate the tunneling barrier. With shrinking dimensions the approximation of the potential profile is less accurate than considering the origin potential profile. Since the NEGF formalism inherently includes quantum mechanical effects by applying the origin potential profile, an improvement could be achieved. The concept of using numerical NEGF simulations to consider TFETs was shown by [69]. The combination of an accurate Poisson solution with the quantum mechanical based current calculation leads to the second modeling approach of the thesis (see Fig. 3.12(b)). Therefore, the WKB approximation is exchanged with the NEGF formalism in order to obtain a NEGF based analytical TFET model.

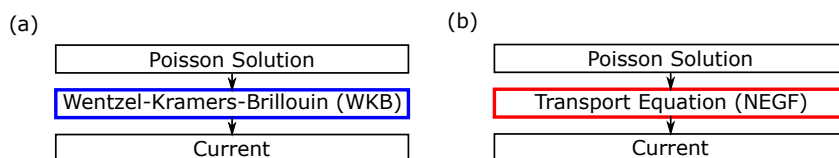


Figure 3.12: Flowchart of (a) common compact TFET models and (b) the hereby introduced NEGF based analytical TFET model.

CHAPTER 4

Mathematical and Physical Derivation

Many physical behaviors can be described mathematically by partial differential equations (PDEs). In general, there are two types of differential equations, the ones that describes a time-dependent relation and the other that are stationary and describe a time-independent relation. For this model the focus is on the time-independent ones that depend on the location. Some specific problems can be solved analytically but other problems need to be solved numerically which leads to model limitations. In the following sections, several opportunities are introduced to handle PDEs based on the references [55] and [70]. Sec. 4.1 shows the mathematical preliminaries for calculating the potential within the channel of a DG MOSFET and in Sec. 4.2 the NEGF formalism is derived.

4.1 Potential Theory

The continuous shrinking of the transistor's dimensions into nanometer region and the simultaneously building of more dimensional device geometries yield to complex electrostatic effects. Parallel to the scaling process, new physical models are constructed which describe these effects. The electrical potential within the channel of a transistor is described by a PDE (see Sec. 4.1.1). One way to solve this PDE analytically is shown hereinafter. Therefore, the complex potential theory (see Sec. 4.1.2) and the conformal mapping technique (see Sec. 4.1.3) is introduced. Solving these equations leads to an accurate potential in the channel region of the DG MOSFET (see Sec. 4.1.4).

4.1.1 Poisson's and Laplace's Equation

The Poisson equation is a common form of a partial differential equation which shows a differential behavior of the second order:

$$\Delta u = -f, \tag{4.1}$$

whereby Δ is the Laplace operator. When considering the homogeneous case $f = 0$, the Poisson equation becomes the Laplace equation:

$$\Delta u = 0. \quad (4.2)$$

The electrostatic behavior within a transistor also depends on these PDEs, the so called Maxwell's equations. One of Maxwell's equations is also known as the Gaussian law and describes the relationship of the electric field and the charge density:

$$\nabla \cdot E(r) = \frac{\rho(r)}{\varepsilon}, \quad (4.3)$$

with ε is the constant permittivity depending on the material. The next important equation describes the physical relation between the electric field E and the potential Φ [70]:

$$E = -\nabla\Phi. \quad (4.4)$$

The substitution of Eq. (4.4) into Eq. (4.3) and solving for Φ leads to the fundamental inhomogeneous Poisson equation, which describes the correlation between the charge density and the potential [70]:

$$\Delta\Phi(r) = -\frac{\rho(r)}{\varepsilon}. \quad (4.5)$$

The potential is given as a linear PDE and depends on the space coordinates. In the case of Cartesian coordinates, the Laplace operator is read as [70]:

$$\Delta = \frac{\partial^2}{\partial x^2} + \frac{\partial^2}{\partial y^2} + \frac{\partial^2}{\partial z^2}, \quad (4.6)$$

which defines Eq. (4.5) more precisely to:

$$\Delta\Phi(x,y,z) = -\frac{\rho(x,y,z)}{\varepsilon}. \quad (4.7)$$

A special case of the electrostatic problem is given for constant dielectric material $\varepsilon = \text{const}$ and a space charge free region. In this case, the Poisson equation (4.7) becomes the Laplace equation [55]:

$$\Delta\Phi(x,y,z) = 0. \quad (4.8)$$

As for all PDEs, there exists infinite solutions for Poisson's and Laplace's equation. The general solution, together with the boundary conditions lead to the particular solution of the problem [70]. This equation can be solved by existing analytical, graphical and experimental solutions, which makes it a special case of PDEs. The boundary conditions of the Laplace equation are separated into two parts and can also be a mixture of both. In the case of mixed boundary conditions, the Neumanns are on one side and the Dirichlet are on the other side [70]:

- In the case of **Dirichlet** boundary conditions, a harmonic function Φ in an enclosed area

is looked for which matches the given value Φ_a at the boundary.

- In the case of **Neumann** boundary conditions, a harmonic function Φ in an enclosed are is looked for which matches the given derivative $\frac{\partial\Phi}{\partial n}|_a$ at the boundary.

4.1.2 Complex Potential Theory

The complex potential theory is a technique to provide an analytical solution of field problems. Considering one point within a 2D plane, it is described in the case of Cartesian coordinates by $z = x + iy$. The corresponding electric field lines are given by fixing z to a constant value. Considering a charge free plane area, the electric field E is given by [71]:

$$\nabla E = \frac{\partial E_x}{\partial x} + \frac{\partial E_y}{\partial y} = 0 \quad (4.9)$$

and can be described by the partial derivation of the potential:

$$E_x = -\frac{\partial\Phi}{\partial x}, \quad E_y = -\frac{\partial\Phi}{\partial y}, \quad \rightarrow \quad E = -\nabla\Phi. \quad (4.10)$$

Additionally, Eq. (4.9) is valid for considering the electric flux ψ :

$$E_x = -\frac{\partial\psi}{\partial y}, \quad E_y = \frac{\partial\psi}{\partial x}, \quad \rightarrow \quad E = -\nabla \times (\psi e_z). \quad (4.11)$$

The electric potential Φ and the electric flux ψ describe the same electric field. Both are linked by the Cauchy-Riemann differential equations [71]:

$$\frac{\partial\Phi}{\partial x} = \frac{\partial\psi}{\partial y}, \quad \frac{\partial\Phi}{\partial y} = -\frac{\partial\psi}{\partial x}. \quad (4.12)$$

The same relationship of x and y can be described by using the complex variables $z = x + iy = re^{i\varphi}$ which describes the same point within a complex z -plane. The theory of complex functions can be applied to solve potential calculations in a plane area. That means that the electric potential and electric flux is given for the real and imaginary part of a complex function [71]:

$$w = w(z) = u(x,y) + iv(x,y). \quad (4.13)$$

The real and imaginary part is defined by real functions depending on x and y . A moving point p_1 within z -plane is mapped by $w(z)$ into w -plane. It is necessary that the moved distance Δz is uniquely defined within the w -plane by Δw . This condition is achieved if the derivation does not depend on the orientation of dz [71]:

$$\frac{dw}{dz} = \lim_{\Delta z \rightarrow 0} \frac{w(z + \Delta z) - w(z)}{\Delta z}, \quad (4.14)$$

which is finally obtained by fulfilling the Cauchy-Riemann differential equation:

$$\frac{\partial u}{\partial x} + i \frac{\partial v}{\partial x} = -i \frac{\partial u}{\partial y} + \frac{\partial v}{\partial y}. \quad (4.15)$$

For the analytical function w , the real and also the imaginary part fulfill the Laplace equation. If one of both functions u and v describes the electric potential, the other describes the electric flux and vice versa. Whereby, the electric field is given by the complex function $w(z)$. The complex potential function in w -plane is given by [71]:

$$w(z) = \Phi(x,y) + i\psi(x,y). \quad (4.16)$$

In the case of Eq. (4.16), the potential function $\Phi(x,y)$ is given by u and the electric field E can be calculated by:

$$E = -\frac{\partial u}{\partial x} - i \frac{\partial u}{\partial y} = -\left(\frac{dw}{dz}\right)^*. \quad (4.17)$$

Figure 4.1 shows the advantage of the mapping technique. The contour line of the potential and flux is given by curves within z -plane Fig. 4.1(a). The contour line are turned into straightforward lines within w -plane Fig. 4.1(b). The perpendicularity of Φ and ψ is still achieved within both planes.

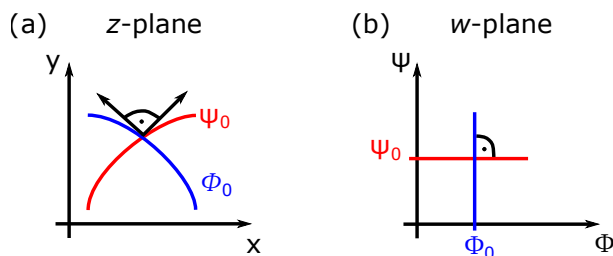


Figure 4.1: (a) Shown is the z -plane, where Φ and ψ are perpendicular and both depend on x and y . (b) Within the w -plane the perpendicularity is still given and the axes are labeled by Φ and ψ . The mapping turns the curves within z -plane into straightforward lines within w -plane.

4.1.3 Conformal Mapping Technique

The conformal mapping technique is needed to transform a well known geometry from its origin z -plane to w -plane. The geometry is mapped with the help of an analytical function $w(z)$ and loses its complexity in its new plane:

$$z = x + iy, \quad (4.18)$$

$$w = u + iv. \quad (4.19)$$

Due to less complexity within the w -plane, the shape of the potential can be calculated much easier. For describing transistors, this transformation is needed to calculate the potential within the channel area of the DG MOSFET. To verify the analytical transformation, the continuous potential within the z -plane, has to be continuous within w -plane as well. That implies that Poisson's equation and its integration is valid in z -plane as well as in w -plane. Due to the transformation of Eq. (4.16), the electrostatic potential and electrical flux is described by u and iv :

$$w(u,v) = \Phi(u,v) + i\psi(u,v). \quad (4.20)$$

In the following, the general transformation of an arbitrary polygon from the z -plane into the w -plane is introduced. The Schwarz-Christoffel transformation maps the polygon from its origin z -plane into the upper half of the w -plane. As shown in Fig. 4.2, the boundaries of the polygon in z -plane are distributed in a 2D shape, whereas in the w -plane all boundaries are mapped on the real axis u . Since the boundaries are located now next to each other, the complex potential can be calculated more conveniently. The mapping is done by changing each angle γ_1 to γ_n of the polygon. In order to perform this mapping, the associated differential $\frac{dz}{dw}$ of the polygon needs to be calculated [55] [71]:

$$\frac{dz(w)}{dw} = C \cdot (w - w_1)^{-\gamma_1} (w - w_2)^{-\gamma_2} \dots (w - w_v)^{-\gamma_n} \quad (4.21)$$

$$= C \cdot \prod_{(m)} (w - w_m)^{-\gamma_m}, \quad (4.22)$$

whereby $z = f(w_m)$ are the vertexes of the polygon, having an angle of γ_m , C is the constant scale and rotation factor and m is altered from 1 to n . The integration of Eq. (4.22) leads to the transformation function:

$$z(w) = C \int \prod_{(m)} (w - w_m)^{-\gamma_m} \cdot dw + D. \quad (4.23)$$

The integration constant D is the origin coordinate in z -plane. As shown in Fig. 4.2, the rotation of a vertex m of the polygon is given by the angle γ . The constant C can be calculated by considering two points located in infinity, the distance between both points is given by [55]:

$$z''_n - z'_n = i\pi C \cdot \prod_{(m \neq n)} (w_n - w_m)^{-\gamma_m}, \quad (4.24)$$

with $\gamma_n = +1$ and $z_n = \infty$. In that case $u_v = \pm\infty$ and Eq. (4.24) can be reduced and the distance between the parallel lines is given by:

$$z''_n - z'_n = i\pi C, \quad (4.25)$$

which leads directly to C . A shape consisting out of N vertexes within z -plane consists of w_n points within w -plane. Both integrations yield to two unknown integration constants C and D .

The approach allows to choose three parameters freely, hence $N - 1$ parameters have to be solved by using Eq. (4.24) and Eq. (4.25). Applying the calculated parameters C and D the

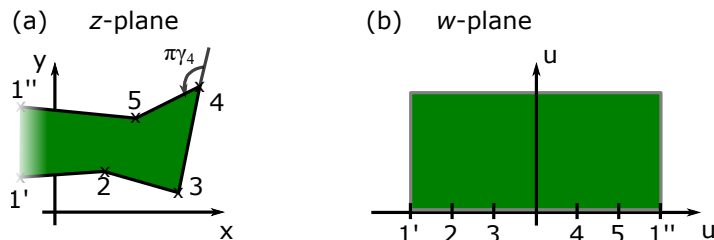


Figure 4.2: Transformation of a polygon from z -plane (a) into w -plane (b).

integration of Eq. (4.23) can be performed. After the integration, the inverse of the function can be built. The inverse function $w(z)$ is inserted into the complex potential of the upper w -plane and leads to the complex potential within z -plane [71]:

$$w(z) = f^{-1}(z(w)). \quad (4.26)$$

4.1.4 Potential Solution

The former section showed a method to map a rather complicated geometry into another plane where the electrostatic potential can be calculated more easily. Therefore, the Poisson integral within w -plane is introduced hereinafter. As mentioned before, the potential is described by its boundary conditions and in general both boundary conditions are mixed and magnify the challenge to find a solution. For the purpose of this potential solution, the boundary conditions are chosen to be Dirichlet ones. In this case, the potential at some specific positions is predefined and the potential φ within the channel area is looked for. The analytical and closed-form solution for the potential within w -plane is given by the Poisson integral:

$$\varphi(w) = \varphi(u,v) = \frac{1}{\pi} \int_{-\infty}^{+\infty} \frac{v}{(u - \bar{u})^2 + v^2} \cdot \phi(\bar{u}) d\bar{u}. \quad (4.27)$$

Since, the potential is calculated in w -plane, the associated boundary conditions along the given geometry are also mapped into w -plane by:

$$\phi(\bar{u}) = \phi(w(\bar{z})). \quad (4.28)$$

This Poisson integral can be partitioned by the N vertexes of the mapped geometry. For example, the section from point \bar{u}_1 to \bar{u}_2 is given by:

$$\varphi(w) = \varphi(u,v) = \frac{1}{\pi} \int_{\bar{u}_1}^{\bar{u}_2} \frac{v}{(u-\bar{u})^2 + v^2} \cdot \phi(\bar{u}) d\bar{u}. \quad (4.29)$$

After the solution is found, the potential $\varphi(w)$ is mapped back into z -plane $\varphi(z) = \varphi(x,y)$:

$$\varphi(z) = \varphi(z(w)). \quad (4.30)$$

4.2 Non-Equilibrium Green's Function

The NEGF formalism provides a basis to perform atomic-level quantum mechanical simulations, which will be needed for future device simulations. The formalism can consequently be applied to consider transistors which are downscaled to the atomic region [36]. Additionally, the formalism allows to apply complicated Hamiltonians like the sp^3s^* , which can be used to describe the valence band, and also the $6-31G^*$ Hamiltonian, which provide a description of molecular conductors [42]. Nevertheless, the focus is on a parabolic conduction band and therefore the effective mass Hamiltonian is applied.

Since the goal is to calculate the current based on quantum mechanical equations, the ballistic NEGF formalism is now introduced in detail. The formalism is based on the finite difference approximation, derived in Sec. 4.2.1, which is a computational formalism to solve PDEs. Based on the finite difference approximation, the Hamiltonian matrix is introduced in Sec. 4.2.2. In a first step, the focus is on a potential well by applying infinite wall boundary conditions in Sec. 4.2.3. In a second step the open boundary conditions are applied in Sec. 4.2.4 and the dispersion relation is adjusted in Sec. 4.2.5. Based on the open boundary conditions the retarded Green's function is built in Sec. 4.2.6. Finally, in Sec. 4.2.7, the electron density is derived. The NEGF formalism provides a numerical way to treat scattering which is shown in Sec. 4.2.8.

4.2.1 Finite Difference Approximation

When simulating transistors using the NEGF formalism, a major task is to solve a PDE and therefore the finite difference approximation is a possible solution. The method can be applied for differential equations described by an initial value problem (IVP), also called Cauchy problem, and boundary value problems (BVP). The numeric method approximates discrete results of the differential equation for independent variables. At the end, the results need to be checked because they are approximations and include calculation errors. In this case, the focus is on the time-independent one [72] [73].

A general example of a 1D stationary differential equation is given by:

$$0 = a \frac{d^2 T(x)}{dx^2} + s(x) \cdot T(x), \quad (4.31)$$

fixed by the boundary conditions $T(x=0) = T_0$ and $T(x=l) = T_N + 1$. As well known, the derivation of a function $f(x)$ can be expressed by the algebraic equation:

$$f'(x) = \lim_{\Delta x \rightarrow 0} \frac{f(x + \Delta x) - f(x)}{\Delta x}. \quad (4.32)$$

A discretization of the grid with a fixed step size results in a certain number of mesh points. For small but not infinitesimal small Δx , the solution becomes acceptable and can be expressed by:

$$f'(x) \approx \frac{f(x + \Delta x) - f(x)}{\Delta x}. \quad (4.33)$$

The Taylor series describes the value of a function f at the position $x + \Delta x$ or $x - \Delta x$ by using a known value $f(x)$ and its derivatives $f'(x), f''(x), \dots$ located at the position x . Taking the distance to the positive mesh point is named as the forward difference:

$$f(x + \Delta x) = f(x) + \frac{\Delta x}{1!} f'(x) + \frac{\Delta x^2}{2!} f''(x) + \dots = \sum_{n=0}^{\infty} \frac{\Delta x^n}{n!} f^{(n)}(x), \quad (4.34)$$

whereas the negative distances are named as the backward difference:

$$f(x - \Delta x) = f(x) - \frac{\Delta x}{1!} f'(x) + \frac{\Delta x^2}{2!} f''(x) - \dots \quad (4.35)$$

The first derivation $f'(x)$ is obtained by solving Eq. (4.34) for $f'(x)$:

$$f'(x) = \frac{f(x + \Delta x) - f(x)}{\Delta x} - \frac{\Delta x}{2!} f''(x) - \dots \quad (4.36)$$

For small mesh sizes, especially for $\Delta x < 1$, the first sum of Eq. (4.36) dominates the remainder of the equation. Taking only the first part of the equation for the calculation of the first derivative, the remainder becomes the calculation error O and the Eq. (4.36) is shortened to [72] [73]:

$$f'(x) = \frac{f(x + \Delta x) - f(x)}{\Delta x} + O(\Delta x). \quad (4.37)$$

The backward difference is received by solving Eq. (4.35) for $f'(x)$:

$$f'(x) = \frac{f(x) - f(x - \Delta x)}{\Delta x} + O(\Delta x). \quad (4.38)$$

The central difference of the first derivation is obtained by finding the difference of Eq. (4.34) and Eq. (4.35) and subsequently solving for $f'(x)$:

$$f'(x) = \frac{f(x + \Delta x) - f(x - \Delta x)}{2\Delta x} + O(\Delta x^2). \quad (4.39)$$

The second order of central difference is obtained by an addition of Eq. (4.34) and Eq. (4.35) and subsequently solving for $f''(x)$:

$$f''(x) = \frac{f(x + \Delta x) - 2f(x) + f(x - \Delta x)}{\Delta x^2} + O(\Delta x^2). \quad (4.40)$$

For computational calculations and in the following equations, the calculation error O is neglected. A discretization of the 1D problem into equidistant parts having the size Δx leads to:

$$x_i = x_0 + i \cdot \Delta x \quad \text{for} \quad i = 1, \dots, N + 1, \quad (4.41)$$

assuming x_0 to be the starting point and x_{N+1} to be the ending point of the lattice (see Fig. 4.3). Every discrete position x_i is approximated by T_i , whereby the real value is given by $T(x_i)$:

$$T_i \approx T(x_i) \quad \text{for} \quad i = 1, \dots, N. \quad (4.42)$$

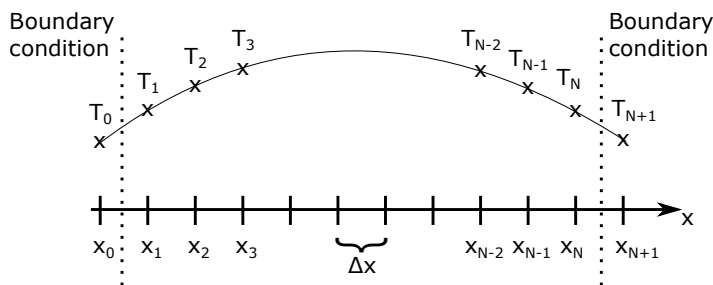


Figure 4.3: Discretization of a continuous function fixed by its boundary conditions.

The central difference of Eq. (4.40) leads to an expression to approximate each grid point x_i of the desired differential equation (4.31):

$$0 = a \frac{T_{i-1} - 2T_i + T_{i+1}}{\Delta x^2} + s_i \cdot T_i \quad \text{for} \quad i = 1, \dots, N \quad \text{and} \quad s_i = s(x_i). \quad (4.43)$$

With $b = \frac{a}{\Delta x^2}$:

$$0 = bT_{i-1} - 2bT_i + bT_{i+1} + s_i \cdot T_i \quad \text{for} \quad i = 1, \dots, N \quad \text{and} \quad s_i = s(x_i). \quad (4.44)$$

As one can see, the first point T_1 in lattice does not have a preceding grid point T_0 and the last grid point T_N does not have a following element T_{N+1} . These values are given by the Dirichlet boundary conditions. Eq. (4.44) can be represented for each element of the discrete lattice in a

system of linear equations by incorporating the boundary conditions:

$$\begin{bmatrix} 2b + s_1 & -b & 0 & \cdots & 0 \\ -b & 2b + s_2 & -b & \ddots & 0 \\ \vdots & \ddots & \ddots & \ddots & \vdots \\ 0 & \ddots & -b & 2b + s_{N-1} & -b \\ 0 & \cdots & 0 & -b & 2b + s_N \end{bmatrix} \cdot \begin{bmatrix} T_1 \\ T_2 \\ \vdots \\ T_{N-1} \\ T_N \end{bmatrix} = \begin{bmatrix} bT_0 \\ 0 \\ \vdots \\ 0 \\ bT_{N+1} \end{bmatrix}. \quad (4.45)$$

4.2.2 Effective Mass Hamiltonian

The operator describing the particle energy in space is given by the Hamiltonian. It expresses the total particle energy by the kinetic and potential energy $E = E_{kin} + E_{pot}$, which is given for the classical case by:

$$H = \frac{p^2}{2m} + E_{pot}. \quad (4.46)$$

whereby p is given in the quantum case by an operator $\hat{p} = -i\hbar \frac{\partial}{\partial r}$ which results in the quantum mechanical Hamiltonian:

$$H = -\left(\frac{\hbar^2}{2m}\right) \nabla^2 + E_{pot}. \quad (4.47)$$

The longitudinal part, which is needed for the 1D description in real space, is given by:

$$H_L = E_c - \frac{\hbar^2 d^2}{2mdx^2} + U(x), \quad (4.48)$$

with $U(x)$ is the 1D energy profile and E_c is the energy of the bottom of the conduction band. By applying Schrödinger's wave equation:

$$\mathbf{H}_L \psi = E\psi, \quad (4.49)$$

the finite difference approximation is applied to perform second derivative of Schrödinger's equation. The method describes the wavefunction of each element with the help of its former and following element by applying a lattice in real space. The first element of the device is given by:

$$E\psi_1 = -t\psi_0 + (E_c + 2t + U(1))\psi_1 - t\psi_2 \quad (4.50)$$

and the last element of the device is given by:

$$E\psi_N = -t\psi_{N-1} + (E_c + 2t + U(N))\psi_N - t\psi_{N+1}, \quad (4.51)$$

with $t = \hbar^2/(2ma^2)$ and a is the finite grid size. In order to describe each cell of a discrete lattice by its former and following element as is done in Eq. (4.50) and Eq. (4.51), the tridiagonal Hamiltonian matrix \mathbf{H}_L is given by $E_c + 2t + U(x)$ on the diagonal and $-t$ on the upper and

lower diagonals:

$$\mathbf{H}_L = \begin{bmatrix} E_c + 2t + U(1) & -t & 0 & \cdots & 0 \\ -t & E_c + 2t + U(2) & -t & \cdots & 0 \\ 0 & -t & E_c + 2t + U(3) & \cdots & 0 \\ \vdots & \ddots & \ddots & \ddots & \vdots \\ 0 & \cdots & 0 & -t & E_c + 2t + U(N) \end{bmatrix}. \quad (4.52)$$

In Eq. (4.50) one can see that the element ψ_0 is not well described because it is located outside of the device. The same is valid for the element ψ_{N+1} of Eq. (4.51).

4.2.3 Infinite Wall Boundary Conditions

The infinite wall boundary conditions assume a potential well and force the wavefunction to equal zero at both ends and therefore both elements are set to zero $\psi_{N+1} = 0, \psi_0 = 0$. Applying the boundary conditions to Eq. (4.49), the matrix form is given by:

$$\begin{bmatrix} \ddots & & \ddots & 0 \\ -t & E_c + 2t + U(x) & -t & \\ 0 & & \ddots & \ddots \end{bmatrix} \cdot \begin{bmatrix} \psi_1 \\ \vdots \\ \psi_N \end{bmatrix} = E \begin{bmatrix} \psi_1 \\ \vdots \\ \psi_N \end{bmatrix}, \quad (4.53)$$

thereby the equation can be rewritten as:

$$(\mathbf{E}\mathbf{I} - \mathbf{H}_L)\psi = 0, \quad (4.54)$$

whereby \mathbf{I} being the identity matrix to map the energy on the diagonal of a matrix with the same size as \mathbf{H}_L . The eigenvalues of \mathbf{H}_L are the allowed energy levels ε_n and the corresponding eigenfunctions are the wavefunctions ψ_n . The case of infinite boundary conditions as shown in Fig. 4.4 assume a potential well and is therefore not practicable when considering a transistor in transport direction. For the case of a transistor, the boundary conditions are improved by applying open boundary conditions.

4.2.4 Open Boundary Conditions

When considering a transistor, the well is flipped into a barrier. Secondly, due to the connection of the device with the contacts, the system is not more confined by the infinite boundary conditions which force the wavefunction to be zero $\psi_0 = 0 \rightarrow \psi_0 \neq 0, \psi_{N+1} = 0 \rightarrow \psi_{N+1} \neq 0$. For the case that the contacts are heavily doped, infinite long and stay in equilibrium, the wavefunction inside the contact is assumed by plane waves. These plane waves keep the mathematics simple because they describe the simplest possible connection of the device to the outside world. As shown in Figure 4.5(a), the wave of the source contact $1e^{ik_1x}$ enters the device at the left side. Some part of the incident wave is reflected $r'e^{-ik_1x}$ by the potential barrier

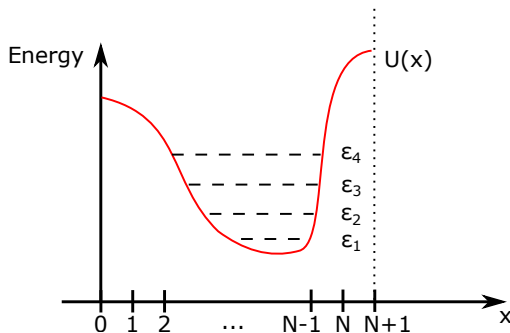


Figure 4.4: Discretized potential well showing the discrete eigenenergies [63].

and turns back to the source contact. Inside the source contact scattering turns everything into equilibrium. Some part of the wave transmits $t'e^{ik_2x}$ through the device and enters the drain contact. Inside the contact, the wave is also restored to equilibrium. As shown in Figure 4.5(b), another incident wave enters the device coming from the drain contact. Again, some part is reflected and transmits through the device. Due to these incoming waves, the wavefunction at both ends needs to be described by appropriate boundary conditions and not by zero. To find appropriate boundary conditions, in the following the wavefunction is solved inside the contacts. Both contacts are assumed to be infinite long and having a constant energy profile. The solution to this case is given by plane waves. The wavefunction inside the source contact at an arbitrary position x is given by:

$$\psi(x) = 1e^{ik_1x} + r'e^{-ik_1x}. \quad (4.55)$$

In order to give an appropriate open boundary condition by using the finite difference discretization at the first element, Eq. (4.50) can be rewritten as:

$$E\psi_1 - [-t\psi_0 + (2t + Ec_1)\psi_1 - t\psi_2] = 0. \quad (4.56)$$

The wavefunction at the position ψ_0 has to be figured out, which is the first element inside the contact having the position $x = -a$ (see Fig. 4.6):

$$\psi(x = -a) = \psi_0 = 1e^{-ik_1a} + r'e^{ik_1a}. \quad (4.57)$$

At the first node inside the device having the position $x = 0$, the wavefunction ψ_1 is given by:

$$\psi(x = 0) = \psi_1 = 1 + r'. \quad (4.58)$$

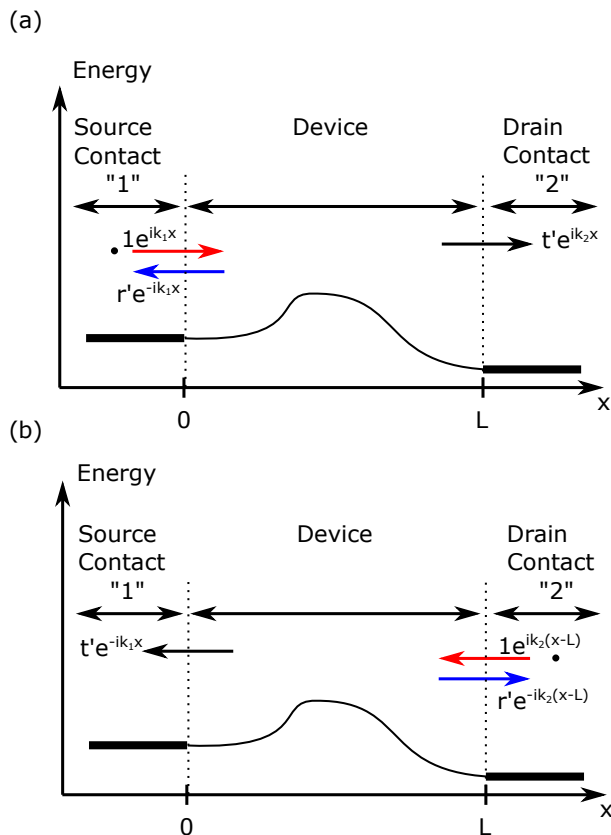


Figure 4.5: Incident wave coming from (a) the source contact and (b) the drain contact. Some part is reflected by the potential barrier and some part transmits through the device [63].

Solving Eq. (4.58) for r' and substituting into Eq. (4.57), the wavefunction inside the contact is expressed by using the wavefunction of the device:

$$\psi_0 = \psi_1 e^{ik_1 a} - (e^{ik_1 a} - e^{-ik_1 a}). \quad (4.59)$$

Substituting this result into Eq. (4.56) leads to the expression for the first element:

$$E\psi_1 - [-t \cdot (\psi_1 e^{ik_1 a} - (e^{ik_1 a} - e^{-ik_1 a})) + (2t + E c_1)\psi_1 - t\psi_2] = 0. \quad (4.60)$$

Eq. (4.59) and (Eq. 4.60) lead to the following two results in order to account for open boundary conditions, $-te^{ik_1 a}$ needs to be added to the first diagonal element of the matrix \mathbf{H}_L and $t(e^{ik_1 a} - e^{-ik_1 a})$ needs to be added to the total wave equation. Doing the same calculations for the second contact, equally conditions can be obtained. The former obtained expression for

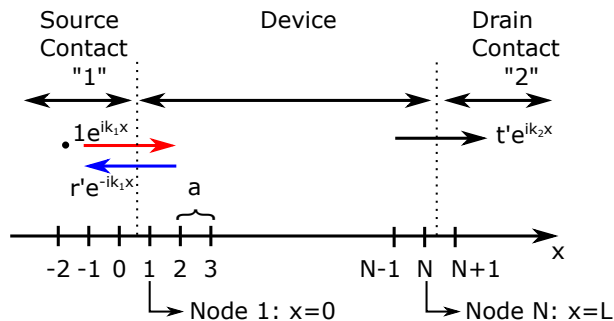


Figure 4.6: Wavefunction inside the source contact [63].

the source contact $-te^{ik_1a}$ is added to the first cell of $\mathbf{H}_L(1,1)$ and $-te^{ik_2a}$ is added to the last element $\mathbf{H}_L(N,N)$. This summation is done by the self-energy function of the first contact Σ_1 and second contact Σ_2 which are given by:

$$\Sigma_1 = \begin{bmatrix} -te^{ik_1a} & 0 & \dots & 0 \\ 0 & 0 & \dots & 0 \\ \vdots & \vdots & \ddots & \vdots \\ 0 & 0 & \dots & 0 \end{bmatrix}, \quad \Sigma_2 = \begin{bmatrix} 0 & \dots & 0 & 0 \\ \vdots & \ddots & \vdots & \vdots \\ 0 & \dots & 0 & 0 \\ 0 & \dots & 0 & -te^{ik_2a} \end{bmatrix}. \quad (4.61)$$

The second result obtained from Eq. (4.60) is captured by the broadening functions:

$$\Gamma_1 = i \left[\Sigma_1 - \Sigma_1^* \right], \quad (4.62)$$

$$\Gamma_2 = i \left[\Sigma_2 - \Sigma_2^* \right]. \quad (4.63)$$

By applying the former results, the Schrödinger equation is enhanced by:

$$\mathbf{E}\psi = [\mathbf{H}_L + \Sigma]\psi + \mathbf{S} = i\gamma, \quad (4.64)$$

whereby γ of Eq. (4.64) is one element of the $\Gamma_{1,2}$ matrix. In the case of the first contact this column vector is expressed by $\gamma_1 = [-[\Sigma_1(1,1) - \Sigma_1^*(1,1)], 0, \dots, 0]^T$. Due to the broadening of the former sharp energy levels, as shown in Figure 4.7, to a continuous density of states, the energy is treated as a variable. The response of the device to incoming electrons has to be calculated at a range of energies and not only at the former discrete energy levels.

4.2.5 Dispersion Relation

By incorporating the self-energy functions for treating the open boundary conditions and additionally the broadening which inevitably comes together with the connection of the device

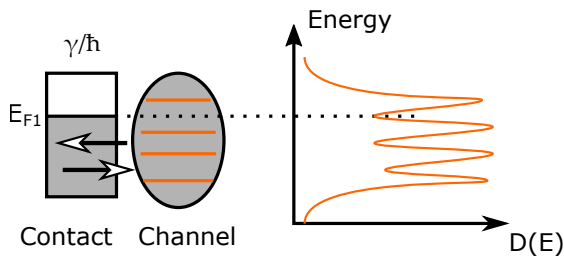


Figure 4.7: Due to the connection of the device with the channel, the former discrete energy levels are broadened into a continuous density of states [37].

with the contacts, the wavefunction is given by:

$$[EI - \mathbf{H}_L - \Sigma_1 - \Sigma_2] \psi = S = i\gamma. \quad (4.65)$$

As derived by Eq. (4.61), Σ_1 and Σ_2 depend on $k_1 a$ and $k_2 a$ which are given by the dispersion relation. Since the self-energies describe the wave coming in from the contact, the dispersion relation is also given inside the contact. Due to the finite difference discretization inside the contact which is assumed to be an infinitely long and also a uniform structure with a constant conduction band, the dispersion relation inside the contact is shown in Fig. 4.8 and calculated by [37]:

$$E = E_c + U(1) + 2t(1 - \cos(k_1 a)), \quad (4.66)$$

whereby E is the considered energy and E_c is the bottom of the conduction band. As one can see in Fig. 4.8, this approximation is only valid for energies $E \ll 4t$. Consequently, the

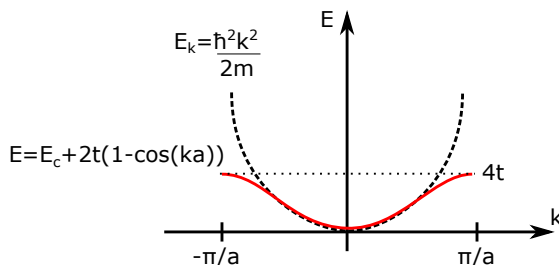


Figure 4.8: Dispersion relation assumed by the effective mass equation (dashed line) and the assumed dispersion relation due to the finite difference discretization inside the contact (solid line) [63].

self-energy functions Σ_1 , Σ_2 as well as the broadening functions Γ_1 , Γ_2 are energy dependent and change their values in k -space [37].

4.2.6 Retarded Green's Function

The device's system response to an input stimulus is given by the retarded Green's function \mathbf{G} . The Green's function is built out of a matrix subtraction of the considered energy E , the Hamiltonian matrix \mathbf{H}_L and the self-energy functions of each contact $\mathbf{\Sigma}_1$ and $\mathbf{\Sigma}_2$:

$$\mathbf{G}(E) = \left[\mathbf{E}I - \mathbf{H}_L - \mathbf{\Sigma}_1 - \mathbf{\Sigma}_2 \right]^{-1}. \quad (4.67)$$

The retarded Green's function shown in Eq. (4.67) can now be presented in matrix form by:

$$\mathbf{G}(E) = \left[\begin{bmatrix} E & 0 & \dots & 0 \\ 0 & E & \dots & 0 \\ \vdots & \vdots & \ddots & \vdots \\ 0 & 0 & \dots & E \end{bmatrix} - \begin{bmatrix} E_c + 2t + U(1) & -t & 0 & \dots & 0 \\ -t & E_c + 2t + U(2) & -t & \dots & 0 \\ \vdots & \vdots & \ddots & \ddots & \vdots \\ 0 & \dots & \dots & 0 & -t & E_c + 2t + U(N) \end{bmatrix} - \begin{bmatrix} -t \exp(ik_1 a) & 0 & \dots & 0 \\ 0 & 0 & \dots & 0 \\ \vdots & \vdots & \ddots & \vdots \\ 0 & 0 & \dots & 0 \end{bmatrix} - \begin{bmatrix} 0 & 0 & \dots & 0 \\ 0 & 0 & \dots & 0 \\ \vdots & \vdots & \ddots & \vdots \\ 0 & 0 & \dots & -t \exp(ik_1 a) \end{bmatrix} \right]^{-1}. \quad (4.68)$$

The wavefunction can be expressed by:

$$\psi = \mathbf{G} \cdot \mathbf{S} = \mathbf{G} \cdot i\gamma. \quad (4.69)$$

4.2.7 Electron Density

In the following, the aim is to calculate the electron density inside the device. As well known, the electron density is related to the square of the wavefunction, whereby the connection between them needs to be derived.

The wavefunction for an infinite bulk semiconductor is given by plane waves. When considering a part of the semiconductor having the length L and applying again periodic boundary conditions one can add up all k -states initiated by the periodic boundary conditions. Filling up these states by the Fermi function will give the electron density [37] [63]:

$$n(x) = \sum_k |\psi_k(x)|^2 \cdot F(E - E_F), \quad (4.70)$$

with the wavefunction inside the contact is given by:

$$\psi_k(x) = \frac{1}{\sqrt{L}} e^{ikx}. \quad (4.71)$$

Since $|e^{ikx}|^2 = \text{const}$ for a plane wave solution, the sum is given by:

$$n(x) = \frac{1}{L} \sum_k F(E - E_F). \quad (4.72)$$

Similar to the example above, one can also calculate the electron density inside a device. In a first step the device is connected to only one of the two contacts (see Fig. 4.5(a)). A plane wave coming from the contact penetrates into the device and results in a wavefunction within the device described by Eq. (4.65). As it was made for the bulk semiconductor, the wavefunction has to be weighted by the Fermi function. Since the wavefunction comes from the left contact, the Fermi function of the left contact E_{F1} is applied:

$$n_1(x) = \frac{1}{L} \sum_{k_1} |\psi_{k_1}(x)|^2 \cdot F(E - E_{F1}). \quad (4.73)$$

For a bulk semiconductor with discretized k -states, the number of states is given by $dk/2\pi \cdot L \cdot 2$. The multiplication by 2 is made to give justice to the up and down spin. The sum over k -space can be converted into an integral over k -space, which can be converted into an integral over energy:

$$n_1(x) = \frac{1}{L} \cdot \frac{L}{2\pi} \cdot 2 \int_0^\infty dE \frac{dk_1}{dE} |\psi_{k_1}(x)|^2 \cdot F(E - E_{F1}). \quad (4.74)$$

The local density of states $LDOS$ initiated from the source contact depending on the position and the energy is given by:

$$LDOS_1(x, E) = \frac{1}{\pi} \cdot \frac{dk_1}{dE} |\psi_{k_1}(x)|^2. \quad (4.75)$$

The same consideration can be applied to the second contact leading to the states initiated from the second contact. $LDOS_2(x, E)$. Both contacts contribute together to the total electron density inside the device:

$$n(x) = \int_0^\infty LDOS_1(x, E) \cdot F(E - E_{F1}) dE + \int_0^\infty LDOS_2(x, E) \cdot F(E - E_{F2}) dE. \quad (4.76)$$

Since ψ is given in terms of the retarded Green's function which is a $N \cdot N$ matrix (see Eq. (4.68)) the calculation is done by:

$$\psi \psi^H = (\mathbf{G} \gamma_1) (\gamma_1^H \mathbf{G}^H), \quad (4.77)$$

with H is the hermitian transpose and $\psi \cdot \psi$ is calculated at each node [63]:

$$\psi\psi^H = \begin{bmatrix} \psi_1 \cdot \psi_1 & \psi_1 \cdot \psi_2 & \psi_1 \cdot \psi_3 & \cdots & \\ \psi_2 \cdot \psi_1 & \psi_2 \cdot \psi_2 & \psi_2 \cdot \psi_3 & \cdots & \\ \cdots & \cdots & \psi_3 \cdot \psi_3 & \cdots & \\ & & & \ddots & \\ & & & & \psi_N \cdot \psi_N \end{bmatrix}. \quad (4.78)$$

The diagonal elements of this matrix are needed to calculate the electron density at each x -position as shown in Eq. (4.74). By performing this, the $N \cdot N$ sized electron density matrix initiated by the left contact is obtained from [37] [63]:

$$\rho_1 = \frac{1}{\pi} \cdot \int_0^{\infty} \frac{dk_1}{dE} \{ \mathbf{G} \gamma_1 \gamma_1^H \mathbf{G}^H \} \cdot F(E - E_{F1}) dE. \quad (4.79)$$

The diagonal elements of ρ_1 contain the electron density at each node. By using the dispersion relation:

$$E(k) = 2t(1 - \cos(ka)), \quad (4.80)$$

the inverse of the derivative can be built:

$$\frac{dk}{dE} = \frac{1}{2at \cdot \sin(ka)} \quad (4.81)$$

and $\gamma_1 \gamma_1^H$ is given by:

$$\gamma_1 \gamma_1^H = \begin{bmatrix} 4t^2 \sin^2(ka) & 0 & \cdots & 0 \\ 0 & 0 & \cdots & 0 \\ \vdots & \vdots & \ddots & \\ 0 & 0 & & 0 \end{bmatrix}. \quad (4.82)$$

By substituting both former equations into Eq. (4.79), $t \cdot \sin(ka)$ can be canceled with one of those given in Eq. (4.82):

$$\frac{a}{\pi} \frac{dk}{dE} \gamma_1 \gamma_1^H = \mathbf{F}_1 = \begin{bmatrix} 2t \sin(ka) & 0 & \cdots & 0 \\ 0 & 0 & \cdots & 0 \\ \vdots & \vdots & \ddots & \\ 0 & 0 & & 0 \end{bmatrix} = i(\boldsymbol{\Sigma}_1 - \boldsymbol{\Sigma}_1^H). \quad (4.83)$$

Substituting Eq.(4.83) into Eq. (4.79), the equation can be modified to:

$$\rho_1 = \int_0^{\infty} 2 \cdot \frac{\mathbf{A}_1}{2\pi} \cdot F(E - E_{F1}) dE, \quad (4.84)$$

with \mathbf{A}_1 is the spectral function of the first contact:

$$\mathbf{A}_1 = \mathbf{G}\mathbf{\Gamma}_1\mathbf{G}^H. \quad (4.85)$$

Each spectral function could be seen as the available density of states of each contact. By doing this for both contacts, the total electron density of the device is given by:

$$\rho = \rho_1 + \rho_2. \quad (4.86)$$

4.2.8 Numerical Treatment of Scattering

Up to now, the focus was on a purely ballistic transport. A ballistic transport does not depend on the device length and consequently does not lead to Ohm's law. The NEGF approach assumes a third contact Σ_s to incorporate scattering processes inside the device (see Fig. 4.9):

$$\mathbf{G}(E) = \left[\mathbf{E}\mathbf{I} - \mathbf{H}_L - \Sigma_1 - \Sigma_2 - \Sigma_s \right]^{-1}. \quad (4.87)$$

The assumption of this s -contact was first made by Büttiker in the mid 1980s [74]. The contact extracts and reinjects electrons throughout the channel to describe the incoherent scattering processes. As it was shown for the source and drain contacts $\Sigma_{1,2}$, the strength of the coupling is again described by the broadening $\mathbf{\Gamma}_s$. In contrast to the other contacts, the s -contact does not have a Fermi function. Therefore, the outflow of electrons is again given by $\text{Trace}[\mathbf{\Gamma}_s\mathbf{G}^n/2\pi]$ but the inflow needs to be calculated in another way. Where the relation between electron

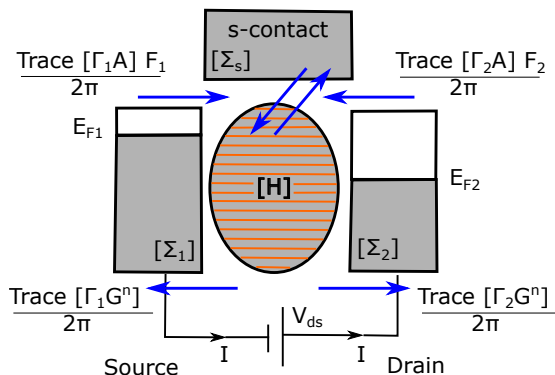


Figure 4.9: Multi-level device showing the source and drain contact and the hereby introduced s -contact and the correlation function \mathbf{G}^n in order to incorporate scattering processes [37].

density and potential is given by the law of electrostatic, the dependency between Σ_s and density matrix ρ can be much more difficult. Therefore, Σ_s has to be calculated self-consistently together with the density matrix ρ [42]. The additional effort dramatically slows down the simulation time and forbids its use for a compact model.

CHAPTER 5

Potential Model

This chapter introduces the 2D potential model for the compact model of an ultra-short DG MOSFET down to a minimum channel length of $l_{ch} = 6$ nm in a detailed way. The potential model refers to the mathematical basics introduced in Sec. 4. Since the industrial transistor scaling not only affects the channel length but also the channel thickness, the potential model has to be accurate down to a minimum thickness of $t_{ch} = 2$ nm. In this case neither a gate underlap nor a gate overlap is considered, thus the channel length of the model equals the top and bottom gate length l_{ch} . The source and drain regions are highly n-doped typical $N_{sd} = 2 \cdot 10^{20} \text{cm}^{-3}$ with a length of $l_{sd} = 10$ nm. The thickness of the intrinsic channel is presented by t_{ch} , whereby the thickness of the insulator is given by t_{in} .

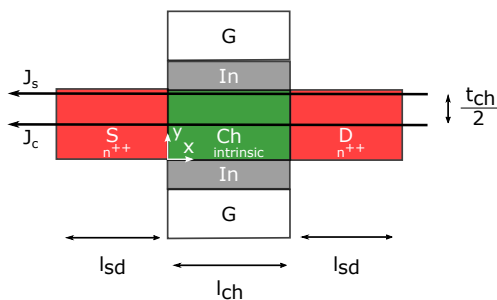


Figure 5.1: Cross-section of the considered ultra-short DG MOSFET. Shown are both gates G , the insulator In , the intrinsic channel Ch , the constant doping profiles of the source S and drain region D . J_s and J_c show the position dependent slices for the 1D current calculation at the channel surface and center.

In a first step some preliminaries of the potential model are introduced in Sec. 5.1. In Sec. 5.2 the potential solution is derived for the channel region. In order to describe the potential within the source and drain region, a closed-form expression is given in Sec. 5.3. From the potential for the entire device, the band structure is derived in Sec. 5.4. Based on the potential model for the MOSFET device, the potential model for the TFET is derived in Sec. 5.5. In

Sec. 5.6 the accuracy of the potential model for the DG MOSFET is verified by comparison with numerical 2D TCAD simulation data for the device structure shown in Fig. 5.1. Finally in Sec. 5.7, the potential model verification for the DG TFET is shown.

5.1 Modeling Preliminaries

Before the potential calculation can be started, some preliminaries have to be considered at first. These show some simplifications in Sec. 5.1.1 which are needed to obtain a closed-form expression of the potential. In Sec. 5.1.2 the former introduced conformal mapping technique is applied to the DG device structure. Since the focus is on the Laplace equation where mobile channel charges are neglected, the inversion charges are calculated as a second order effect in a closed-form in Sec. 5.1.3. Since the channel thickness is smaller than 10 nm, quantum effects play an important role and are considered in Sec. 5.1.4.

5.1.1 Model Simplifications

Many physical, electrical and also quantum-mechanical effects influence the behavior of ultra-short channel transistors. In the first step, these effects are neglected to achieve a general and stable model for a closed-form potential solution. Due to the electrical resistances of the source and drain region, the device current is limited, but this effect is neglected at first. This effect mainly influences the device behavior at high drain currents and is not treated by the model.

Laplace's Equation

Solving Poisson's equation seems to be the accurate way, but its numerical solution forbids the usage for compact models. Due to the fact, that the DG MOSFET is built out of an intrinsic channel, the charges within the channel are neglected in the first step. Thus, it is much more suitable to consider the Laplace equation, which is a special case of Poisson's equation. This case requires to look at the device in the subthreshold region, where the inversion charges as well as the channel doping may be neglected:

$$\Delta\Phi(x,y) = -\frac{\rho}{\varepsilon_{si}} \quad \rightarrow \quad \Delta\Phi(x,y) \approx 0, \quad (5.1)$$

with ε_{si} is the silicon's permittivity and ρ the space charge inside the channel region. Considering a device just in the subthreshold region is not sufficient, thus the on-state has to be incorporated in another way which is shown in Sec. 5.1.3.

Scaled Insulator

The conformal mapping technique is one method to solve the Laplace equation and requires to map the geometry and all associated boundary conditions. The device contains two different permittivities, one for the insulator material ε_{in} and the other for the channel material ε_{si} . The potential solution requires a constant permittivity throughout the device because these two magnitudes lead to different electric fields E_0 and hence cause discontinuities in the potential calculation. To avoid this problem $\varepsilon_{si} \neq \varepsilon_{in}$, one of them needs to be adjusted and therefore the permittivity of the insulator is adapted by a scaled insulator thickness \tilde{t}_{in} [75]:

$$D_{in} = \varepsilon_0 \varepsilon_{si} \cdot E_0 = \varepsilon_0 \varepsilon_{in} \cdot E_{in} = \varepsilon_0 \varepsilon_{in} \frac{V_{in}}{t_{in}}, \quad (5.2)$$

with V_{in} is the potential difference between both insulator surfaces and D_{in} is the electric displacement field. t_{in} is the insulator thickness. To avoid discontinuities Eq. (5.2) is modified by the scaled insulator thickness \tilde{t}_{in} :

$$\tilde{t}_{in} = \frac{\varepsilon_{si}}{\varepsilon_{in}} \cdot t_{in}, \quad (5.3)$$

$$D_{in} = \varepsilon_0 \varepsilon_{si} \cdot E_0 = \varepsilon_0 \varepsilon_{si} \frac{V_{in}}{\tilde{t}_{in}}. \quad (5.4)$$

It should be noted that the applied theory of using scaled insulator thickness is only suitable for channel length much bigger than the insulator thickness $l_{ch} \gg t_{in}$ [75]. For the case of $\varepsilon_{in} > \varepsilon_{si}$ the approach changes the device structure from the original one shown in Fig. 5.2(a) to the new one shown in Fig. 5.2(b).

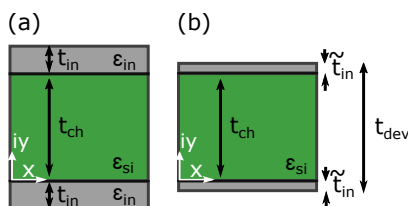


Figure 5.2: (a) Device with insulator thickness t_{in} and two distinct ε for the channel region ε_{si} and insulator ε_{in} . (b) Device with scaled insulator thickness \tilde{t}_{in} and only one permittivity ε_{si} .

Decomposition of the Device

The channel and insulator electrostatics are given in a 4-corner rectangular area surrounded by the boundary conditions. As shown in previous work [53], the region can easily be decomposed into two 2-corner structures. These separate 2-corner structures yield less complexity while solving the Laplace equation. The source related case describes the potential behavior at the source side of the channel, whereas the drain related case describes the potential behavior at the

drain side of the channel. Since the potential at the channel junctions consists of a mixture of constant and parabolically shaped potentials (see Fig. 5.3(a)), both cases are further separated into constant and parabolically shaped boundary conditions. These resulting four cases are the source related case with constant boundary conditions (see Fig. 5.3(b)), source related case with parabolic boundary conditions (see Fig. 5.3(c)), drain related case with constant boundary conditions (see Fig. 5.3(d)) and drain related case with parabolic boundary conditions (see Fig. 5.3(e)).

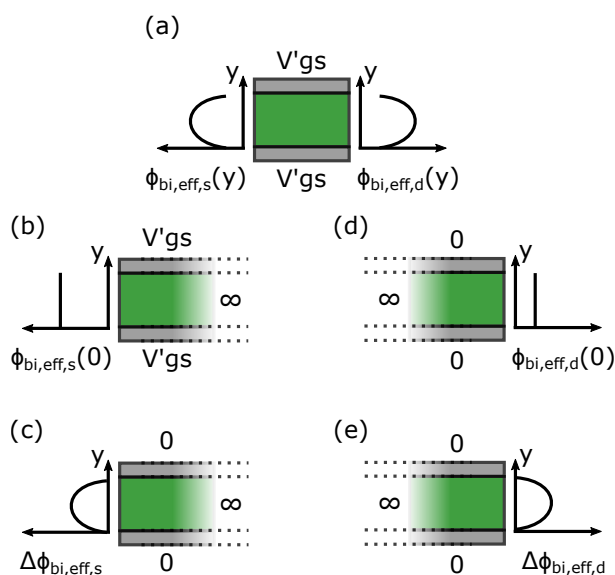


Figure 5.3: Decomposition of the DG MOSFET to obtain four separate boundary conditions. (a) Boundary conditions of the whole device with a mixture of constant and parabolically shaped potentials at the channel junctions. (b) source- (d) drain-related case with constant boundary conditions for the 2D Laplace solution. (c) source- (e) drain-related case with parabolically shaped boundary conditions at the channel junctions for the 2D Laplace solution.

5.1.2 Conformal Mapping of the Device Structure

A specific part of the potential model is the applied conformal mapping technique. The general formalism for mapping a polygon has been explained detailed in Sec. 4.1.3. In the following the mapping technique is applied for the source related case. The drain case is done in the same way by mirroring the mapping function of the source related case and replacing the boundary conditions. The Schwarz-Christoffel transformation maps the 2-corner structure from the z -plane into the upper half of the w -plane. The boundaries are mapped from a 2D distribution within z -plane on the real u -axis within w -plane. The angles to map the vertexes depend on the device structure shown in Fig. 5.4 and are listed in Table 5.1. Inserting the

\bar{u}	$w_{\bar{u}}$	$z_{\bar{u}}$	$\pi\gamma_{\bar{u}}$	$\gamma_{\bar{u}}$
1'	$+\infty$	$+\infty$	$+\pi$	$+1$
2	$+1$	z_2	$+\frac{\pi}{2}$	$+\frac{1}{2}$
5	-1	z_5	$+\frac{\pi}{2}$	$+\frac{1}{2}$
1''	$-\infty$	$+\infty$	$+\pi$	$+1$

Table 5.1: Mapping of channel positions from z -plane into w -plane. With $\gamma_{\bar{u}}$ as the angle of mapping. The other positions i.e. \bar{u}_3 and \bar{u}_4 already have an angle of $1 \cdot \pi$ which does not need to be changed.

values of Table 5.1 into Eq. (4.22), the specific differential is given by:

$$\frac{dz(w)}{dw} = \frac{C}{\sqrt{w-1}\sqrt{w+1}}. \quad (5.5)$$

The integration finally leads to:

$$z(w) = 2C \ln(\sqrt{w-1} + \sqrt{w+1}) + D. \quad (5.6)$$

The constant D is assumed to be zero, because the absolute position within the original plane is not important. By applying Eq. (4.25), the constant C is calculated as:

$$z_1'' - z_1' = i t_{dev} = i \pi C \rightarrow C = \frac{t_{dev}}{\pi}, \quad (5.7)$$

with t_{dev} is shown in Fig. 5.3 and calculated using the device geometry:

$$t_{dev} = 2\tilde{t}_{in} + t_{ch}. \quad (5.8)$$

Together with the calculated parameters, the inverse function of Eq. (5.6) is built, which maps all points from the z -plane into the w -plane:

$$w(z) = f^{-1}(z(w)) = u + iv = \cosh\left(\frac{\pi z}{t_{dev}}\right) = \cosh\left(\frac{\pi(x + iy)}{t_{dev}}\right). \quad (5.9)$$

5.1.3 Inversion Charges

Up till now the focus has been on the subthreshold region, where charges inside the channel are neglected. In order to extend the model to above threshold operation, these charges have to be considered. Since the Laplace equation is only valid for a charge free space, the influence of the inversion charges on the electrostatics is calculated as a second order effect. The inversion

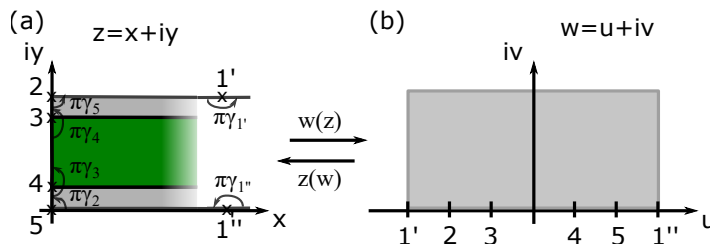


Figure 5.4: Mapping the source related case of the device structure from z -plane shown in (a) into w -plane in (b) and vice versa.

charge density per gate area $Q'_{i,s}$ is estimated in a closed-form approach obtained from [54]:

$$Q'_{i,s} = 2C'_{in} V_{th} \cdot \mathcal{L} \left\{ \frac{Q'_{i,0}}{2C'_{in} V_{th}} \cdot \exp \left(\frac{2C'_{in}(V_{gs} - V_0) + Q'_{i,0}}{2C'_{in} V_{th}} \right) \right\}. \quad (5.10)$$

The mobile electron charge density $Q'_{i,0}$ is given at an arbitrary gate bias $V_{gs} = V_0$, which for the adjustment of this model is set to the flatband voltage $V_0 = V_{fb}$:

$$Q'_{i,0} = q \cdot n_i \cdot t_{ch}, \quad (5.11)$$

with n_i is the intrinsic carrier concentration and t_{ch} is the channel thickness. In Eq. (5.10), \mathcal{L} is the first branch of Lambert's W -function, V_{th} is the thermal voltage and C'_{in} is the insulator capacitance per gate area. The device current of nano-scaled transistors is mostly controlled by the energy barrier in the channel region [76], whereas electrons located at the drain side of the barrier are absorbed anyway. This implies that the influence of the mobile charges located at the energy barrier on the electrostatic is the largest. The model implementation assumes a constant charge density along the channel to calculate the resulting inversion layer $\frac{Q'_{i,s}}{2}$ at the channel surface. If one considers a purely ballistic transport, this assumption is suitable because the mobile charges are not able to change their energy. Therefore, the mobile charge density is constant at each x -position, when neglecting back scattering [42]. The part of the gate voltage ΔV_{gs} shielded by the inversion charges, needs to be subtracted from the contact gate voltage V_{gs} and is calculated by:

$$\Delta V_{gs} = \left(\frac{Q'_{i,s}}{2 \cdot C'_{in}} \right). \quad (5.12)$$

This reduced effective gate voltage V'_{gs} influences the channel potential:

$$V'_{gs} = V_{gs} - \Delta V_{gs}. \quad (5.13)$$

Below threshold the effective gate voltage almost equals the contacting gate voltage $V'_{gs} \approx V_{gs}$, but with linearly increasing gate voltage above threshold the barrier height and hence V'_{gs} remains almost constant. Figure 5.5 shows the correlation of these three voltages for different contacting gate voltages. The potential model consequently applies this effective gate bias V'_{gs} as a boundary condition for the gate contact.

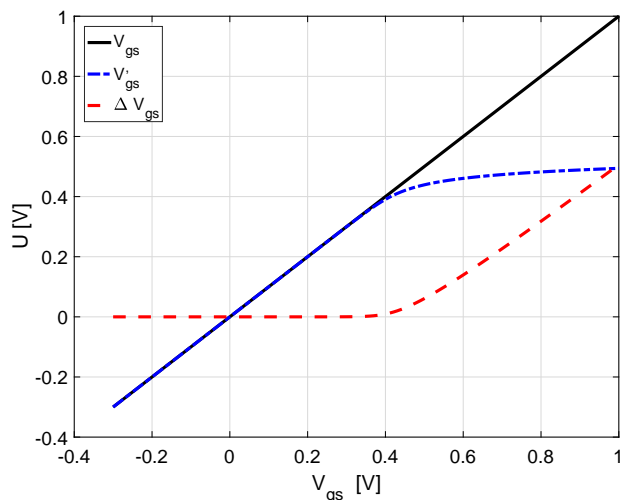


Figure 5.5: Comparison of contacting gate voltage V_{gs} , the shielded part of the gate voltage ΔV_{gs} and the reduced gate voltage V'_{gs} applied for the Laplace equation.

5.1.4 Quantum Confinement

Quantum confinement heavily influences the device behavior of nano-scaled transistors with a channel thickness lower than approximately 5 nm. This quantum mechanical effect changes the device behavior and consequently some compact models capture this effect as a change of the threshold voltage [77] or an adaption of the flatband voltage [78]. For this model, the effect of quantum confinement is considered by an adaption of the flatband voltage. Therefore, the confinement energy ΔE is added to the physical value of the flatband voltage:

$$V_{fb} = V_{fb,phy} + \Delta E, \quad (5.14)$$

whereby the confinement energy is given by [54]:

$$\Delta E = \frac{\hbar^2 \pi^2}{2m_e t_{ch}^2}. \quad (5.15)$$

5.2 Closed-Form Solution of the 2D Potential

The accurate closed-form potential solution is the next step to describe the device properly. In order to take respect to the potential drop inside the highly doped source and drain regions, an effective built-in potential $\Phi_{bi,eff,s/d}$ is calculated in Sec. 5.2.1. The effective built-in potential estimates the potential at the source and drain to channel junctions which is used as boundary condition. Applying the Schwarz-Christoffel transformation, the 2D Laplace equation is calculated within the device channel. This technique requires a mapping of the integration limits, introduced in Sec. 5.2.2. After all in Sec. 5.2.3 three different kinds of boundary conditions are applied to the Poisson integral.

5.2.1 Effective Built-in Potentials

The potential within the channel region is described by its boundary conditions. These boundary conditions have to be determined in a prior step (see Fig. 5.3). The effective gate potential V'_{gs} calculated in Eq. (5.13) is applied on both sides of the gate. At the source to channel junction and drain to channel junction the applied boundary conditions are described by the effective built-in potential $\Phi_{bi,eff,s/d}$:

$$\Phi_{bi,eff,s/d}(y) = \Phi_{bi,s/d} - \Delta\Phi_{bi,s/d}(y), \quad (5.16)$$

where the source case is given by $\Phi_{bi,eff,s}$ and the drain case by $\Phi_{bi,eff,d}$. The effective built-in potential is derived from the built-in potential in source and drain region $\Phi_{bi,s/d}$, whereby $\Delta\Phi_{bi,s/d}$ is calculated by [53][79]:

$$\begin{aligned} \Delta\Phi_{bi,s/d}(y) = & \Phi_{bi,s/d} + V_{s/d} - \Phi_{sp} + \lambda(y)^2 \cdot \frac{q}{\varepsilon_{si}} \cdot N_D \\ & \cdot \left[1 - \sqrt{1 + \frac{2(\Phi_{bi,s/d} + V_{s/d} - \Phi_{sp})}{\lambda(y)^2 \frac{q}{\varepsilon_{si}} N_D}} \right], \end{aligned} \quad (5.17)$$

with N_D is the donor doping concentration, ε_{si} is the silicon permittivity, $V_{s/d}$ is the source and drain bias. The screening length $\lambda(y)$ shows the approximated potential bending in x -direction at the source to channel and drain to channel junction [53][80]:

$$\lambda(y) = \lambda_{fit} \sqrt{\frac{\varepsilon_{ch} \cdot t_{in} \cdot t_{ch}}{2 \cdot \varepsilon_{in}} \left(1 + \frac{\varepsilon_{in} \cdot y}{\varepsilon_{ch} \cdot t_{in}} - \frac{\varepsilon_{in} \cdot y^2}{\varepsilon_{ch} \cdot t_{in} \cdot t_{ch}} \right)}, \quad (5.18)$$

whereby λ_{fit} is a fitting factor, typically in the range of 0.9 to 1. The surface potential Φ_{sp} is the potential at the channel to insulator junctions assumed for a long channel device:

$$\Phi_{sp} = -(V'_{gs} - V_{fb} - V_{in}), \quad (5.19)$$

with V_{in} is the voltage drop across the insulator calculated by:

$$V_{in} = \frac{q \cdot n_i \cdot t_{ch} \cdot t_{in}}{2 \cdot \varepsilon_{in}}. \quad (5.20)$$

5.2.2 Integration Limits

The Poisson integral is solved for several position dependent intervals. In order to perform the integration, all vertexes are mapped by Eq. (5.9) from z -plane into w -plane. The conformal mapping technique requires that the position of \bar{u}_1'' and \bar{u}_1' are located in infinity. To simplify this statement, both positions are chosen to be located at three times the channel length $3 \cdot l_{ch}$. The six vertexes, which describe the device as shown in Fig. 5.4, represent the integration limits and are calculated by:

$$\bar{u}_1'' = \cosh \left(\frac{\pi (3l_{ch} + i(2\tilde{t}_{in} + t_{ch}))}{t_{dev}} \right), \quad (5.21)$$

$$\bar{u}_2 = \cosh \left(\frac{\pi (0 + i(2\tilde{t}_{in} + t_{ch}))}{t_{dev}} \right), \quad (5.22)$$

$$\bar{u}_3 = \cosh \left(\frac{\pi (0 + i(\tilde{t}_{in} + t_{ch}))}{t_{dev}} \right), \quad (5.23)$$

$$\bar{u}_4 = \cosh \left(\frac{\pi (0 + i(\tilde{t}_{in}))}{t_{dev}} \right), \quad (5.24)$$

$$\bar{u}_5 = \cosh \left(\frac{\pi (0 + i0)}{t_{dev}} \right), \quad (5.25)$$

$$\bar{u}_1' = \cosh \left(\frac{\pi (3l_{ch} + i0)}{t_{dev}} \right). \quad (5.26)$$

5.2.3 Boundary Conditions and Potential Solution Within the Channel

The Laplace solution within the device region, more precisely channel and insulator, is described by different kinds of boundary conditions (see Fig. 5.6). For this case, three different kinds of boundary conditions are applied. Both gates have a constant potential for the entire length and therefore the potential is described by constant boundary conditions. Since the potential within both insulator regions varies almost linearly, it is described by a linear function. The third case is given at the source and drain to channel junctions where the potential varies according to a parabolic function. This parabolic function is getting separated into the parabolic part and into the constant factor. The potential within the channel is calculated separately for each case

and superposed afterwards:

$$\varphi_{ch} = \varphi_{const} + \varphi_{lin} + \varphi_{para}. \quad (5.27)$$

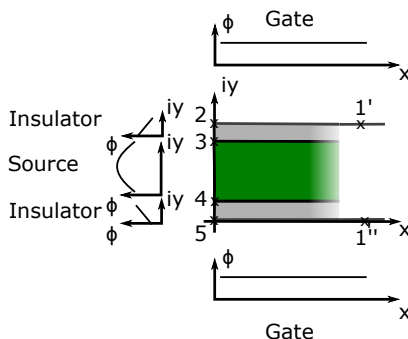


Figure 5.6: Boundary conditions for the source related case.

Constant Boundary Conditions

The Poisson integral of Eq. (4.29) for constant boundary condition $\phi(\bar{u}) = \phi_{const}$ is given by:

$$\varphi_{const}(w(z)) = \frac{1}{\pi} \int_{\bar{u}_a}^{\bar{u}_b} \frac{v}{(u - \bar{u})^2 + v^2} \phi_{const} d\bar{u} = -\frac{\phi_{const}}{\pi} \tan^{-1} \left(\frac{u - \bar{u}}{v} \right) \Big|_{\bar{u}_a}^{\bar{u}_b}. \quad (5.28)$$

The constant boundary conditions are shown in Table 5.2. Superposing all four parts (top gate $\varphi_{const,g1}$, bottom gate $\varphi_{const,g2}$, source to channel junction $\varphi_{const,s}$ and drain to channel junction $\varphi_{const,d}$) leads to the overall potential for constant boundary conditions:

$$\varphi_{const} = \varphi_{const,g1} + \varphi_{const,g2} + \varphi_{const,s} + \varphi_{const,d}. \quad (5.29)$$

Potential	ϕ_{const}	\bar{u}_a	\bar{u}_b
$\varphi_{const,g1}$	V'_{gs}	\bar{u}'_1	\bar{u}_2
$\varphi_{const,g2}$	V'_{gs}	\bar{u}_5	\bar{u}''_1
$\varphi_{const,s}$	$\Phi_{bi,eff,s}(y=0)$	\bar{u}_3	\bar{u}_4
$\varphi_{const,d}$	$\Phi_{bi,eff,d}(y=0) - V'_{gs}$	\bar{u}_3	\bar{u}_4

Table 5.2: Summary of the constant boundary conditions ϕ_{const} which are applied at each gate g_1, g_2 as well as for the source s and drain d boundary. φ_{const} is the potential solution between the two points \bar{u}_a and \bar{u}_b along the u -axis.

Linear Boundary Conditions

The almost linear potential drop within the insulator can be described within z -plane by $\phi_{lin}(z) = E_{in} \cdot y$. For this reason the linear boundary condition in w -plane is given by $\phi(\bar{u}) = E_{in} \cdot \frac{t_{dev}}{\pi} \cosh^{-1}(\bar{u})$. The Poisson integral of Eq. (4.27) with applying the linear boundary condition $\phi(\bar{u})$ results in:

$$\varphi_{lin}(w(z)) = \frac{1}{\pi} \int_{-\infty}^{\infty} \frac{v}{(u - \bar{u})^2 + v^2} \cdot \frac{t_{dev}}{\pi} \cosh^{-1}(\bar{u}) d\bar{u}. \quad (5.30)$$

In order to give an expression which can be integrated in a closed-form, the boundary condition of a linear function is approximated by a square root one:

$$E_{in} \cdot \frac{t_{dev}}{\pi} \cosh^{-1}(u) \approx \pm \sqrt{\frac{\bar{u} - b}{a}}, \quad (5.31)$$

whereby the parameter a is a function of the linear boundary condition ϕ_{lin} . The Poisson integral for linear boundary conditions is finally given by:

$$\varphi_{lin}(w(z)) = \frac{1}{\pi} \int_{\bar{u}_a}^{\bar{u}_b} \frac{v}{(u - \bar{u})^2 + v^2} \cdot \pm \sqrt{\frac{\bar{u} - b}{a}} d\bar{u}, \quad (5.32)$$

whereby a detailed derivation of a and b as well as a detailed solution for φ_{lin} is presented in [81]. The potentials for the linear boundary conditions are summarized in Table 5.3.

Potential	ϕ_{lin}	\bar{u}_a	\bar{u}_b
$\varphi_{lin,s1}$	$V'_{gs} - \Phi_{bi,eff,s}(y=0)$	\bar{u}_4	\bar{u}_5
$\varphi_{lin,s2}$	$\Phi_{bi,eff,s}(y=0) - V'_{gs}$	\bar{u}_2	\bar{u}_3
$\varphi_{lin,d1}$	$V'_{gs} - \Phi_{bi,eff,d}(y=0)$	\bar{u}_2	\bar{u}_3
$\varphi_{lin,d2}$	$\Phi_{bi,eff,d}(y=0) - V'_{gs}$	\bar{u}_4	\bar{u}_5

Table 5.3: Potential solution φ_{lin} for the linear boundary conditions ϕ_{lin} between the points \bar{u}_a and \bar{u}_b . $\varphi_{lin,s1}$ and $\varphi_{lin,s2}$ describe the potential drop in both insulator regions of the source related case, whereas $\varphi_{lin,d1}$, $\varphi_{lin,d2}$ describe the same for the drain related case.

The total potential for the case of linear boundary conditions is given by:

$$\varphi_{lin} = \varphi_{lin,s1} + \varphi_{lin,s2} + \varphi_{lin,d1} + \varphi_{lin,d2}. \quad (5.33)$$

Parabolic Boundary Conditions

The influence of the gate potential on the electrostatic at the channel surface is the biggest and decreases by getting closer to the channel center. This decreasing influence is considered by parabolic boundary conditions at the source and drain to channel junctions. For this case, the boundary condition $\phi(\bar{u})$ of the Poisson integral (see Eq. (4.27)) is approximated with:

$$\phi(\bar{u}) = \phi_{para} \cdot \sqrt{1 - \bar{u}^2}. \quad (5.34)$$

The unknown parameter ϕ_{para} is calculated by the difference of the effective built-in potential at the surface $y = 0$ and the channel center $y = t_{ch}/2$:

$$\phi_{para} = \Phi_{bi,eff,s/d}(y = t_{ch}/2) - \Phi_{bi,eff,s/d}(y = 0). \quad (5.35)$$

The Poisson integral to calculate this shape is valid for $t_{ch} \ll l_{ch}$ [81]:

$$\varphi_{para}(w(z)) = \frac{1}{\pi} \int_{\bar{u}_a}^{\bar{u}_b} \frac{v}{(u - \bar{u})^2 + v^2} \phi_{para} \cdot \sqrt{1 - \bar{u}^2} d\bar{u}. \quad (5.36)$$

The integration finally leads to:

$$\varphi_{para}(w(z)) = \phi_{para} \cdot \left[\frac{1}{2} \left(\sqrt{1 - (u - iv)^2} + \sqrt{1 - (u + iv)^2} \right) - v \right]. \quad (5.37)$$

Potential	ϕ_{para}	\bar{u}_a	\bar{u}_b
$\varphi_{para,s}$	$\Phi_{bi,eff,s}(y = t_{ch}/2) - \Phi_{bi,eff,s}(y = 0)$	\bar{u}_4	\bar{u}_5
$\varphi_{para,d}$	$\Phi_{bi,eff,d}(y = t_{ch}/2) - \Phi_{bi,eff,d}(y = 0)$	\bar{u}_2	\bar{u}_3

Table 5.4: Summary of the parabolic boundary conditions ϕ_{para} which are applied at the source to channel s and drain to channel d junctions.

The total potential for the parabolically shaped boundary conditions is given by:

$$\varphi_{para} = \varphi_{para,s} + \varphi_{para,d}. \quad (5.38)$$

5.3 Gate Influence on the Source and Drain Regions

With shrinking channel length l_{ch} the SD tunneling distance decreases as well. The SD tunneling comes into play for channel length below 10 nm. With every shrinking nanometer the SD tunneling probability rises. Until now, the potential spreading into the source and drain region is not considered. Due to the potential extensions into the source and drain region, the tunneling distance is increased by some nanometers. For an example channel length of 6 nm

an extension of 2 nm for each side increases the total tunneling distance by 66 %. In [82] an analytical formalism was introduced to calculate these extensions, which is implemented for this DG MOSFET model. The applied solution is based on two parabolic functions which are built at the surface $y = 0$ and center $y = t_{ch}/2$. The potential bending distance from source and drain to channel junction into the source region is given by subscript s and for the drain region by subscript d [53]:

$$d_{s/d}(y) = -\lambda(y) + \sqrt{\lambda^2(y) + \frac{(\Phi_{bi,eff,s/d} - \Phi_{sp} + V_{s/d}) \cdot 2 \cdot \epsilon_{s/d}}{qN_{s/d}}}, \quad (5.39)$$

with λ is the y -dependent screening length given by Eq. (5.18) and Φ_{sp} given by Eq. (5.19). The decay in x -direction of the potential within the source and drain region is described by parabolic functions as follows:

$$\varphi_{s,x}(x,y) = \frac{\Phi_{bi,eff,s}(y) - \Phi_{bi,s}}{d_s^2(y)} \cdot (x - d_s(y))^2 + \Phi_{bi,s}, \quad (5.40)$$

$$\varphi_{d,x}(x,y) = \frac{\Phi_{bi,eff,d}(y) - \Phi_{bi,d}}{d_d^2(y)} \cdot (x - (l_{ch} + d_d)(y))^2 + \Phi_{bi,d}. \quad (5.41)$$

The 2D potential bending in source and drain region is calculated by:

$$\varphi_{s/d}(x,y) = \frac{\varphi_{s/d,x}(x,y=0) - \varphi_{s/d,x}(x,y=t_{ch}/2)}{t_{ch}/2^2} \cdot (y - t_{ch}/2)^2 + \varphi_{s/d,x}(x,y=t_{ch}/2). \quad (5.42)$$

For those regions which are unaffected by the gate potential, the potential is given by the built-in potential $\Phi_{bi,s}$ and $\Phi_{bi,d}$.

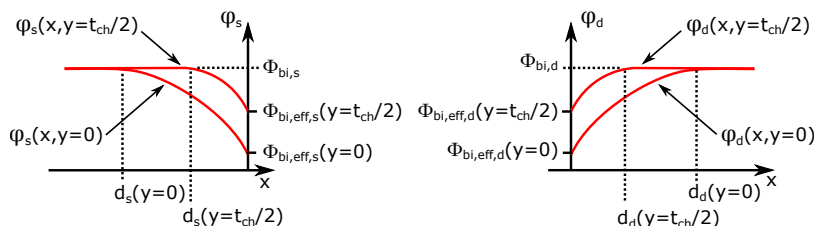


Figure 5.7: Source and drain potential extensions of the MOSFET. The potential at the surface $y = 0$ is more influenced by the gate electrode than at the center $y = t_{ch}/2$.

5.4 Band Structure

In a further step the band structure is calculated, whereby the potential throughout the device φ is given by the former potential solution of Sec. 5.2 and Sec. 5.3. Ultra-short channel devices commonly have highly doped source and drain regions. The high doping concentrations lead to band gap narrowing (bgn) which influences the band structure in both regions. Bgn reduces

with:

$$\Delta\Phi_{bi,s}(y) = \Phi_{bi,s} + V_s - \Phi_{sp} + \lambda(y)^2 \cdot \frac{q}{\epsilon_{si}} \cdot N_A \cdot \left[1 - \sqrt{1 + \frac{2(\Phi_{bi,s} + V_s - \Phi_{sp})}{\lambda(y)^2 \frac{q}{\epsilon_{si}} N_A}} \right], \quad (5.46)$$

whereby N_A describes the acceptor doping concentration. By applying the equations introduced

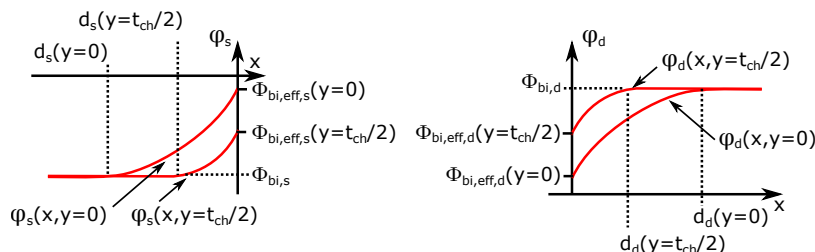


Figure 5.9: Source and drain potential extensions of the TFET. The potential at the surface $y = 0$ is more influenced by the gate electrode than at the center $y = t_{ch}/2$.

in Sec. 5.4 the band structure for the DG TFET can be calculated in a same manner (see Fig. 5.10).

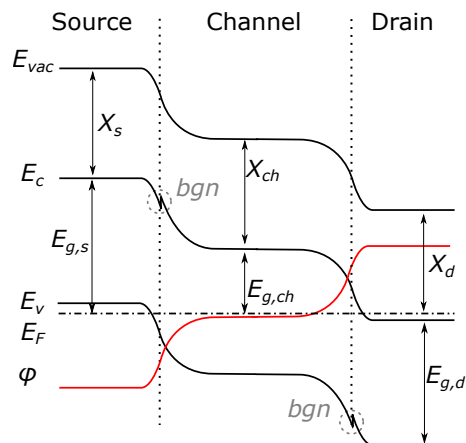


Figure 5.10: Potential profile φ and band structure E_c , E_v of a DG TFET. Shown are additionally the Fermi level E_F and the vacuum level E_{vac} as well as the band gap E_g and electron affinity X .

5.6 MOSFET Potential Model Verification

The 2D potential model of the DG MOSFET is verified by applying the parameters listed in Table 5.5. The channel length is varied for three different device structures. The reference data is given by the numerical NEGF based nanoMOS TCAD [38] [84]. Beginning with a device having a channel length of $l_{ch} = 30$ nm, the surface conduction band $E_c(x,0)$ is shown in Fig. 5.11 and the center conduction band $E_c(x,t_{ch}/2)$ is shown in Fig. 5.12, with an applied drain bias of $V_{ds} = 0.4$ V. Shrinking the channel length to a length of $l_{ch} = 10$ nm is shown in Fig. 5.13 and Fig. 5.14 for the surface and center conduction band, respectively. The minimum channel length is given for $l_{ch} = 6$ nm, shown for a high drain bias of $V_{ds} = 0.4$ V in Fig. 5.15 and Fig. 5.16 for the relating surface and center conduction band. Lowering the drain bias to $V_{ds} = 0.05$ V is shown in Fig. 5.17 and Fig. 5.18 for the surface and center conduction band, respectively. The focus is on an accurate device current and therefore the fitting of the band structure shows some deviations. Nevertheless, all figures show a good agreement for below threshold operation whereby above threshold the deviation increases. One should keep, in mind that the TCAD simulation data is given by a far more complex and iterative calculations. Another difference of the TCAD data are the floating boundary conditions which allow the contact voltage to float [84]. These floating boundary conditions can easily be seen for the center conduction band slices at the source and drain contacts.

Parameter	Value
l_{ch}	6-30 nm
t_{ch}	2 nm
t_{in}	1 nm
l_{sd}	10 nm
m	$0.19 \cdot m_0$
ε_{si}	$11.7 \cdot \varepsilon_0$
ε_{in}	$25 \cdot \varepsilon_0$
N_s	$2 \cdot 10^{20} \text{ cm}^{-3}$
N_d	$2 \cdot 10^{20} \text{ cm}^{-3}$
Device Material	Silicon
Gate Material	Aluminum

Table 5.5: Model simulation parameter set for the extremely scaled DG MOSFET.

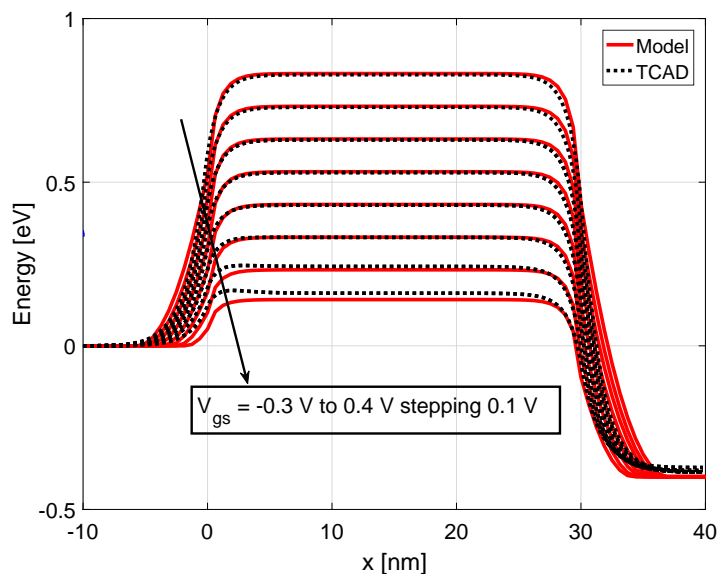


Figure 5.11: Surface conduction band of a DG MOSFET with a channel length of $l_{ch} = 30 \text{ nm}$ compared with TCAD simulation data for different gate voltages and an applied drain bias of $V_{ds} = 0.4 \text{ V}$.

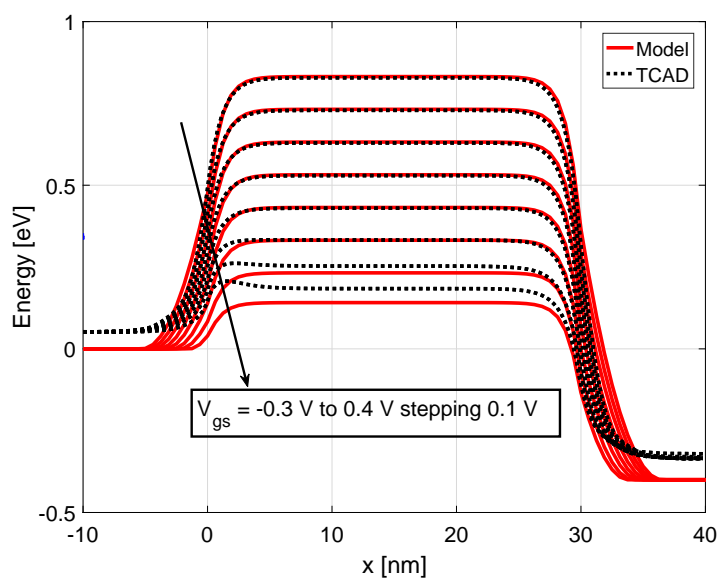


Figure 5.12: Conduction band at the center position of a DG MOSFET with a channel length of $l_{ch} = 30 \text{ nm}$ for different gate voltages and an applied drain bias of $V_{ds} = 0.4 \text{ V}$, compared with TCAD simulation data.

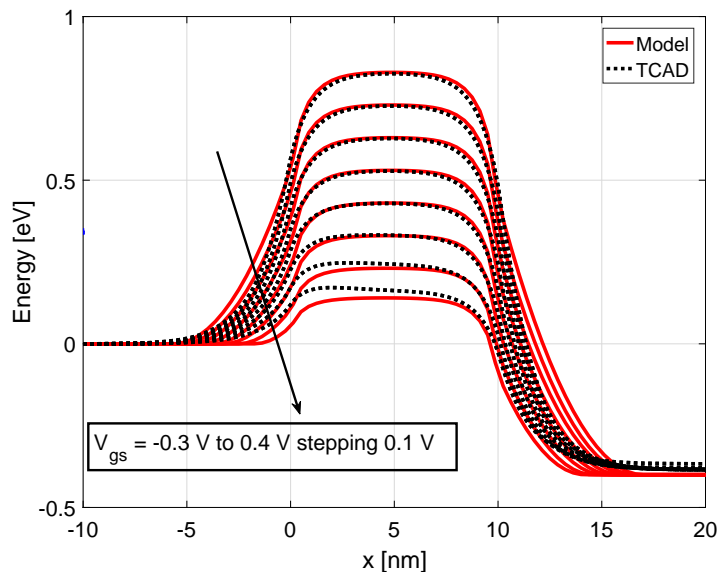


Figure 5.13: Surface conduction band of a DG MOSFET with a short channel length of $l_{ch} = 10$ nm verified with TCAD simulation data for different gate voltages and an applied drain bias of $V_{ds} = 0.4$ V.

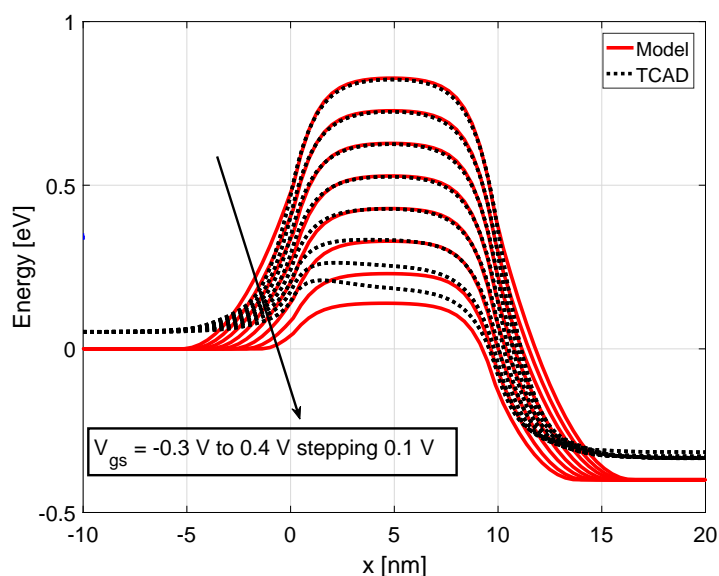


Figure 5.14: Conduction band at the center position of a DG MOSFET with a short channel length of $l_{ch} = 10$ nm for different gate voltages and an applied drain bias of $V_{ds} = 0.4$ V, verified with TCAD simulation data.

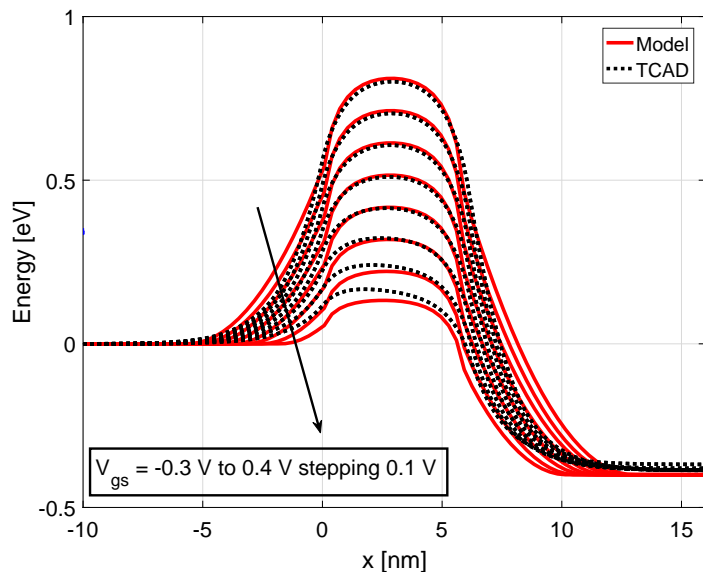


Figure 5.15: Surface conduction band of a DG MOSFET with an ultra-short channel length of $l_{ch} = 6$ nm compared with TCAD simulation data for different gate voltages and an applied drain bias of $V_{ds} = 0.4$ V.

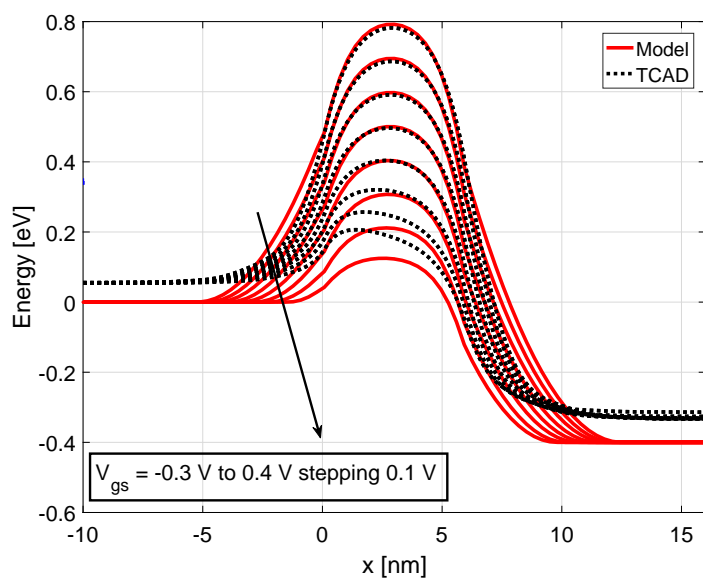


Figure 5.16: Conduction band at the center position of a DG MOSFET with an ultra-short channel length of $l_{ch} = 6$ nm for different gate voltages and an applied drain bias of $V_{ds} = 0.4$ V, compared with TCAD simulation data.

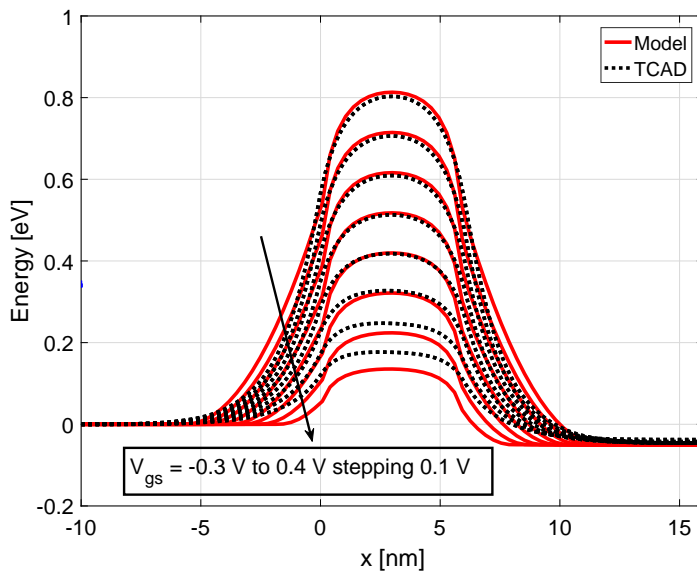


Figure 5.17: Surface conduction band of a DG MOSFET with an ultra-short channel length of $l_{ch} = 6$ nm verified with TCAD simulation data for different gate voltages and an applied drain bias of $V_{ds} = 0.05$ V.

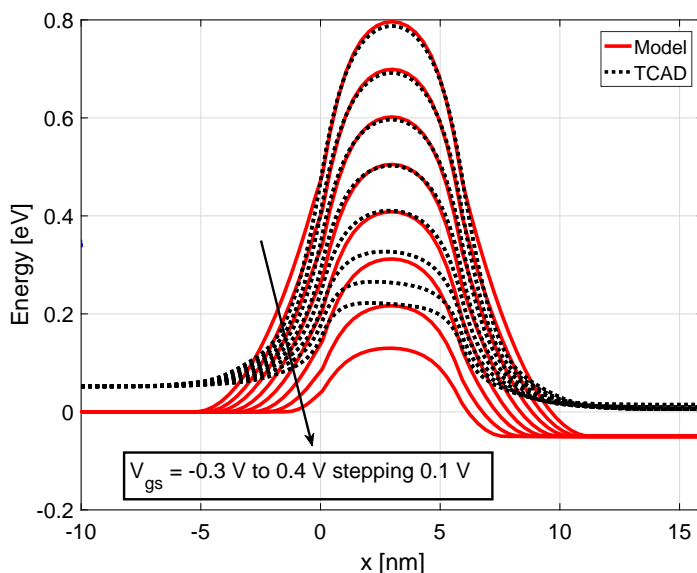


Figure 5.18: Center conduction band of a DG MOSFET with an ultra-short channel length of $l_{ch} = 6$ nm for different gate voltages and an applied drain bias of $V_{ds} = 0.05$ V, verified with TCAD simulation data.

5.7 TFET Potential Model Verification

The 2D potential model of the DG TFET is verified by applying the parameters listed in Table 5.6. The solution leads to the potential as well as the band structure in the source and channel region. The band calculation in comparison with numerical TCAD Sentaurus simulation data [26] is shown in Fig. 5.19. Since the focus is on the on-state, only the band structure for the source and channel region is shown. Additionally, only the surface band structure is shown, because the current resulting from this position dominates the device current [67].

Parameter	Value
l_{ch}	22 nm
t_{ch}	10 nm
t_{in}	2 nm
l_{sd}	20 nm
ϵ_{si}	$11.7 \cdot \epsilon_0$
ϵ_{in}	$25 \cdot \epsilon_0$
N_s	$1 \cdot 10^{20} \text{ cm}^{-3}$
N_d	$1 \cdot 10^{20} \text{ cm}^{-3}$
Device Material	Silicon

Table 5.6: Model simulation parameter set for the DG TFET.

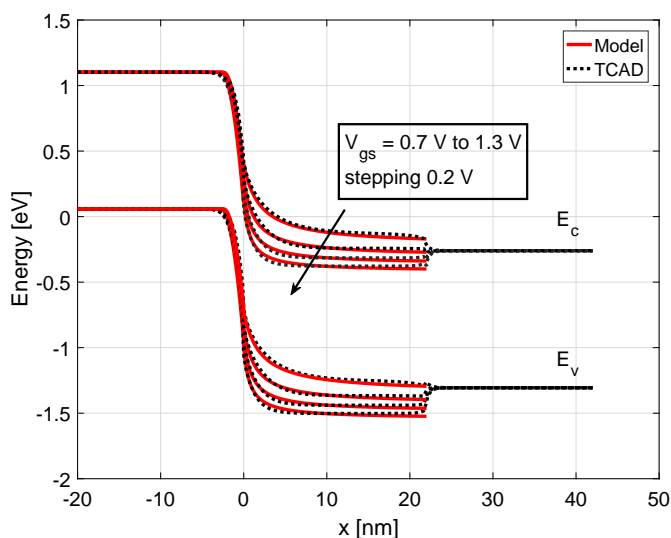


Figure 5.19: Shown is the comparison between the analytical TFET model and the Sentaurus TCAD simulation data of the energy bands for a bias of $V_{ds} = 0.2 \text{ V}$.

CHAPTER 6

MOSFET Current Model

The former section introduced the way to calculate the conduction band for the entire device. This section focuses on the calculation of the device current and therefore the conduction band is applied to the NEGF in Sec. 6.1. The ballistic NEGF formalism is applied in Sec. 6.2 to calculate the current for ultra-short channel devices. In Sec. 6.3 the numerical efficiency of the NEGF formalism is increased by using mathematical approximations. By considering the backscattering in Sec. 6.4, the model can be extended to longer channel devices. Finally, the current model is verified with the help of numerical TCAD simulation data in Sec 6.5. Applying this model, investigations on short-channel effects are done in Sec. 6.6.

6.1 Slicing of the Conduction Band

As stated before, the NEGF is a time consuming numerical method. To find a balance between simulation time and accuracy, the NEGF is implemented in 1D. In order to consider 2D effects in the device behavior, it is necessary to extract more than just one 1D slice. Therefore, the 2D conduction band $E_c(x,y)$ is cut into 1D slices in x -direction at several y -positions, which leads to $E_c(x)$. The NEGF treats the conduction band slice as an individual profile $U(x)$, each leading to an independent current. The drawback of using more slices is an increasing simulation time. A trade-off for this analytical model is given by extracting only two 1D slices out of the 2D profile. The first close to the channel surface, which results in the surface current density J_s , and the second at the channel center which leads to the center current density J_c (see Fig. 6.1).

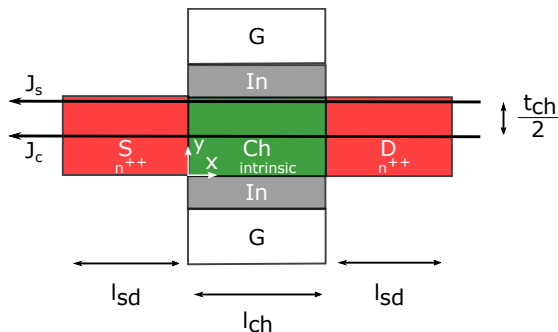


Figure 6.1: Cross-section of the considered ultra-short DG MOSFET. J_s and J_c show the position dependent slices for the 1D current calculation.

6.2 Current Calculation by NEGF

In contrast to the derivation of the full NEGF approach as it was shown in Sec. 4.2, in the following only the model relevant equations are summarized. These equations are based on a self-consistent 1D NEGF method for considering quantum current transport in highly doped resistors presented in [42].

6.2.1 Hamiltonian Matrix

The effective mass Hamiltonian, to describe the particle flow in x -direction is expressed by:

$$H_L = E_c - \frac{\hbar^2 d^2}{2mdx^2} + U(x), \quad (6.1)$$

with $U(x)$ is the 1D energy profile of the conduction band, calculated by the potential solution introduced in Section 5.4 at discrete y -positions inside the source, drain and channel region. Schrödinger's wave equation in combination with the Hamiltonian operator shown in Eq. (6.1) is given by:

$$\mathbf{H}_L \psi = E \psi. \quad (6.2)$$

In order to perform the second derivative shown in Eq. (6.1) the finite difference approximation is applied: The finite difference approximation makes use of a discrete lattice in real space in order to describe the wavefunction of each element $1 \leq i \leq N$ using its preceding $i - 1$ and following element $i + 1$:

$$E \psi_i = -t \psi_{i-1} + (E_c + 2t + U(i)) \psi_i - t \psi_{i+1}, \quad (6.3)$$

with $t = \hbar^2 / (2ma^2)$ and a is the finite grid size with an approximate length of 0.3 nm. Eq. (6.3) can be expressed by a system of linear equations, in order to describe each cell of the

discrete lattice by its former and following element. This system is expressed by the tridiagonal Hamiltonian matrix \mathbf{H}_L having a size of about 100×100 . The matrix contains $E_c + 2t + U(x)$ on the diagonal and $-t$ on the upper and lower diagonals:

$$\mathbf{H}_L = \begin{bmatrix} E_c + 2t + U(1) & -t & 0 & \cdots & 0 \\ -t & E_c + 2t + U(2) & -t & \cdots & 0 \\ 0 & -t & E_c + 2t + U(3) & \cdots & 0 \\ \vdots & \ddots & \ddots & \ddots & \vdots \\ 0 & \cdots & 0 & -t & E_c + 2t + U(N) \end{bmatrix}. \quad (6.4)$$

Considering Eq. (6.3), for the case of $i = 1$ the element ψ_1 does not have a well-defined preceding element ψ_0 . The same refers to the opposite of the device $i = N$, the last element ψ_N does not have a well-defined following element ψ_{N+1} . Both elements are described by the boundary conditions. By adjusting both boundary conditions to zero, Eq. (6.2) can be rewritten as:

$$(\mathbf{E}\mathbf{I} - \mathbf{H}_L)\psi = 0, \quad (6.5)$$

with \mathbf{I} constitutes the identity matrix having the same size of \mathbf{H}_L .

6.2.2 Self-Energy Functions

The incorporation of the wavefunction of the left and right contact is given by the self-energy functions Σ_1 and Σ_2 . Both functions characterize the unknown first element ψ_0 for $i = 1$ of Eq. (6.3) and the last element ψ_{N+1} for $i = N$. The applied self-energy functions tread the device to just have outgoing waves at the ends by simply adding the term $-t \exp(ik_1 a)$ to the first and last cell of $\mathbf{H}_L(1,1)$ and $\mathbf{H}_L(N,N)$ [42]. The self-energy function of the first contact Σ_1 and second contact Σ_2 is given by:

$$\Sigma_1 = \begin{bmatrix} -t \exp(ik_1 a) & 0 & \cdots & 0 \\ 0 & 0 & \cdots & 0 \\ \vdots & \vdots & \ddots & \vdots \\ 0 & 0 & \cdots & 0 \end{bmatrix}, \quad \Sigma_2 = \begin{bmatrix} 0 & \cdots & 0 & 0 \\ \vdots & \ddots & \vdots & \vdots \\ 0 & \cdots & 0 & 0 \\ 0 & \cdots & 0 & -t \exp(ik_2 a) \end{bmatrix}, \quad (6.6)$$

where $(k_1 a)$ is given by the dispersion relation of an infinitely long uniform structure (see Fig. 4.8):

$$E = E_c + U(1) + 2t(1 - \cos(k_1 a)), \quad (6.7)$$

whereby E is the considered energy. Due to the dispersion relation, the self-energy functions depend on energy and change their values in k -space.

6.2.3 Broadening Functions

The broadening functions Γ_1 and Γ_2 come inevitably with the open boundary conditions and are also needed to describe the connection of the device to the contacts. More precisely, some states from the contacts spread into the channel and some states of the channel spread into the contacts. The overall effect broadens the discrete energies of the channel into continuous density of states. Additionally, the broadening functions indicate the electron escape rates. An electron initially placed in that state will escape into the left or right contact with the time constant \hbar/γ , whereby γ denotes one element of the $\Gamma_{1,2}$ matrix. The broadening functions are built out of the self-energy functions by:

$$\Gamma_1 = i \left[\Sigma_1 - \Sigma_1^* \right], \quad \Gamma_2 = i \left[\Sigma_2 - \Sigma_2^* \right], \quad (6.8)$$

with Σ^* is the conjugate complex of Σ . The self-energy functions treat the open boundary conditions and the broadening inevitably comes together with the connection of the device to the contacts. Therefore, when considering the open boundary conditions, the self-energy functions as well as the broadening are added to the wave function and Eq. (6.5) is rewritten as:

$$[EI - H_L - \Sigma_1 - \Sigma_2] \psi = S = i\gamma. \quad (6.9)$$

6.2.4 Spectral Function

The Green's function is derived from Eq. (6.9) by isolating the variable inside the brackets:

$$G(E) = \left[EI - H_L - \Sigma_1 - \Sigma_2 \right]^{-1}, \quad (6.10)$$

in order to give an appropriate expression for the wavefunction:

$$\psi = G \cdot i\gamma. \quad (6.11)$$

In a further step, the spectral function A is built. More precisely, one spectral function considers the source case A_1 and the second spectral function considers the drain case A_2 . Both are formulated out of the Green's function by multiplying with the Γ of each contact:

$$A_1 = G\Gamma_1G^*, \quad A_2 = G\Gamma_2G^*, \quad (6.12)$$

with G^* is the conjugate complex of G . Each function could be seen as the available density of states initiated by each contact. The oscillating behavior of these states is shown in Fig. 6.2 and Fig. 6.3 for the source case and drain case, respectively. The probability of finding states decays for energies below the conduction band energy.

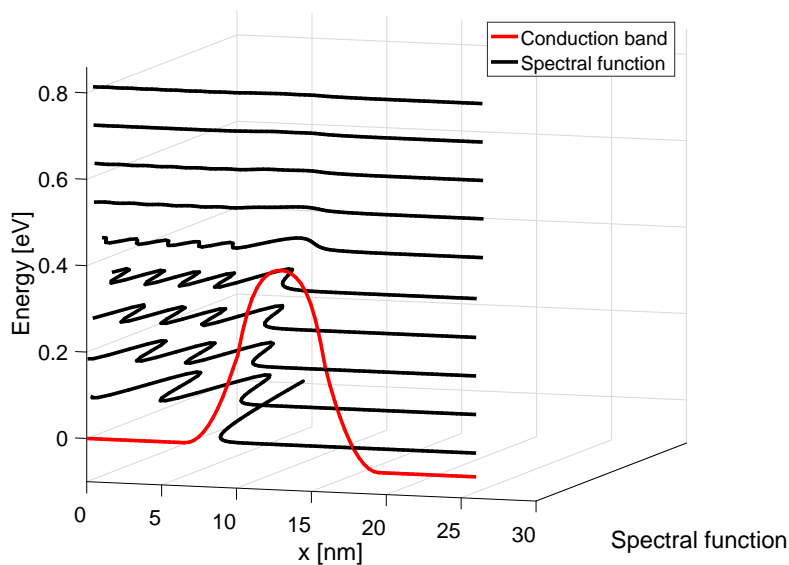


Figure 6.2: Spectral function A_1 initiated by the source contact.

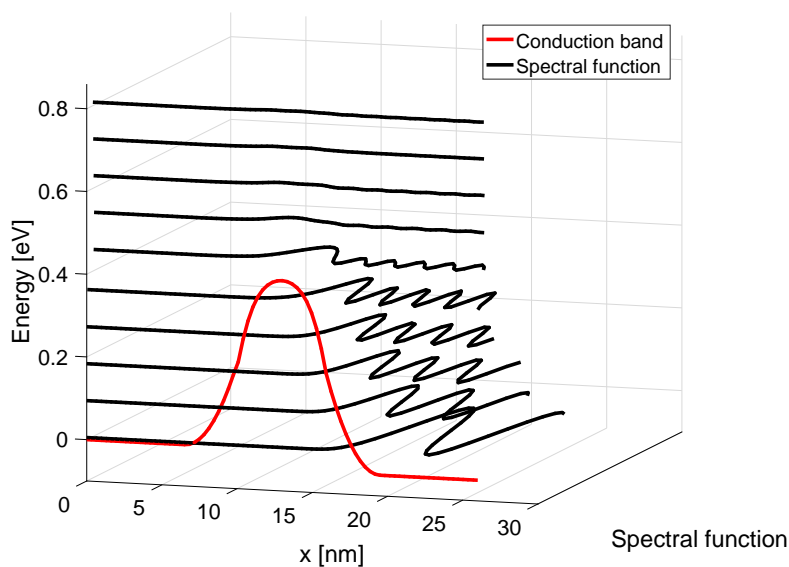


Figure 6.3: Spectral function A_2 initiated by the drain contact.

6.2.5 Fermi Function

The \mathcal{F}_0 distribution is applied to describe the Fermi function for this 2D device [85]:

$$n = N_c \cdot \mathcal{F}_0(\eta), \quad (6.13)$$

$$\mathcal{F}_0(\eta) = \int_0^{\infty} \frac{\xi^0}{1 + e^{\xi - \eta}} d\xi = \ln(1 + e^{\eta}), \quad (6.14)$$

$$\xi = \frac{E - E_c}{k_B \cdot T}, \quad (6.15)$$

$$\eta = \frac{E_F - E_c}{k_B \cdot T}, \quad (6.16)$$

where N_c is the 2D effective density of states, E is the considered energy and E_F is the Fermi level. For this model, the Fermi level is adjusted to achieve a good current characteristic according to the ultra-thin channel thickness.

6.2.6 Density Matrix

Filling up each spectral function \mathbf{A}_1 and \mathbf{A}_2 according to the Fermi function of each contact F_1 and F_2 leads to the electron density matrix $\tilde{\rho}(E)$ of a considered energy E :

$$\tilde{\rho}(E) = \frac{F_1 \cdot \mathbf{A}_1(E) + F_2 \cdot \mathbf{A}_2(E)}{2\pi}. \quad (6.17)$$

The electron density initiated by the source contact and the drain contact is shown as being related to Fig. 6.4 and Fig. 6.5. The total electron density is given by the summation of both parts (see Fig. 6.6). Due to the presence of electrons within the barrier SD tunneling occurs. The interferences result from the incoming and reflecting waves of each contact.

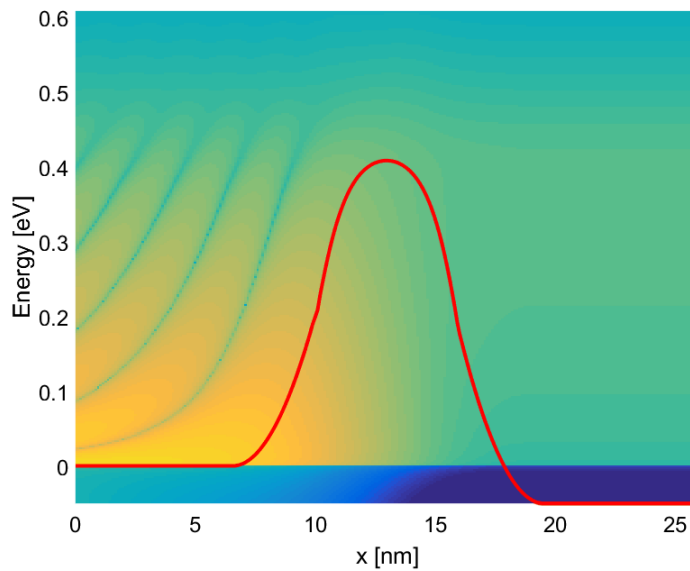


Figure 6.4: Electron density caused by the source spectral function and source Fermi function. Bright colors indicate a high electron density and dark colors indicate a low electron density.

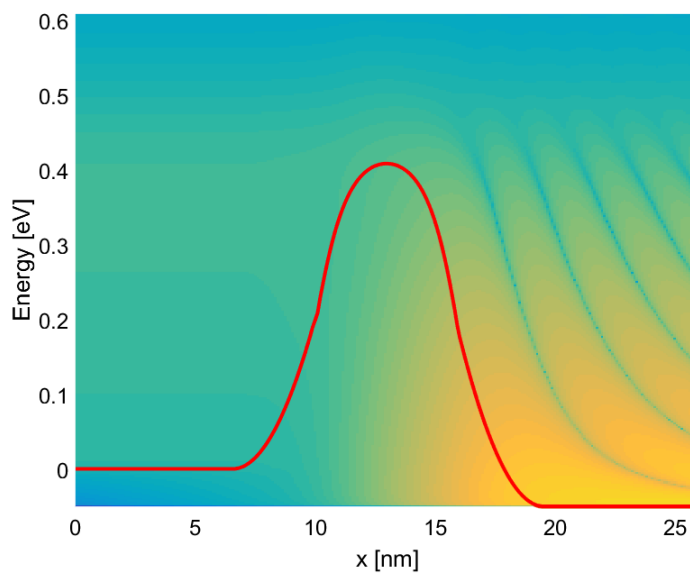


Figure 6.5: Electron density caused by the drain spectral function and drain Fermi function. Bright colors indicate a high electron density and dark colors indicate a low electron density.

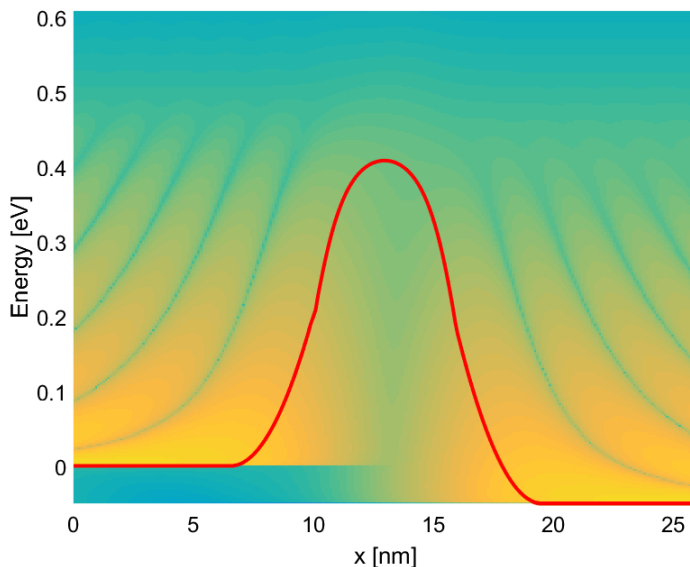


Figure 6.6: Total electron density given by the summation of both parts.

6.2.7 Current Operator

The derivation of the electron density matrix leads to the electron flow in x -direction. The current operator:

$$- (i\hbar mL) \frac{\partial}{\partial x} \quad (6.18)$$

is applied to perform this derivation by using again the finite difference approximation. The current operator is presented in matrix form by:

$$\mathbf{J}_{op} = (t/\hbar N) \begin{bmatrix} 0 & -i & 0 & 0 & \cdots & 0 \\ +i & 0 & -i & 0 & \cdots & 0 \\ 0 & +i & 0 & -i & \cdots & 0 \\ \vdots & \ddots & \ddots & \ddots & \ddots & \vdots \\ 0 & \cdots & 0 & +i & 0 & -i \\ 0 & \cdots & 0 & 0 & +i & 0 \end{bmatrix}, \quad (6.19)$$

with N being the number of points in the lattice.

6.2.8 Energy Dependent Integration

The matrix multiplication of the density matrix $\tilde{\rho}(E)$ and the current operator \mathbf{J}_{op} leads to the current density $\tilde{J}(E, y, z)$. The resulting current density of the considered energy E is given

by the diagonal elements:

$$\tilde{J}(E, y, z) = -q \cdot \text{Trace}(\tilde{\rho}(E) \mathbf{J}_{op}). \quad (6.20)$$

To obtain the total current density Eq. (6.20) is integrated over energy, which is computationally complex, because all associated density matrices are needed:

$$J(y, z) = \int \tilde{J}(E, y, z) dE. \quad (6.21)$$

6.3 Approximations for Increased Numerical Efficiency

An accurate 1D current density calculation requires to calculate the current density according to Eq. (6.20) for many energies and positions within the device cross-section. A reduction from hundreds to few calculations speeds up the total calculation time of the model by almost the same factor. The numerical efficiency is increased in two steps, the first one reduces the number of energy dependent calculations and the second one reduces the number of geometry dependent calculations. Both steps are introduced in the following two sections.

6.3.1 Energy Dependent Approximation

In order to decrease the number of energy dependent calculations without losing much accuracy, the current density is only calculated at some distinctive energies. In a further step, interpolations between these energies are applied. As shown in Fig. 6.7, these energies represent significant points. To describe the behavior of the current density depending on energy in a good manner, the significant points have to be chosen carefully. Some current densities are calculated at energies below the energy barrier E_{barrier} to predict SD tunneling which is important for ultra-short channel device $l_{ch} \leq 10$ nm and less important for longer channels. The other current densities are calculated at energies above E_{barrier} to capture the thermionic emission current (see Fig. 6.7). To avoid oscillations when interpolating the sharp edge which occurs slightly above E_{barrier} (see Fig. 6.17), a linear approximation is applied. In this case, the total current density is approximated with $i = 11$ linear functions which are built out of 12 significant points. This number of points is a trade-off of accuracy and speed, which has proven to be useful for this device. Since the log-scaled plots of Fig. 6.7 show an almost linear behavior, the interpolation parameters a_1 , a_2 of the linear functions are also calculated using the log-scaled values of the calculated current density:

$$\log(\tilde{J}(E, y, z)) \rightarrow a_1, a_2. \quad (6.22)$$

The following interpolation is done by:

$$J_i(y, z) = \int_{E_i}^{E_{i+1}} (10^{a_{1,i} \cdot E + a_{2,i}}) \frac{A}{\text{cm}^2 \text{eV}} dE. \quad (6.23)$$

Summing up all parts of the current density leads to the total 1D current density for all associated energies at one specific y, z -position in the channel cross-section:

$$J(y,z) = \sum_{i=1}^{11} J_i(y,z). \quad (6.24)$$

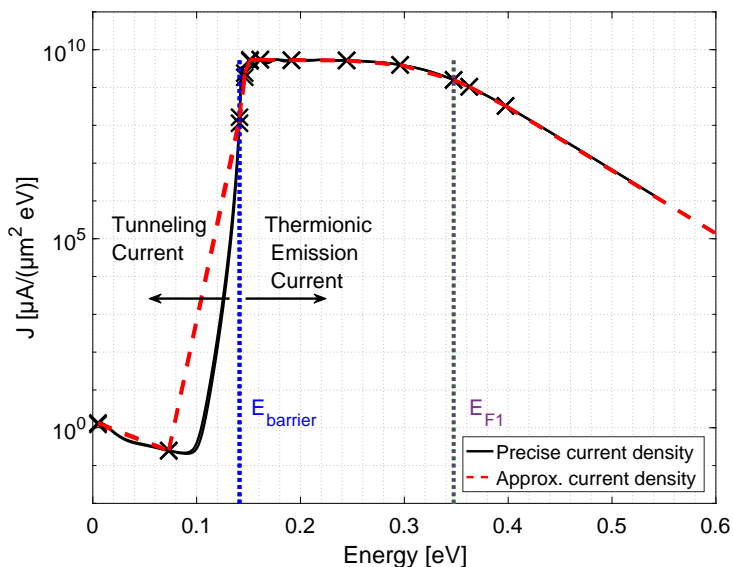


Figure 6.7: Surface current density J_s for different energies at $V_{gs} = 0.4$ V and $V_{ds} = 0.05$ V for channel geometry of $l_{ch} = 30$ nm, $t_{ch} = 2$ nm. The "Precise current density" is calculated at each energy by Eq. (6.20). The "Approx. current density" shows the current density as it is approximated by the mathematical functions of Eq. (6.23), which are defined by the current densities calculated only at positions marked by a "x".

6.3.2 Geometry Dependent Approximation

Furthermore, the current density must be integrated over the channel thickness t_{ch} and channel width w_{ch} to calculate the device current:

$$I_d = \int_{z=0}^{w_{ch}} \int_{y=0}^{t_{ch}} J(y,z) dy dz. \quad (6.25)$$

Describing a 2D device behavior by 1D slices could lead to many discrete calculations. The advantage of considering a DG MOSFET is the mirror-symmetrically device structure. Therefore, the model applies a parabolic current density profile from gate-to-gate which results in an additional simplification. The parabolic dependency of the current is built by calculating

the current density $J(y,z)$ at two y -positions. One current density is calculated at the channel surface J_s and the other at the channel center J_c (see Fig. 6.1). Due to the double-gate device structure the current density at both Si/SiO_2 interfaces is assumed to be equal. These position dependent current densities are applied to derive the parameters b_1, b_2, b_3 of the parabolic function. One half of the device current I_d is given by a closed-form integration using the parabolic function between both positions. The other half of the drain current can be calculated by a multiplication by 2, due to the symmetry of the device. Since the electrostatic behavior of the device in z -dimension is almost constant, the integration shown in Eq. (6.25) is simplified by a multiplication of the device width w_{ch} :

$$I_d = 2 \cdot w_{ch} \cdot \int_0^{t_{ch}/2} (b_1 \cdot y^2 + b_2 \cdot y + b_3) dy. \quad (6.26)$$

6.4 Analytical Treatment of Electron Backscattering

The carrier transport inside the MOSFET is affected by carrier scattering events e.g. surface roughness, phonon-electron, impurity-electron, electron-electron scattering. When considering long channel devices by applying classical transport equations, these scattering types are summarized in the mobility μ . High scattering rates indicate low mobilities and vice versa. Since the NEGF based treatment of scattering, introduced in Sec. 4.2.8 is far too complex when developing a compact model, an analytical treatment of scattering is applied. A straightforward method of considering elementary backscattering processes was presented by [76] and is implemented in the modeling approach (see Fig. 6.8). The model is related to the calculation

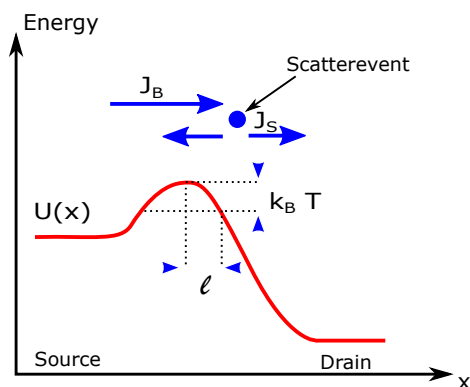


Figure 6.8: Energy profile along the x -axis of the MOSFET and the specific distance l which affects backscattering events. Also shown is the ballistic current density J_B which comes from the source side and the scattering current J_S which enters the drain side.

of the transmission coefficient and reflection for steady state current. Observations of short-

channel devices showed that carriers overcoming the energy barrier only backscatter under certain conditions. In general, the probability of electron backscattering depends on the shape of the energy barrier and the electron's energy. In order to derive a closed-form expression of the backscattering probability, a specific distance is defined. This specific distance l is given by the length along the energy barrier where the energy drops from its maximum by the thermal energy of $k_B T$ (see Fig. 6.8). Quasi ballistic current comes into play if the distance l reaches the scale of the mean free path λ of the carriers:

$$\lambda = 2 \cdot \mu_0 \frac{k_B T}{v_t q}, \quad (6.27)$$

with v_t is the non-degenerate thermal velocity:

$$v_t = \sqrt{2 \frac{k_B T}{m_c}}. \quad (6.28)$$

The parameter μ_0 is fitted to adapt the model to the variety of scattering types. The part of electrons which enter the channel from the source region is reflected by scattering effects and reenters the source region given by:

$$r_C = \frac{l}{l + \lambda}. \quad (6.29)$$

The positive and negative directed fluxes contribute to the electron density, whereby the coefficient which shows the percentage part of the electrons which transmit from the source region to the drain region is given by:

$$T_s = \frac{1 - r_C}{1 + r_C}. \quad (6.30)$$

The ballistic current density J_B needs to be multiplied with the transmission factor $T_s < 1$ to obtain the drain current density J_S including scattering effects:

$$J_S = J_B \cdot T_s. \quad (6.31)$$

As stated before, only those current contributions resulting from an electron energy greater than the maximum of the energy barrier minus $k_B T$ are affected by these scattering events. Electrons which tunnel through the barrier below that energy are not affected because it is assumed that they cannot gain enough energy to overcome the barrier back to the source contact. According to Eq. (6.31), the current density calculation of Eq. (6.23) is partitioned in two energy dependent parts:

$$J_{i,sc} = \begin{cases} J_B & \text{if } E < E_{\text{barrier}} - k_B T \\ J_S & \text{else} \end{cases} \quad (6.32)$$

In order to include scattering in the final device current, this expression for $J_{i,sc}$ is used in Eq. (6.24) instead of J_i .

6.5 MOSFET Model Verification

The analytical model is validated by the NEGF based numerical nanoMOS simulator [38]. Simulations are done for an ultra-short channel n-type DG MOSFET with the parameters listed in Table 6.1. Due to the heavy confinement in the model, the effective density of states and the Fermi level is slightly adapted. The effective mass of carriers for the analytical model and the TCAD simulation are the same. It is assumed that all electrons occupy the lowest subband and therefore the effective mass for motion within the x-y plane is represented by the transverse effective mass $m = 0.19 \cdot m_0$ [62]. First of all, the simulation data for the ballistic device (see Sec. 6.5.1) and then the simulation data for considering backscattering are shown (see Sec. 6.5.2).

Parameter	Value
l_{ch}	6-30 nm
t_{ch}	2 nm
t_{in}	1 nm
l_{sd}	10 nm
ϵ_{si}	$11.7 \cdot \epsilon_0$
ϵ_{in}	$25 \cdot \epsilon_0$
N_s	$2 \cdot 10^{20} \text{ cm}^{-3}$
N_d	$2 \cdot 10^{20} \text{ cm}^{-3}$
Device Material	Silicon
Gate Material	Aluminum

Table 6.1: Model simulation parameter set for the DG MOSFET.

6.5.1 Ballistic transport

Since the applied NEGF formalism is based on the ballistic current calculation, the ballistic transfer current characteristic for an ultra-short channel length of $l_{ch} = 6 \text{ nm}$ is depicted in Fig. 6.9. The figure shows reasonable results for the leakage current as well as for the on-state at different drain biases. Additionally, the slope degradation with increasing V_{ds} is shown. In Fig. 6.10, the ballistic transfer current characteristic for the same device with a channel length of $l_{ch} = 30 \text{ nm}$ is shown. Considering this device, the influence of the drain voltage on the slope degradation is reduced. Due to the ballistic current calculation the on current of the 6 nm device almost equals the on current of the 30 nm device.

The scalability of compact transistor models is an important part and therefore Fig. 6.11 shows the transfer characteristic of the model for different channel thicknesses. The picture also demonstrates the shift of the threshold voltage. This shift is caused by the heavy confinement which occurs for these ultra-thin channels. Fig. 6.12 illustrates the output current characteristic as well as the output conductance for the device with a channel length of $l_{ch} = 6 \text{ nm}$. The oscillations of the output conductance can be reduced by more interpolation steps.

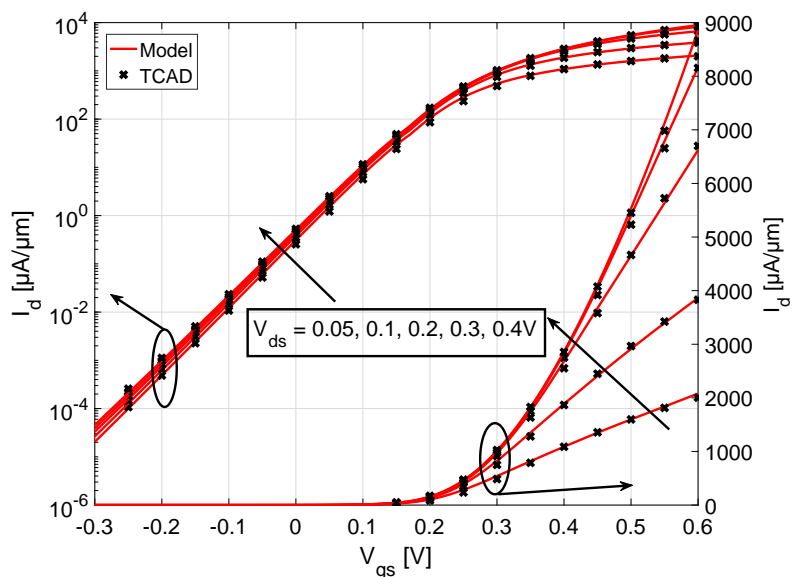


Figure 6.9: Ballistic drain current transfer characteristic at $T = 300$ K for channel length of $l_{ch} = 6$ nm.

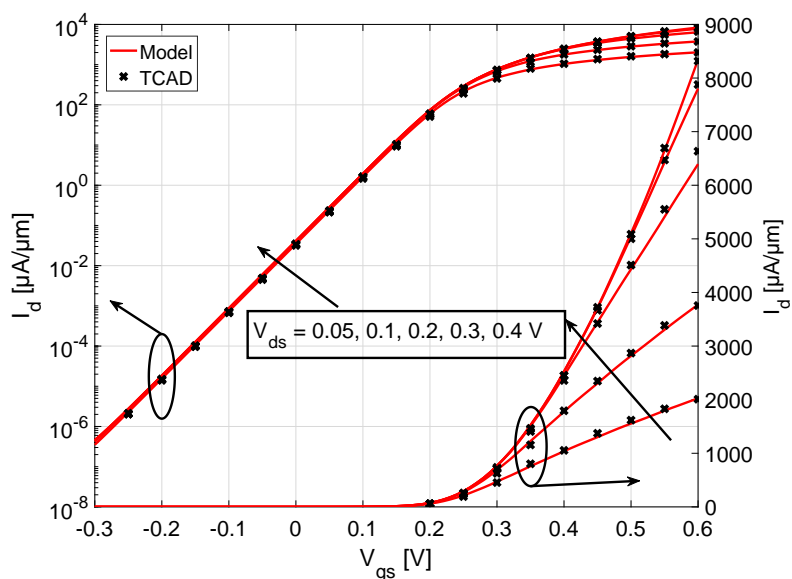


Figure 6.10: Ballistic drain current transfer characteristic at $T = 300$ K for channel length of $l_{ch} = 30$ nm.

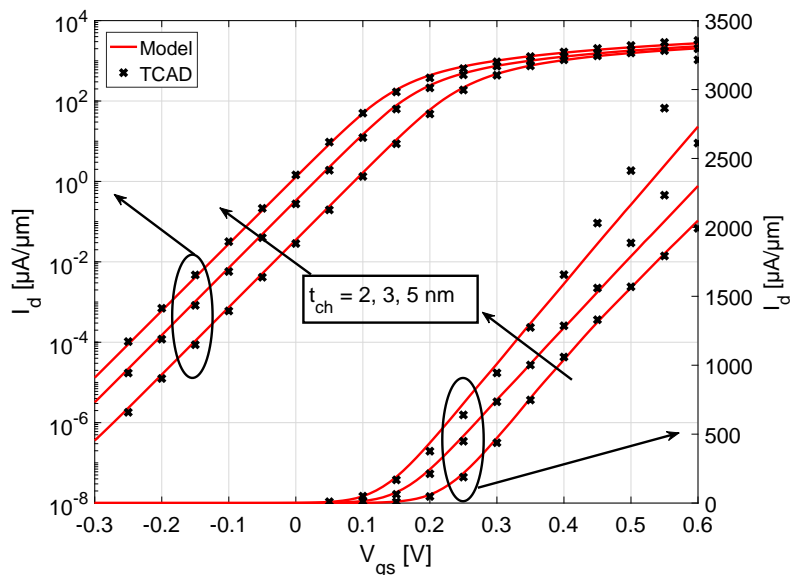


Figure 6.11: Ballistic drain current transfer characteristic at $T = 300$ K for a channel thickness of $t_{ch} = 2, 3, 5$ nm and a channel length of $l_{ch} = 20$ nm and an applied bias of $V_{ds} = 0.05$ V.

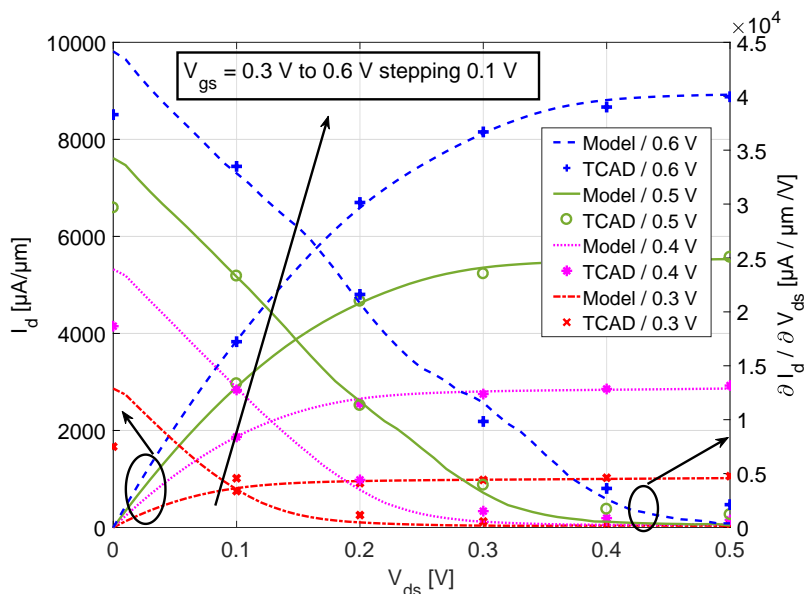


Figure 6.12: The left axis shows the output current characteristic for channel length of $l_{ch} = 6$ nm at $T = 300$ K. The right axis shows the output conductance of the same device. The model results are illustrated by the lines whereas TCAD data is given by the markers.

To highlight the SD tunneling effects, the currents at a temperature of $T = 300$ K are compared to the currents at $T = 75$ K (see Fig. 6.13). For $T = 75$ K, in subthreshold region the thermionic current is repressed and the total current is dominated by the SD tunneling. Fig. 6.13 also indicates the ideal slope of 15 mV/dec, which could be achieved at $T = 75$ K when only thermionic emission current occurs. Whereas both the simulation data and the model data indicate a much worse slope, which is a result of the additional SD tunneling. The difference between $T = 75$ K and $T = 300$ K of the device with a channel length of $l_{ch} = 6$ nm is small because the SD tunneling dominates in both cases. For the device with a channel length of $l_{ch} = 10$ nm the difference increases, in consequence of less SD tunneling current at both temperatures.

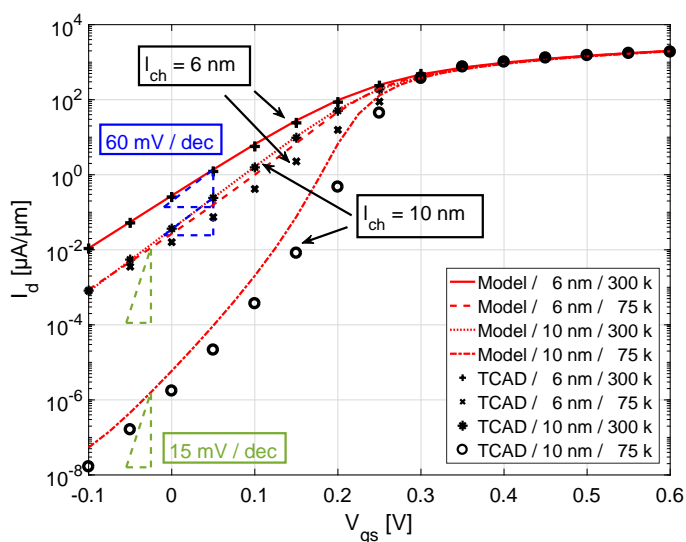


Figure 6.13: Ballistic current transfer characteristic for channel geometry of $l_{ch} = 6, 10$ nm, $t_{ch} = 2$ nm and a drain bias of $V_{ds} = 0.05$ V at $T = 75$ K and 300 K. The triangle, showing a slope of 15 (60) mV/dec, denotes the ideal slope which could be reached for a pure thermionic emission current at $T = 75$ (300) K.

6.5.2 Non-Ballistic transport

The longer the channel, the more important it is to consider the influence of scattering. The influence of scattering increases with higher drain currents I_d which are controlled by the gate voltage V_{gs} and thus Fig. 6.14 shows the output current characteristic of a device, having a channel length of $l_{ch} = 30$ nm. The device current is smaller by considering backscattering in contrast to the ballistic one. Additionally, one can see that the formalism applied to calculate the scattering current introduced in Sec 6.4 fits well for different biases. Figure 6.15 shows the influence of the SD tunneling as well as the scattering for different channel lengths. A short channel length leads to SD tunneling and consequently a worse subthreshold slope, whereas for long channel devices the on current decreases. If scattering is included, numerical issues of nanoMOS TCAD result in an unphysical high leakage current in the off-state [86]. Since the current for a channel length of $l_{ch} = 6$ nm is almost the same when considering scattering or ballistic current, the TCAD data of the 6 nm device is given as a ballistic one. The other characteristics are given for considering scattering current.

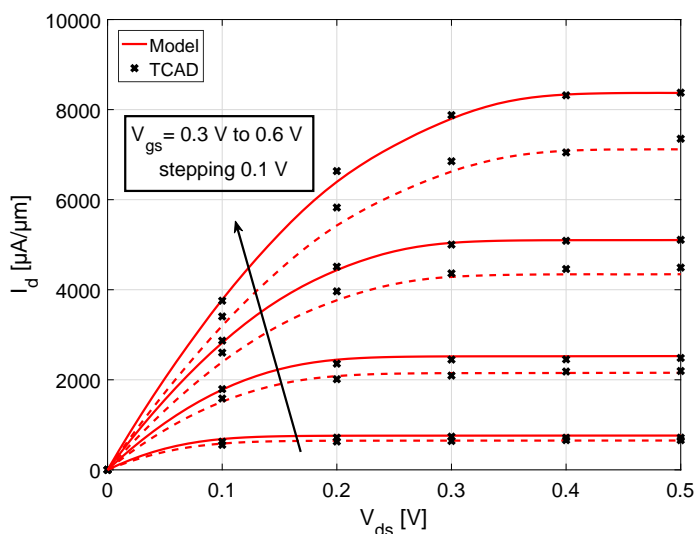


Figure 6.14: Comparison of the ballistic (solid line) to the scattering current (dashed line) shown as output characteristic of the DG MOSFET with a channel length of $l_{ch} = 30$ nm at $T = 300$ K.

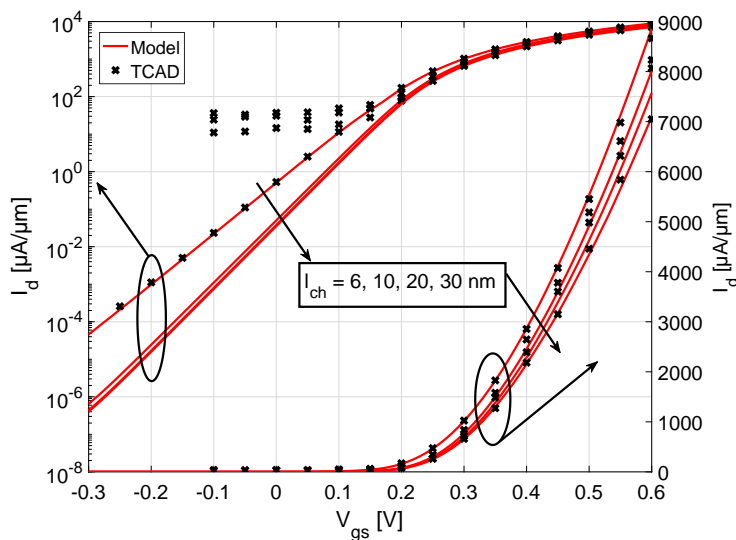


Figure 6.15: Drain current transfer characteristic including scattering and a drain bias of $V_{ds} = 0.05$ V at $T = 300$ K. If scattering is included, numerical issues of nanoMOS TCAD lead to an unphysical high leakage current in the off-state [86]. Therefore, the ballistic TCAD data for a channel length of 6 nm is given as reference.

6.6 Investigations of Short-Channel Effects

The model gives an insight into the physical and even quantum mechanical device behavior. Due to its analytical implementation, physical based investigations can be done faster than by using numerical models.

6.6.1 Source-to-Drain Tunneling

Considering a long channel device, the current is calculated precisely for each energy (see Fig. 6.7). The applied channel length of $l_{ch} = 30$ nm represses a large part of the tunneling current and therefore the current is very low for energies below E_{barrier} . The current increases sharply as soon as the considered energy is nearly equal to E_{barrier} . The current remains almost constant between energies slightly above E_{barrier} and the source Fermi level E_{F1} . For energies above E_{F1} the current decreases according to the Fermi function. Fig. 6.16 shows a separation of the total device current into the SD tunneling and the thermionic emission current. The SD tunneling current $I_{T_{\text{unnel}}}$ describes the device behavior in the subthreshold region, whereas the thermionic emission current $I_{E_{\text{mission}}}$ dominates in the on-state. The total current I_d is given by a summation of both parts.

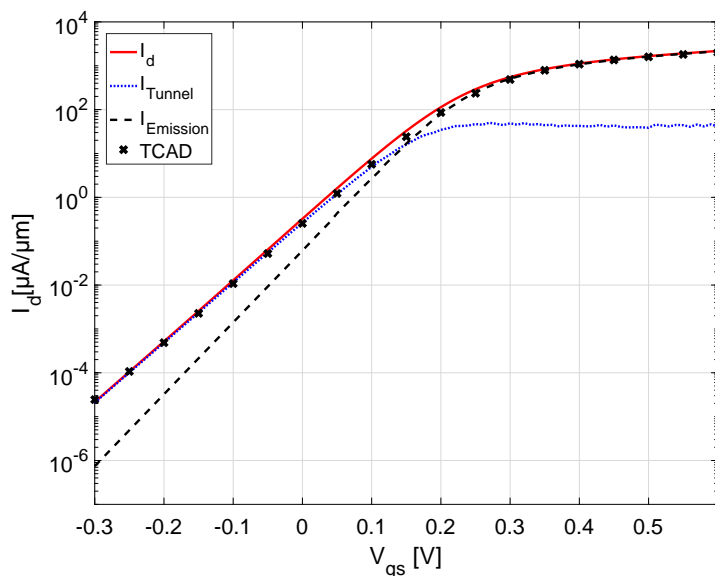


Figure 6.16: Separation of the total model current I_d into the SD tunneling current $I_{T_{\text{unnel}}}$ and thermionic emission current $I_{E_{\text{mission}}}$. The transfer characteristic is given by the model and TCAD data at $V_{ds} = 0.05$ V for a channel length of $l_{ch} = 6$ nm.

6.6.2 Quantum Reflections

Fig. 6.17 shows a partial zoomed view of Fig. 6.7 to highlight the differences of a classical and a quantum based consideration of nano-scaled transistors. Classical physics assumes a transmission coefficient of $T = 1$ for energies greater than the barrier and $T = 0$ for energies lower than the barrier. As introduced in Sec. 2.3.4, due to the quantum mechanical equations, the transmission reaches 1 only at certain resonance energies. The oscillating transmission coefficient of an electron having an energy slightly above the energy barrier is described by wave mechanics [57].

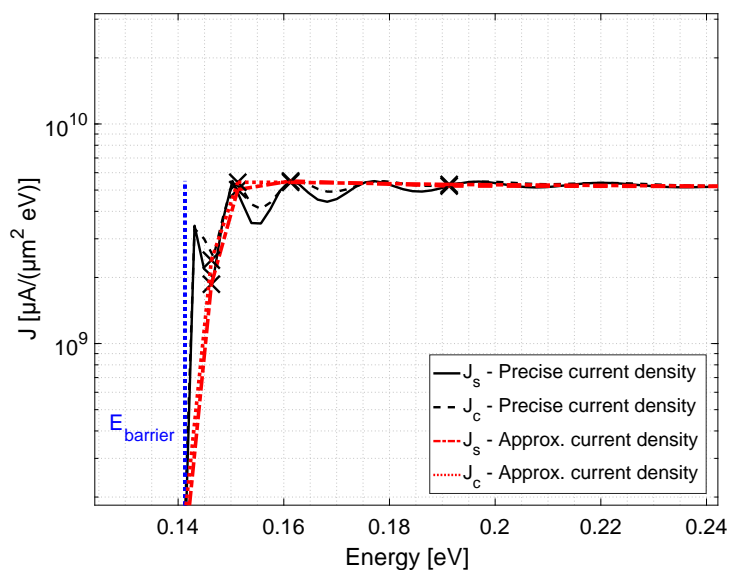


Figure 6.17: The partial enlarged view of Fig. 6.7 shows the oscillating surface and center current density for energies slightly above E_{barrier} at $V_{gs} = 0.4$ V and $V_{ds} = 0.05$ V and a channel geometry of $l_{ch} = 30$ nm, $t_{ch} = 2$ nm.

6.6.3 Leakage Current

The device performance decreases on account of the leakage current appearing in ultra-short channel MOSFETs (see Fig. 6.18). The leakage current increases heavily for channel lengths $l_{ch} < 10$ nm due to the SD tunneling. Lowering the temperature highlights again the SD tunneling because thermionic emission current is repressed and the total current is dominated by the SD tunneling current.

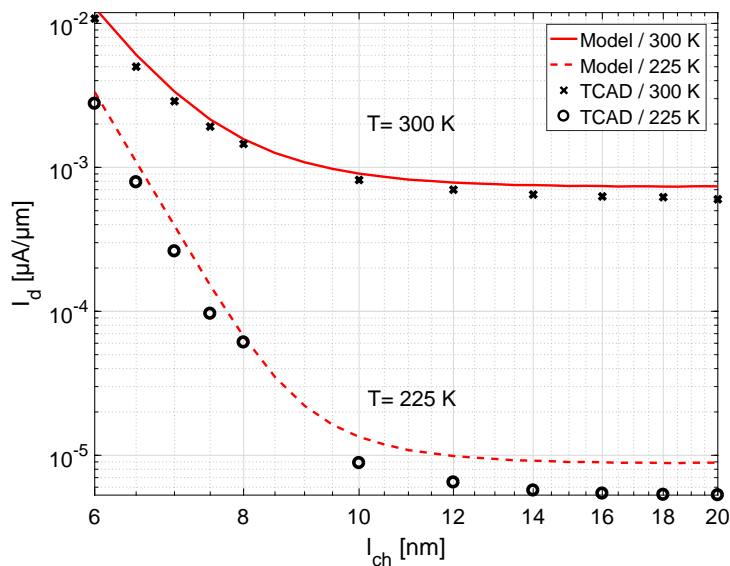


Figure 6.18: Ballistic leakage current depending on the channel length calculated by the model and compared with TCAD data at $V_{gs} = -0.2$ V and $V_{ds} = 0.05$ V for two different temperatures.

6.6.4 Subthreshold Slope

Fig. 6.19 shows the device's subthreshold slope for various channel lengths. The long channel device approaches the ideal subthreshold slope, given by thermal emission, for a temperature of $T = 300\text{ K}$ as well for $T = 225\text{ K}$. Due to the SCEs, this also includes the SD tunneling, the subthreshold slope worsens as soon as the channel length falls below 10 nm , whereby the most degradation is given by the SD tunneling current.

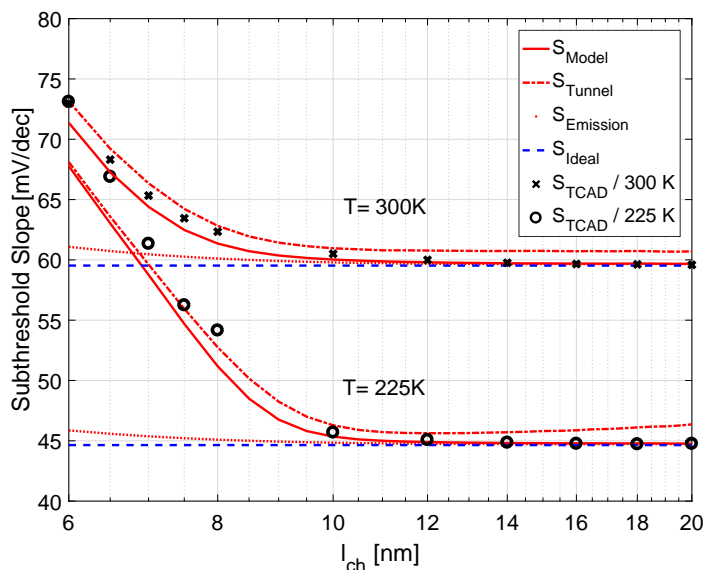


Figure 6.19: Subthreshold slope depending on the channel length calculated by the model and compared with TCAD at $V_{gs} = -0.2\text{ V}$ and $V_{ds} = 0.05\text{ V}$ and different temperatures. Additionally, the subthreshold slope of the model is shown for both the tunneling and thermionic emission current contribution separately. The blue dashed line shows the ideal slope based on the thermionic emission current in a long channel device.

CHAPTER 7

TFET Current Model

Based on the NEGF formalism derived in Sec. 4.2 and the band structure derived in Sec. 5, the TFET current model is introduced. As shown in [67], the device current of TFETs is dominated by the surface part, where the electrostatic control by the gate contact is the best. Therefore, the 1D NEGF is only applied at the channel to insulator interface J_s , as it is depicted in Fig. 7.1. In order to do so, the extraction of the band structure is introduced in Sec. 7.1. Based on the extracted band structure, a time-efficient current calculation is shown in Sec. 7.2. In Sec. 7.3, the quantum based TFET model is compared with numerical TCAD simulation data.

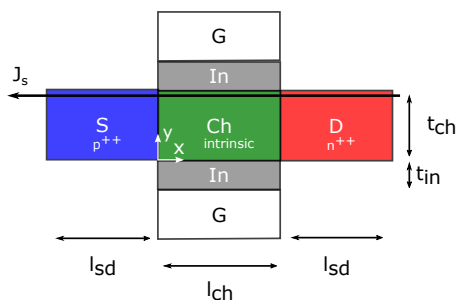


Figure 7.1: Geometry of the applied n-type DG TFET, showing the 1D current density at the channel's surface J_s .

7.1 Transition Between Electrostatics and NEGF

In order to characterize the on-state of the TFET, only the source to channel junction is under investigation. The b2b tunneling current depends on the carrier tunneling between the valence- and conduction band and is therefore calculated by using two separate bands. Since the applied NEGF formalism, as it was introduced in Sec. 4.2, considers only the conduction band, it is necessary to modify the problem in hand. The goal is to map the b2b tunneling into a kind

of tunneling through a barrier (see Fig. 7.2). This is accomplished by a combination of the conduction band E_c and the valence band E_v to build a quasi-conduction band $E_{c,q}$. The quasi-conduction band consists of three parts, a constant energy in the source region, an almost vertical connection and the conduction band of the channel region. The connection merges the constant band of the source region with the conduction band of the channel region. The quasi-conduction band contains the accurate tunneling length between the valence band and the conduction band and additionally considers the shape of the conduction band.

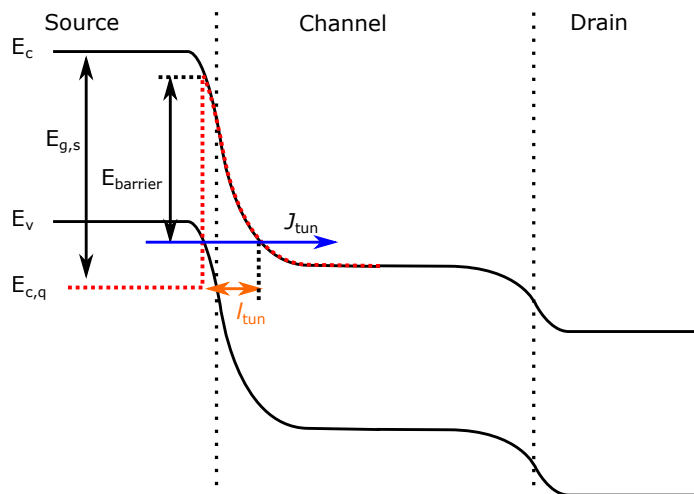


Figure 7.2: The quasi-conduction band transfers the b2b tunneling into a SD tunneling.

In order to set up the quasi-conduction band, the energy window, where b2b tunneling can occur, needs to be defined. The upper limit is defined by the maximum energy of the valence band in the source region $E_{v,max}$ (see Fig. 7.3). This position indicates the highest energy at which b2b tunneling can occur, therefore the first grid point is given at this energy. The last grid point where tunneling current occurs is given by the lowest energy of the conduction band in the channel $E_{c,min}$. At the left side of the connection, the quasi-conduction band is pulled down to a constant energy. This constant energy is fitted to a value below $E_{c,min}$ to offer enough states. At the right side of the connection, the quasi-conduction band equals the conduction band E_c . The tunneling current density per energy J_{tun} is calculated at the energy where the almost vertical connection equals the valence band $E = E_v$. This means, that for each quasi-conduction band the current density is calculated only at one specific energy. With lowering the considered energy, the x -position of the almost vertical connection moves to the right side.

As one can see in Fig. 7.3, the quasi-conduction band does not describe the full band structure in source, channel and drain region. This rough simplification is done for several reasons. First, the focus is on the on-state and the on-state current occurs at the source to

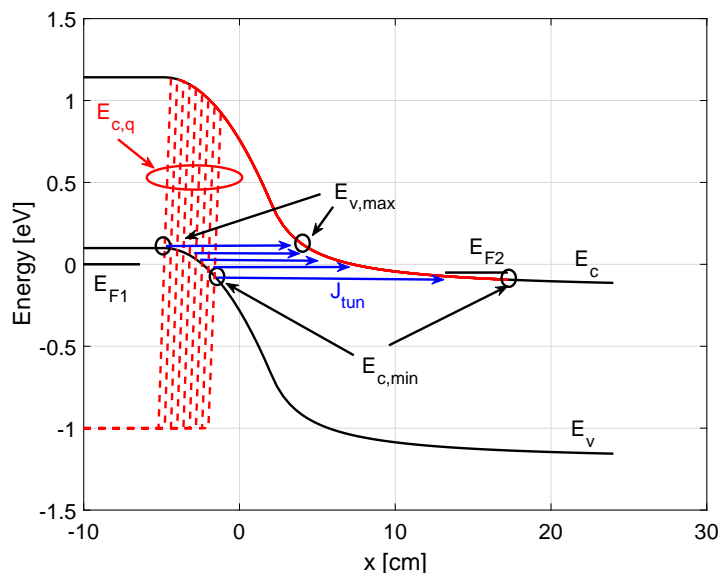


Figure 7.3: Shown is the calculated conduction band E_c and valence band E_v with both Fermi levels E_{F1} and E_{F2} . At each grid point in the energy range of interest, both bands are merged to build the quasi-conduction band $E_{c,q}$. The current density per energy J_{tun} is calculated at the position, where the quasi-conduction band crosses the valence band.

channel junction. Secondly, the applied NEGF algorithm only considers ballistic current. The tunneling current is affected by the tunneling barrier height and length, whereas the ballistic charge transport is not affected by the channel length itself. Reducing the number of grid points leads to a faster calculation of the Green's function and consequently a faster model.

7.2 Current Calculation

Each quasi-conduction band $E_{c,q}$ is used as an individual energy profile $U(x)$ in the 1D NEGF formalism. Therefore, the 1D NEGF equation package already shown in Sec. 6.2 is applied to perform the tunneling current density calculation for each quasi-conduction band. In a further step, these separate currents need to be integrated over energy to receive the drain current density J_d at the channel surface. Fig. 7.4 shows the tunneling distance l_{tun} and current density for the related energy. The resulting tunneling distances for each energy is shown for investigations and is not required to calculate the tunneling current. The tunneling current depends on two parts, the states that get filled by the Fermi function and the tunneling distance. At low energies $E < -0.01$ eV, where the tunneling distance is long, the tunneling current is low. At high energies $E > 0.05$ eV the tunneling distance is short, but the electron density is low, which results in a low tunneling current. The maximum tunneling current is

expected somewhere in the middle of the energy window $-0.01 \text{ eV} < E < 0.05 \text{ eV}$, where l_{tun} is short and the electron density is high.

The current density shown in Fig. 7.4 is calculated at energies marked by \times . The Gaussian shape of the current per energy is approximated by the dashed spline. Integrating this spline leads to the 1D current density at the channel surface. Expanding this current density by the device width and thickness results in the drain current I_d .

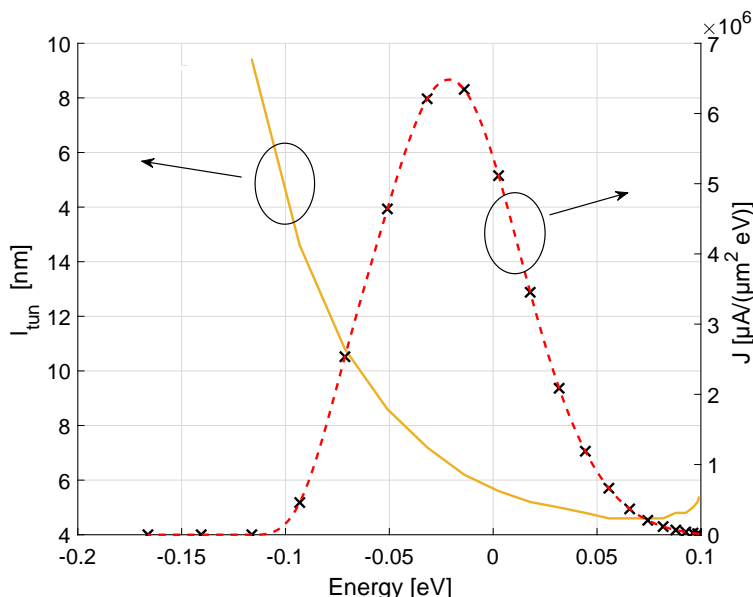


Figure 7.4: The left y -axis shows the resulting tunneling distance l_{tun} for each discrete energy. The right y -axis shows the calculated current density per energy marked by \times at the discrete energies. The dashed line shows a spline interpolation of the current.

7.3 TFET Model Verification

The NEGF based DG TFET model is validated with numeric TCAD Sentaurus simulation data of a short-channel n-type DG TFET by using the non-local tunneling model [26] and the parameters listed in Table 7.1. The model is fitted by adapting the screening length λ and the effective mass used in the NEGF formalism which is set to $m = 0.19 \cdot m_0$. The applied bias conditions are adapted for each simulation and mentioned separately in each figure.

Parameter	Value
l_{ch}	22 nm
t_{ch}	10 nm
t_{in}	2 nm
l_{sd}	20 nm
ϵ_{si}	$11.7 \cdot \epsilon_0$
ϵ_{in}	$25 \cdot \epsilon_0$
N_s	$1 \cdot 10^{20} \text{ cm}^{-3}$
N_d	$1 \cdot 10^{20} \text{ cm}^{-3}$
Device Material	Silicon

Table 7.1: Model simulation parameter set for the DG TFET.

Figure 7.5 shows the resulting current transfer characteristics of the TFET model compared with TCAD simulation data. The drain current shows good transfer characteristic in the subthreshold region as well as in the on-state. The drain bias has only a minor influence on the subthreshold current until the inversion charges come into play. The model overestimates the device current at high drain and gate biases caused by the lack of scattering. In addition, the model overestimates the current because only optimal current components directly under the gate are taken into account. In the real device, the current within the channel center is smaller and consequently the total current. If only the perfect slice is taken to fit the whole device, a performance overestimation is to be expected. The device's off current is caused by TAT, whereby the model treats this effect by a constant fitting parameter.

Figure 7.6 shows the transistor's output current characteristic. The analytical model shows a good agreement for the subthreshold slope when comparing to numerical data. The on-state is quite accurate too but for a high drain bias the deviation increases. This deviation is again justified by the ballistic transport of the model and the non-ballistic current transport given by the Sentaurus TCAD data as well as for the geometry dependent integration of the current.

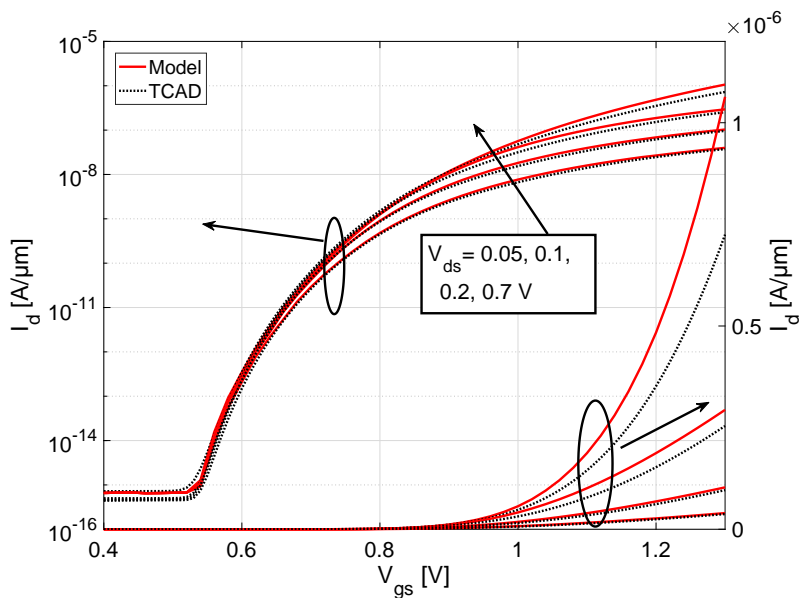


Figure 7.5: Depicted is the resulting transfer characteristics in log-scale on the left y -axis and in linear scale on the right one, respectively. The model shows a good behavior for a wide range of gate and drain bias conditions.

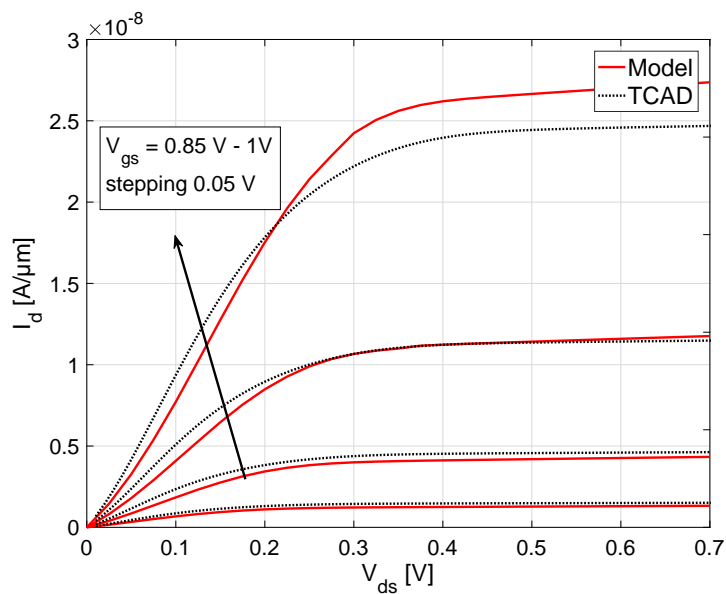


Figure 7.6: Shown is the resulting drain current I_d in the output characteristic.

CHAPTER 8

Conclusion

In this doctoral study, two analytical double-gate transistor models for considering quantum based charge transport were presented. The MOSFET model aimed for ultra-short channel lengths by applying the non-equilibrium Green's function (NEGF) formalism. The NEGF formalism allowed to calculate the classical thermionic emission current as well as the emerging quantum mechanical source-to-drain tunneling current. Based on the MOSFET model, the TFET model was derived in a second step. The TFET model made use of the NEGF formalism to calculate the band-to-band tunneling current. Both analytical transistor models showed an accurate agreement with numerical TCAD simulation data.

At the beginning, the iterative process of the quantum based transport solver with the Poisson solver was decoupled. The omitted iterative coupling was achieved by an accurate potential model and led to a reduced computational complexity. The potential model was constructed by a closed-form potential solution, which was derived from a classical analytical model. Initially, the subthreshold region of the device was under consideration, where mobile charges played only a minor role. This assumption enabled the use of the Laplace equation instead of Poisson's equation, which can be computed in a closed-form. A further step estimated the effect of the inversion charges on the device's electrostatics analytically. The potential within the 2D channel area was determined by using the complex potential theory. The gate influence on the source and drain region affects the tunneling distance and was consequently approximated by a parabolic shaped potential profile. It was found, that the quantum confinement, which occurs in ultra-thin channels, can be treated efficiently by empirical equations. The analytical potential model was compared with numerical TCAD data and showed accurate results for short-channel and also for ultra-short channel devices.

The conduction- and valence bands were derived from the device's potential for certain geometry variations. The band structure was used as the connecting link between potential solution and transport solver. The 1D NEGF was formulated by applying the effective mass Hamiltonian, the Fermi level of each contact and open boundary conditions. The Green's function was used to calculate the current density at certain energies in order to reduce the

computational effort. Instead of considering discrete infinitesimal energies, the number of considered energies was reduced to a minimum by an interpolation based on some specific energies and geometric positions. The analytical current calculation of the 3D device using 1D current densities at a few distinctive energies led to a notable drop in calculation time.

The base of the MOSFET model is formed by a ballistic NEGF approach to consider quantum effects in transport direction. The source-to-drain tunneling current, which is not described by classical transport equations, was effectively calculated and highlighted at low temperatures. The model correctly predicted this effect because the NEGF formalism inherently includes thermionic emission and source-to-drain tunneling current. The ballistic current model was enhanced to consider devices with a longer channel length by calculating back scattering in a closed-form approach. The transfer and output current characteristics of the MOSFET model were validated by far more time-consuming NEGF based TCAD simulations. It was shown that the model accurately captured the quantization effects which heavily influence the device's threshold voltage for ultra-thin channels from 2 nm to 5 nm. A variation of the channel length from 6 nm to 30 nm confirmed the scalability of the modeling approach. The analytical MOSFET model allowed to perform physics-based investigations such as the appearance of source-to-drain tunneling, subthreshold slope degradation and leakage current influences of ultra-scaled devices. The presented approach demonstrated a numerically efficient way to consider quantum mechanical transport in ultra-scaled MOSFET devices in a multi-scale simulation environment.

The analytical DG TFET model was accomplished by the combination of a classical calculation of the device's potential with a quantum mechanical treatment of the charge transport. The model introduced the physics-based calculation of the band-to-band tunneling current by using the device's band structure. In order to avoid the computational burden of a two band structure, the band-to-band tunneling was mapped into direct tunneling within a single band. Therefore, the conduction- and valence bands were cut into many quasi-conduction bands. The tunneling current was calculated at the channel's surface for certain energies which led to an improvement in the computational complexity. The model was able to correctly predict the band-to-band tunneling current because the quantum mechanical charge transport is solved by using the NEGF formalism. The transfer and output current characteristic were compared to numerical TCAD Sentaurus simulation data and showed accurate results. The multi-scale simulation was fulfilled by a quantum based analytical TFET model.

One important requirement for compact models is a continuous current characteristic as well as the derivatives of it. The overbarrier reflections in combination with a piecewise current density calculation may cause a discontinuity and consequently has to be eliminated. The progressive downscaling leads to ultra-thin channels. Especially when considering a channel thickness below 5 nm, the device behavior changes rapidly. The applied concept to handle quantization effects is not position dependent and consequently leads to a simplification of the interface charges at the channel to insulator junctions. A possibility to overcome this incongruity is to pursue a 2D approach. For this purpose, the carrier quantization could

be calculated more accurately by applying a further 1D NEGF formalism in the device's cross-section. Considering band-to-band tunneling by a source-to-drain tunneling approach is certainly not the best practice, yet it is a fundamental first step in the right direction. This approach could be improved by applying a more complex multi-band effective mass Hamiltonian to consider the valence band as well as the conduction band. A further unwanted effect which comes into focus is the gate leakage current. Since the insulator represents a potential barrier and electrons tunnel through it, this effect is described by quantum mechanics and can be captured by the NEGF formalism. The goal of nano transistor technology is the utilization of 3D device structures such as silicon nanowire transistors, hence an adaption for cylindrical device structures is recommended.

Both introduced quantum based models are analytically solved and much more time-efficient than iterative ones. Nevertheless, both models cannot be used for circuit simulations. To achieve this, all mathematical equations must be transferred into compact equations and finally implemented in the hardware description language Verilog-A. Based on the NEGF formalism, atomistic level calculations by using tight binding Hamiltonians can be done and therefore, both introduced transistor models open the door to consider even more quantum mechanical effects in a fast and efficient way.

The future will show in which direction the exiting research and development of emerging transistors and thus the modeling approaches will go.

References

- [1] Univeristy California, *SPICE3 Version 3e User's Manual*, 1991.
- [2] J. E. Lilienfeld, "Method and apparatus for controlling electric currents," Jan. 28 1930. US Patent 1,745,175.
- [3] E. Schrödinger, "Quantisierung als eigenwertproblem," *Annalen der Physik*, vol. 384, 1926.
- [4] R. Ohl, "Light-sensitive electric device," June 25 1946. US Patent 2,402,662.
- [5] W. Schockley, "Circuit element utilizing semiconductive methodaterial," Sept. 25 1948. US Patent 2,569,347.
- [6] W. Schockley, "The theory of p-n junctions in semiconductors and p-n junction transistors," *The Bell System Technical Journal*, vol. 28, pp. 435–489, July 1949.
- [7] W. Shockley, M. Sparks, and G. K. Teal, "p-n Junction Transistors," *Physical Review*, vol. 83, pp. 151–162, 1951.
- [8] J. Kilby, "Invention of the integrated circuit," *IEEE Transactions on Electron Devices*, vol. 23, pp. 648–654, Jul 1976.
- [9] D. Kahng, "Electric field controlled semiconductor device," Aug. 27 1963. US Patent 3,102,230.
- [10] F. Wanlass and C. Sah, "Nanowatt logic using field-effect metal-oxide semiconductor triodes," in *Solid-State Circuits Conference. Digest of Technical Papers. 1963 IEEE International*, vol. VI, pp. 32–33, Feb 1963.
- [11] F. Wanlass, "Low stand-by power complementary field effect circuitry," Dec. 5 1967. US Patent 3,356,858.
- [12] G. E. Moore, "Cramming more components onto Integrated circuits," April 1965.
- [13] G. E. Moore, "Progress in digital integrated electronics," *Electron Devices Meeting*, vol. 21, pp. 11–13, 1975.

-
- [14] F. Faggin, M. E. Hoff, S. Mazor, and M. Shima, "The history of the 4004," *IEEE Micro*, vol. 16, pp. 10–20, Dec 1996.
- [15] "International technology roadmap for semiconductors 2.0 (ITRS)," 2015.
- [16] M. Bohr, "14 nm process technology: Opening new horizons," in *Intel Developer Forum (IDF14)*, 2014.
- [17] E. Fayneh, M. Yuffe, E. Knoll, M. Zelikson, M. Abozaed, Y. Talker, Z. Shmueli, and S. A. Rahme, "14nm 6th-generation core processor soc with low power consumption and improved performance," in *IEEE International Solid-State Circuits Conference (ISSCC)*, pp. 72–73, Jan 2016.
- [18] N. Arora, *MOSFET Modeling for VLSI simulation*. World Scientific Publishing Company, 1993.
- [19] S. M. Sze, *Physics of Semiconductur Devices*. Wiley, 2006.
- [20] C. Shin, X. Sun, and T. J. K. Liu, "Study of random-dopant-fluctuation (RDF) effects for the trigate bulk MOSFET," *IEEE Transactions on Electron Devices*, vol. 56, pp. 1538–1542, July 2009.
- [21] K. Patel, T. J. K. Liu, and C. J. Spanos, "Gate line edge roughness model for estimation of FinFET performance variability," *IEEE Transactions on Electron Devices*, vol. 56, pp. 3055–3063, Dec 2009.
- [22] Y. Omura, S. Horiguchi, M. Tabe, and K. Kishi, "Quantum-mechanical effects on the threshold voltage of ultrathin-SOI nMOSFETs," *IEEE Electron Device Letters*, vol. 14, pp. 569–571, Dec 1993.
- [23] J. Wang and M. Lundstrom, "Does source-to-drain tunneling limit the ultimate scaling of MOSFETs?," *International Electron Devices Meeting IEDM*, pp. 707–710, 2002.
- [24] M. Bescond, J. L. Autran, D. Munteanu, N. Cavassilas, and M. Lannoo, "Atomic-scale modeling of source-to-drain tunneling in ultimate schottky barrier double-gate MOSFETs," in *33rd Conference on European Solid-State Device Research (ESSDERC)*, pp. 395–398, Sept 2003.
- [25] D. Esseni, M. Pala, P. Palestri, C. Alper, and T. Rollo, "A review of selected topics in physics based modeling for tunnel field-effect transistors," *Semiconductor Science and Technology*, vol. 32, no. 8, 2017.
- [26] Synopsys, Inc., *TCAD Sentaurus, C-2012.06 ed.*, 2012.
- [27] K.-T. Grasser, "Minimos-NT Device and Circuit Simulator," September 2002.

- [28] SILVACO, Inc., “ALTAS User’s Manual Device Simulation Software,” September 2010.
- [29] G. Klimeck and M. Luisier, “Atomistic modeling of realistically extended semiconductor devices with nemo and omen,” *Computing in Science Engineering*, vol. 12, pp. 28–35, March 2010.
- [30] Anacad GmbH, *ELDO User’s Manual*, 2005.
- [31] T. Grasser, *Advanced device modeling and simulation*, vol. 31. World scientific, 2003.
- [32] D. Vasileska and S. Goodnick, *Computational Electronics*. Morgan & Claypool, 2003.
- [33] Y. Tsividis, *Operational Modeling of the MOS Transistor*. McGraw-Hill, 1999.
- [34] Q. Rafhay, R. Clerc, G. Ghibaudo, and G. Pananakakis, “Impact of source-to-drain tunnelling on the scalability of arbitrary oriented alternative channel material nMOSFETs,” *Solid-State Electronics*, vol. 52, no. 10, pp. 1474–1481, 2008.
- [35] J. R. Watling, A. R. Brown, A. Asenov, A. Svizhenko, and M. P. Anantram, “Simulation of direct source-to-drain tunnelling using the density gradient formalism: Non-Equilibrium Greens Function calibration,” *International Conference on Simulation of Semiconductor Processes and Devices SISPAD*, vol. 7, pp. 267–270, 2002.
- [36] F. Ortmann, S. Roche, J. C. Greer, G. Huhs, X. Oriols, T. Shulthess, T. Deutsch, P. Weinberger, M. Payne, J. M. Sellier, J. Sprekels, J. Weinbub, K. Rupp, M. Nedjalkov, D. Vasileska, E. Alfinito, L. Reggiani, D. Guerra, D. K. Ferry, M. Saraniti, S. M. Goodnick, A. Kloes, L. Colombo, K. Lilja, J. Mateos, T. Gonzalez, E. Velazquez, P. Palestri, and A. S. M. Macucci, “European multiscale simulation for the computational era,” *Nanonewsletter*, 2012.
- [37] S. Datta, *Quantum Transport: Atom to Transistor*. Cambridge University Press, 2005.
- [38] Z. Ren, S. Goasguen, A. Matsudaira, S. S. Ahmed, K. Cantley, Y. Liu, Y. Gao, X. Wang, and M. Lundstrom, “NanoMOS,” 2016. <https://nanohub.org/resources/nanomos>.
- [39] G. Fiori and G. Iannaccone, “NanoTCAD ViDES,” 2014.
- [40] Global TCAD Solutions GmbH, *VSP-a quantum-electronic simulation framework*. Springer Science+Business Media, 2013.
- [41] M. P. Anantram, S. S. Ahmed, A. Svizhenko, D. Kearney, and G. Klimeck, “NanoFET,” 2016.
- [42] S. Datta, “Nanoscale device modeling: the Green’s Function method,” *Superlattices and Microstructures*, vol. 28, no. 4, pp. 253–278, 2000.

- [43] A. Bhattacharyya, *Compact MOSFET Models for VLSI Design*. Wiley, 2009.
- [44] C. Galup-Montoro and M. C. Schneider, *MOSFET Modeling for Circuit Analysis and Design*. World Scientific Publishing Co. PTe. LTd., 2007.
- [45] Y. Cheng, M.-C. Jeng, Z. Liu, J. Huang, M. Chan, K. Chen, P. Ko, and C. Hu, “A physical and scalable I-V model in BSIM3v3 for analog/digital circuit simulation,” *Electron Devices, IEEE Transactions on*, vol. 44, no. 2, pp. 277–287, 1997.
- [46] R. Velghe, D. Klaassen, and F. Klaassen, “MOS Model 9,” tech. rep., Philips Electronics N.V, 1994.
- [47] R. v. Langevelde, A. Scholten, and D. Klaassen, “MOS Model 11,” tech. rep., Philips Electronics N.V, 2005.
- [48] M. Miura-Mattausch, H. Ueno, J. Mattausch, S. Kumashiro, T. Yamaguchi, K. Yamashita, and N. Nakayama, “HiSIM: Self-consistent surface-potential MOS-model valid down to sub-100 nm technologies,” *Technical Proceedings of the International Conference on Modeling and Simulation of Microsystems*, 2002.
- [49] G. Gildenblat, X. Li, W. Wu, H. Wang, A. Jha, R. van Langevelde, G. Smit, A. Scholten, and D. Klaassen, “PSP: An advanced surface-potential-based MOSFET model for circuit simulation,” *IEEE Transactions on Electron Devices*, vol. 53, 2006.
- [50] J. He, J. Xi, M. Chan, H. Wan, M. Dunga, B. Heydari, A. Niknejad, and C. Hu, “Charge-based core and the model architecture of BSIM5,” in *Sixth International Symposium on Quality of Electronic Design, 2005 (ISQED)*, pp. 96–101, 2005.
- [51] E. V. C. Enz and F. Krummenacher, “An analytical MOS transistor model valid in all regions of Operation and dedicated to low-voltage and low-current applications,” *Journal on Analog Integrated Circuits and Signal Processing, Kluwer Academic Publishers*, 1995.
- [52] C. Galup-Montoro, M. C. Schneider, A. I. A. Cunha, F. R. De Sousa, H. Klimach, and O. Siebel, “The advanced compact MOSFET (ACM) model for circuit analysis and design,” in *Custom Integrated Circuits Conference (CICC '07)*, pp. 519–526, 2007.
- [53] M. Graef, T. Holtij, F. Hain, A. Kloes, and B. Iniguez, “Improved analytical potential modeling in Double-Gate Tunnel-FETs,” *Mixed Design of Integrated Circuits Systems (MIXDES)*, vol. 21, pp. 49–53, 2014.
- [54] A. Kloes, M. Schwarz, T. Holtij, and A. Navas, “Quantum confinement and volume inversion in MOS3 model for short-channel Tri-Gate MOSFETs,” *IEEE Transactions on Electron Devices*, vol. 60, pp. 2691–2694, aug 2013.

- [55] E. Weber, *Electromagnetic Fields: Theory and Applications: Volume I-Mapping of Fields*. John Wiley & Sons, 1960.
- [56] F. Thuselt, *Physik der Halbleiterbauelemente*. Springer-Verlag Berlin Heidelberg, 2011.
- [57] V. V. Mitin, V. A. Kochelap, and M. A. Stroschio, *Introduction to Nanoelectronics, Science, Nanotechnology, Engineering, and Applications*. Cambridge University Press, 2008.
- [58] S. Datta, “Electrical resistance: an atomistic view,” *Nanotechnology*, vol. 15, no. 7, pp. 433–451, 2004.
- [59] J.-P. Colinge, *FinFETs and Other Multi-Gate Transistors*. Springer Science+ Business Media, 2007.
- [60] B. Iniguez, T. A. Fjeldly, A. Lazaro, F. Danneville, and M. J. Deen, “Compact-modeling solutions for nanoscale double-gate and gate-all-around MOSFETs,” *IEEE Transactions on Electron Devices*, vol. 53, pp. 2128–2142, Sept 2006.
- [61] M. Schwarz, *Two-dimensional analytical predictive modeling of schottky barrier SOI and multi-gate MOSFETs*. PhD thesis, 2012.
- [62] M. S. Lundstrom, *Nanoscale Transistors*. Springer Science+Business Media, Inc., 2006.
- [63] M. S. Lundstrom, “A top-down introduction to the NEGF approach,” 2004.
- [64] G. Hilot, Q. Raffay, F. Boeuf, and G. Ghibaudo, “Analytical relationship between subthreshold swing of thermionic and tunnelling currents,” *Electronic Letters*, vol. 50, no. 23, pp. 1745–1747, 2014.
- [65] A. C. Seabaugh and Q. Zhang, “Low-voltage tunnel transistors for beyond CMOS logic,” *Proceedings of the IEEE*, vol. 98, no. 12, pp. 2095–2110, 2010.
- [66] A. Vandooren, D. Leonelli, R. Rooyackers, A. Hikavy, K. Devriendt, M. Demand, R. Loo, G. Groeseneken, and C. Huyghebaert, “Analysis of trap-assisted tunneling in vertical si homo-junction and sige hetero-junction tunnel-FETs,” *Solid-State Electronics*, vol. 83, pp. 50–55, 2013.
- [67] F. Horst, M. Graef, F. Hosenfeld, A. Farokhnejad, F. Hain, G. V. Luong, Q. T. Zhao, B. Iniguez, and A. Kloes, “Implementation of a DC compact model for double-gate Tunnel-FET based on 2D calculations and application in circuit simulation,” in *46th European Solid-State Device Research Conference (ESSDERC)*, pp. 456–459, 2016.
- [68] L. Zhang, J. He, and M. Chan, “A compact model for double-gate tunneling field-effect-transistors and its implications on circuit behaviors,” in *International Electron Devices Meeting*, 2012.

- [69] L. Zhang and M. Chan, *Tunneling Field Effect Transistor Technology*. Springer International Publishing, 2016.
- [70] K. Küpfmüller, W. Mathis, and A. Reibiger, *Theoretische Elektrotechnik*. Springer Berlin Heidelberg New York, 2006.
- [71] H. Henke, *Elektromagnetische Felder*. Springer Science+Business Media, 2007.
- [72] P. J. Oliver, *Introduction to Partial Differential Equations*. Springer Science+Business Media, 2014.
- [73] Technische Universität Berlin, Fachbereich Mathematik, “Finite differenzen methode,” 2011.
- [74] M. Büttiker, “Role of quantum coherence in series resistors,” vol. 33, no. 5, 1986.
- [75] A. Kloes and A. Kostka, “A new analytical method of solving 2D Poisson’s equation in MOS devices applied to threshold voltage and subthreshold modeling,” *Solid-State Electronics*, vol. 39, no. 12, pp. 1761–1775, 1996.
- [76] M. S. Lundstrom, “Elementary scattering theory of the Si MOSFET,” *IEEE Electron Device Letters*, vol. 18, no. 7, pp. 361–363, 1997.
- [77] J. Wang, A. Rahman, A. Ghosh, G. Klimeck, and M. Lundstrom, “On the validity of the parabolic effective-mass approximation for the I-V calculation of silicon nanowire transistors,” *IEEE Transactions on Electron Devices*, vol. 52, no. 7, pp. 1589–1595, 2005.
- [78] D. Selim, S. Gamal, W. Fikry, and O. A.-E. Halim, “Rapid and efficient method for numerical quantum mechanical simulation of gate-all-around nanowire transistors,” *International Conference on Microelectronics*, vol. 28, pp. 229–232, 2012.
- [79] T. Dutta, Q. Rafhay, G. Pananakakis, and G. Ghibaudo, “Modeling of the impact of source/drain regions on short channel effects in MOSFETs,” in *Ultimate Integration on Silicon (ULIS)*, vol. 14, pp. 69–72, 2013.
- [80] A. Tsormpatzoglou, C. A. Dimitriadis, R. Clerc, Q. Rafhay, G. Pananakakis, and G. Ghibaudo, “Semi-analytical modeling of short-channel effects in Si and Ge symmetrical double-gate MOSFETs,” *Electron Devices, IEEE Transactions*, vol. 54, no. 8, pp. 1943–1952, 2007.
- [81] M. Schwarz, T. Holtij, A. Kloes, and B. Iniguez, “Analytical compact modeling framework for the 2D electrostatics in lightly doped double-gate MOSFETs,” *Solid-State Electronics*, pp. 72–84, 2012.

-
- [82] A. Gnudi, S. Reggiani, E. Gnani, and G. Baccarani, “Semianalytical model of the subthreshold current in short-channel junctionless symmetric double-gate field-effect transistors,” *IEEE Transactions On Electron Devices*, vol. 60, no. 4, pp. 1342–1348.
- [83] J. D. Alamo, S. Swirhun, and R. Swanson, “Simultaneous measurement of hole lifetime, hole mobility and bandgap narrowing in heavily doped n-type silicon,” *Electron Devices Meeting*, pp. 290–293, 1985.
- [84] Z. Ren, R. Venugopal, S. Goasguen, S. Datta, and M. S. Lundstrom, “nanoMOS 2.5: A two-dimensional simulator for quantum transport in double-gate MOSFETs,” *IEEE Transactions on Electron Devices*, vol. 50, pp. 1914–1925, Sept 2003.
- [85] K. Raseong and L. Mark, “Notes on Fermi-Dirac integrals (3rd Edition),” sep 2008.
- [86] Z. Ren, *Nanoscale MOSFETs: physics, simulation and design*. PhD thesis, Purdue University, 2001.



UNIVERSITAT
ROVIRA i VIRGILI